Summer 2024

High-Resolution Spectroscopy of Interstellar Lines and Comets

Chemeda Tadese Ejeta
Missouri University of Science and Technology

Department: Physics

HIGH-RESOLUTION SPECTROSCOPY OF INTERSTELLAR LINES AND COMETS

by

CHEMEDA TADESE EJETA

A DISSERTATION

Presented to the Graduate Faculty of the

MISSOURI UNIVERSITY OF SCIENCE AND TECHNOLOGY

and

UNIVERSITY OF MISSOURI-ST.LOUIS

In Partial Fulfillment of the Requirements for the Degree

DOCTOR OF PHILOSOPHY

in

PHYSICS

2024

Approved by:

Dr. Erika Gibb, Advisor
Dr. Shun Saito (co-advisor)
Dr. Alexey Yamilov
Dr. David Horne
Dr. Bruce Wilking

PUBLICATION DISSERTATION OPTION

This dissertation consists of the following two papers, formatted in the style used by the Missouri University of Science and Technology.

Paper I: Pages 38-70 have been published in the Astronomical Journal.

Paper II: Pages 71-96 are intended for submission to Astronomical Journal.

ABSTRACT

The study of interstellar molecules such as CO is crucial because interstellar ices in the core of a pre-solar molecular cloud provide the starting point for volatile evolution in the protoplanetary disk. A record of the initial volatile composition of the protoplanetary disk can be obtained from the study of the chemical composition of cometary nuclei. Because of their long residence in the Oort cloud and infrequent passage through the inner solar system, long-period comets are one of the most primitive bodies in our solar system that can tell us about the composition of the early solar system. High-resolution infrared spectroscopy allows for measuring the chemical abundances of primary volatile species (sublimed native ices directly from the nucleus) in the comae of comets, which are crucial for their chemical taxonomic classification. Characterizing the chemical composition of comets over a range of heliocentric distances (R_h) is crucial to investigate whether the composition of the cometary nucleus varies with heliocentric distance or remains constant. There is a systematic enhancement of some molecules (C_2H_2, NH_3, H_2CO) for comets observed close to the Sun compared to those observed beyond ~1 au. Measurements of the chemical abundance of primary volatile species in the long-period comet C/2020 S3 (Erasmus) observed near R_h ~0.5 AU, presented in this study, contribute to the effort of investigating the chemical abundances at small heliocentric distances. Within 2 AU from the Sun, cometary activity is mainly driven by the sublimation of H_2O ice. On the other hand, cometary outgassing beyond the sublimation region of H_2O (~ 3.0 AU) is driven by hypervolatile species such as CO and CO_2. There have only been a few comet measurements made over the transitional heliocentric distance range R_h ~2.5-3.0 AU because the majority of comets are either very faint or show low activity at this distance from the Sun. This leaves it uncertain where the transition from hypervolatile to H_2O-driven activity occurs. Observations of long-period comet C/2017 K2 (Pan-STARRS) spanning a range of R_h ~2.35 - 3.15 AU were conducted to address this critical topic in cometary science.

ACKNOWLEDGMENTS

I want to thank Dr. Erika Gibb for her guidance and advice throughout this dissertation, starting from the first part of this project; without her help, I would not have completed this project. I thank Dr. Gibb and her collaborators for teaching me how to write observing time proposals, for their help in reducing and analyzing comet spectra, and for providing invaluable comments and discussions on papers they co-authored with me. Without any exaggeration, this opportunity does not come along very often. I must admit that I have been fortunate enough to have collaborated with these world-class researchers - courtesy of Dr. Gibb. In particular, I would like to thank Dr. Nathan Roth for allowing me to work on his C/2020 S3 data, which he acquired as a PI, at the time, I did not have comet data to work on as part of my Ph.D. project shortly after I transitioned to comet project.

I want to thank Dr. Bruce Wilking for his help and advice on the first part of this project. I also thank Dr. Wilking for encouraging me to apply to the UMSL Physics Ph.D. program when he was a Graduate School program coordinator and eventually for giving me the chance to be a Graduate Teaching Assistant, which was of great help to me at the time. I want to thank my committee members, Dr. Alexey Yamlov, Dr. Shun Saito, and Dr. David Horne, for their time and willingness to serve as my committee members. In addition, my sincere thanks go to Dr. Sonya Bahar, who has been supportive and offered me words of encouragement throughout my time at UMSL, especially at tough times in my life. Thank you, Dr. Bahar!

I also thank Dr. Mohammad Saki and Dr. Younas Khan for their help with my questions on comet data reduction and analyses.

TABLE OF CONTENTS

Page

LIST OF ILLUSTRATIONS

Figure Page

SECTION

PAPER I

PAPER II

LIST OF TABLES

SECTION

1. INTRODUCTION

1.1. STAR FORMATION

Observations have shown that star formation in galaxies is strongly associated with molecular gas (e.g. Bigiel et al., 2008; Leroy et al., 2008). The interstellar space (medium) contains inhomogeneously distributed matter from the galaxy, mostly in the form of *gas* and in smaller amounts as dust, which are tiny solid particles (e.g. Ferrière, 2001). Interstellar medium in galaxies such as the Milky Way is predominantly H I by mass, and in such galaxies, molecular gas is organized into discreet clouds that are highly filamentary and clumpy, called giant molecular clouds (Krumholz, 2015). Giant molecular clouds (GMCs) range in mass from $\sim 10^7$ $M_\odot$ to $\sim 10^4$ $M_\odot$ and are hundreds of light-years across (e.g. Greene, 2001; Oka et al., 2001). Regions within the GMCs with density $\geq 10^5$-10^7 H_2 molecules per cm^3 that are roughly round in morphology than the lower-density material around them are called *cores*, and they are thought to be the progenitors of single stars or star systems (Dobbs et al., 2014; Krumholz, 2015; Wilking et al., 2008). Individual stars emerge from dense core fragments of mass ~ 1 $M_\odot$ within much larger $\sim 10^6$ $M_\odot$ GMC, as a result, young stars usually form in *clusters* (Krumholz, 2015).

1.2. STAGES OF STAR FORMATION

The self-gravitating gas of the densest cores of interstellar GMCs or the *prestellar cores* begin to collapse when their gravity exceeds the internal pressure support of the cloud (Stahler, 1983).

The minimum amount of mass required for the core of a GMC to undergo gravitational collapse is expressed by the Jeans Mass, M_J, (Jeans, 1928),

$$M_J \simeq \left(\frac{\pi k_B T}{G\mu m_H}\right)^{\frac{3}{2}} \left(\frac{1}{\rho_0}\right)^{\frac{1}{2}}, \tag{1.1}$$

where T is the temperature of the cloud, μ is the mean molecular weight of the cloud, $\rho_0 = \mu m_H n_{H_2}$ is the initial mass density of the molecular cloud (assumed to be constant throughout the cloud), m_H is the mass of hydrogen atom, G is the gravitational constant, k_B is the Boltzmann constant, and n_{H_2} is the number density of the hydrogen molecule. For example, for T = 10 K and $n_{H_2} = 10^6$ cm^{-3}, the Jean Mass is $M_J = 0.83\ M_\odot$.

As the core central density increases ($\rho_c \gtrsim 10^{-13}$ g cm^{-3}), the inner region of the core becomes opaque to radiation, increasing its temperature. An increase in temperature, in turn, causes an increase in thermal pressure since radiation cannot escape (Dunham et al., 2014; Larson, 1969). The increase in thermal pressure slows further collapse and forms the *first hydrostatic core*, which is a few AU in size and a few hundredths of a solar mass (Krumholz, 2015). The central density and temperature of this core rise as it keeps accreting material from its surroundings. The molecular hydrogen dissociates due to collision, and the kinetic energy required for the dissociation is transformed into chemical energy, which lowers the kinetic energy budget of the gas. A small increase in temperature drastically boosts the dissociation rate, transforming more kinetic energy into chemical energy, thereby preventing further central temperature rise for the thermal pressure to balance the gravitational force. As a result, the first core undergoes a gravitational collapse, which lasts until all of the hydrogen dissociates. Eventually, this leads to the development of a second hydrostatic core called *protostar* or *Stage 0* (Dunham et al., 2014; Krumholz, 2015). The time scale for the collapse of the first core to form the protostar phase is the free-fall time (Dobbs et al., 2014; Lada, 2005): $\tau_{ff} = \left(\frac{3\pi}{32 G \rho_c}\right)^{\frac{1}{2}}$, where ρ_c is the central density of the first core. For a typical GMC, $\rho_c = 100\ m_p$, and the free-fall time for the protostar to form is $\sim 10^5$ years (Greene, 2001).

Since protostellar objects are generally deeply embedded in a large envelope of nascent dust and gas, their mass is smaller than the envelope of material surrounding them (e.g., Cox et al., 2017). As the protostar accumulates mass from its surrounding envelope of gas and dust, the *circumstellar disk* is formed by the rotating material around the protostar that falls into orbits of different radii (Greene, 2001). Some matter remains in orbit, but eventually, much matter flows through the disc into the protostar. The stellar mass eventually exceeds the remaining core mass as most of the envelope material is directed into the central protostar through a circumstellar disk, and the system becomes a *Stage I* object (Dunham et al., 2014). Sources transitioning out of Stage I are referred to as *Flat-Spectrum (FS)* objects.

After the envelope around the Stage I object has faded, most of the circumstellar material is in a large disk that surrounds the central object and continues to slowly accrete to the star (e.g., Cox et al., 2017). This disk is both optically thick and spatially thin. *Stage II* is the term used to describe an object in this Stage. After the protostar has accreted its final mass, a thin circumstellar disk remains, and the object is categorized as a *Stage III* source (Andrews and Williams, 2005, 2007).

As the surrounding dust envelope dissipates, the accretion process ends, and the central ball of gas becomes a *pre-main-sequence* star (Greene, 2001). During their early stages (the first few million years), pre-main sequence objects are referred to as *T Tauri* stars, the youngest objects observable at optical wavelengths. T Tauri stars are still surrounded by a disk of gas and dust, referred to as the *protoplanetary disk*. After dispersing gas and dust for several million years, a bare pre-main sequence star remains in the center of the protoplanetary disk. The planets, moons, asteroids, and comets (the focus of this study) that make up our solar system all formed in such a disk. It is important to note that most planet formation happens during Stage II of protostar evolution. At this stage, the protostar has lost most of its developing envelope and is surrounded by a large disk, which provides a large reservoir for the formation and evolution of planetesimals.

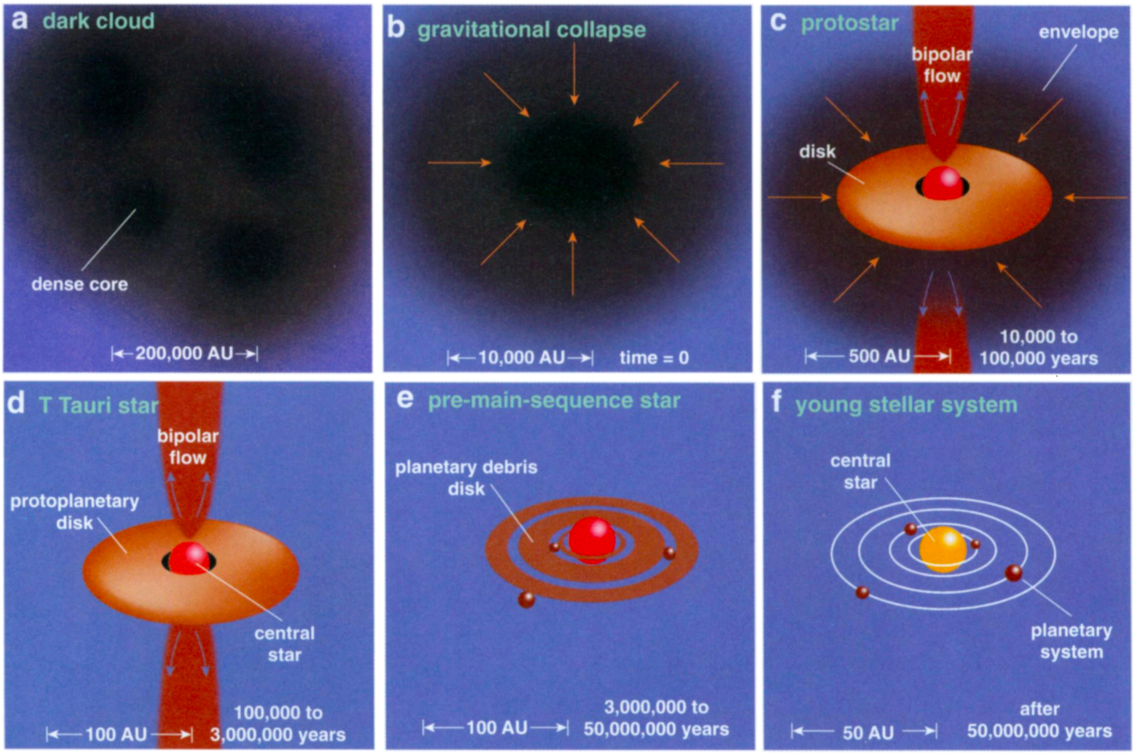

Figure 1.1. Evolutionary stages of a young, Sun-like star. The dense cores of molecular clouds [a] undergo gravitational collapse [b] to form a protostar [c]. As the envelope of dust and gas surrounding the protostar dissipates, the object first appears as the Tauri star at optical wavelengths [d]. As the dusty circumstellar disk fades away, a pre-main sequence star (with a debris belt sometimes containing recently formed planets orbiting the star) remains at its center [e]. As the star continues to collapse due to gravity, its core temperature rises and causes nuclear fusion to occur, transforming it into a main sequence star [f]. The Figure was taken from Greene (2001).

1.3. STUDY OF INTERSTELLAR MOLECULAR CO GAS

Information about star-forming gas can be obtained from studying the observations of rotational transitions of the CO molecule. The most abundant element in the interstellar medium is hydrogen, and at densities where stars form, hydrogen is in the form of molecular (H_2). However, molecular hydrogen cannot be observed directly since it has no rotational or vibrational transitions at the cold (~10 K) temperature of the interstellar medium where stars form.

Thus, observation of the rotational CO lines, the second abundant molecule in the ISM (after H_2), can be utilized as a proxy in the study of star-forming gas since it has transitions at the low temperatures found in molecular clouds. Chapter 2 of this dissertation is devoted to analyses of observations of molecular CO absorption lines in the spectra of several Young Stellar Objects (containing objects in the evolutionary stages from 0 to III) to tie them to the dense star formation conditions in the Interstellar Medium.

1.4. FORMATION OF THE SOLAR SYSTEM

As discussed above, the gravitational collapse of dense cores of molecular clouds leads to protostar formation in a time scale of $\sim 10^5$ years (e.g., Greene, 2001; Krumholz, 2015), eventually forming the protoplanetary disk from which the planets and other small objects around a star subsequently form. In the case of our solar system, the disk of material (gas and dust) out of which all the planets and small bodies (Kuiper belt objects, asteroids, and comets) were formed is referred to as the protosolar nebula. Thus, knowledge of the initial composition of the solar nebula is crucial for understanding the history and evolution of our solar system. As discussed below, comets provide a rare opportunity to learn about the properties and composition of the protosolar nebula, which would not be accessible otherwise. Figure 1.2 is a cartoon illustrating the various processes thought to affect chemistry in the protoplanetary disk.

1.4.1. Comets. Comets are among the small bodies that are leftovers from the formation time of our solar system. Because of their small size, comets lack gravitational heating, which makes them retain volatile ices from where they formed (~5-50 AU from the Sun), representing the volatile composition of the protoplanetary disk at the time of its formation (Bockelée-Morvan et al., 2004; Mumma and Charnley, 2011).

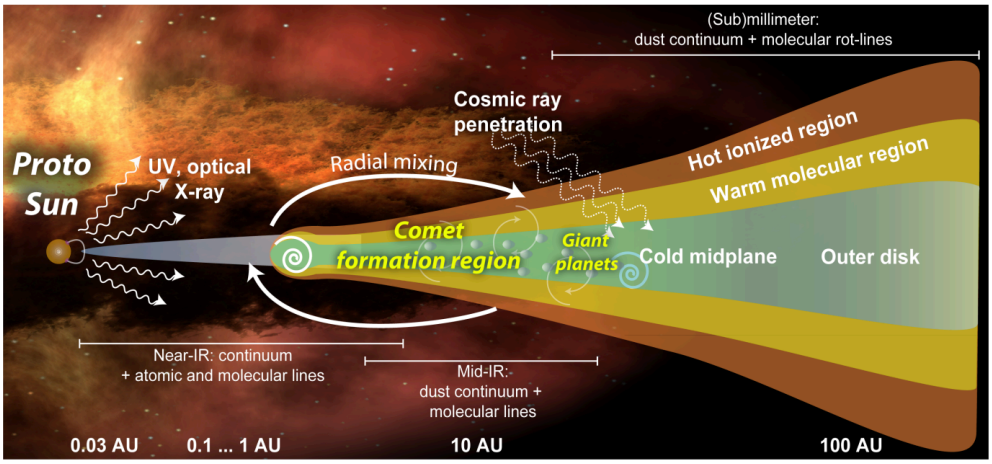

Figure 1.2. The protoplanetary disk. The formation region of comets and the processes thought to affect the chemical composition are shown. Fig. Credit: Geronimo Villanueva.

Once scattered out of the inner solar system by giant planets during their formation, comets are stored in their current, distant regions where the temperature is very low. A spectroscopic study of the composition of comets as they come inside the inner solar system is a valuable tool for gaining insights into the composition and processing of ices in the protosolar nebula.

1.4.2. Dynamical Reservoirs of Comets. The Kuiper belt (KB) and the Oort cloud (OC) are the present-day reservoirs that supply comets to the inner solar system. Figure 1.3 shows the locations of the KB and OC regions with respect to the locations of the planets and the Sun. Once comets enter the inner solar system due to planetary perturbations and collisions (from the KB region) or, in the case of OC comets, due to gravitational interaction from a nearby star or the galactic gravitational field (Stern, 2003), they are classified into two major categories. This classification is based on the Tisserand Parameter (T), which is the measure of the gravitational influence of Jupiter on the orbit of the comet (e.g., Levison, 1996).

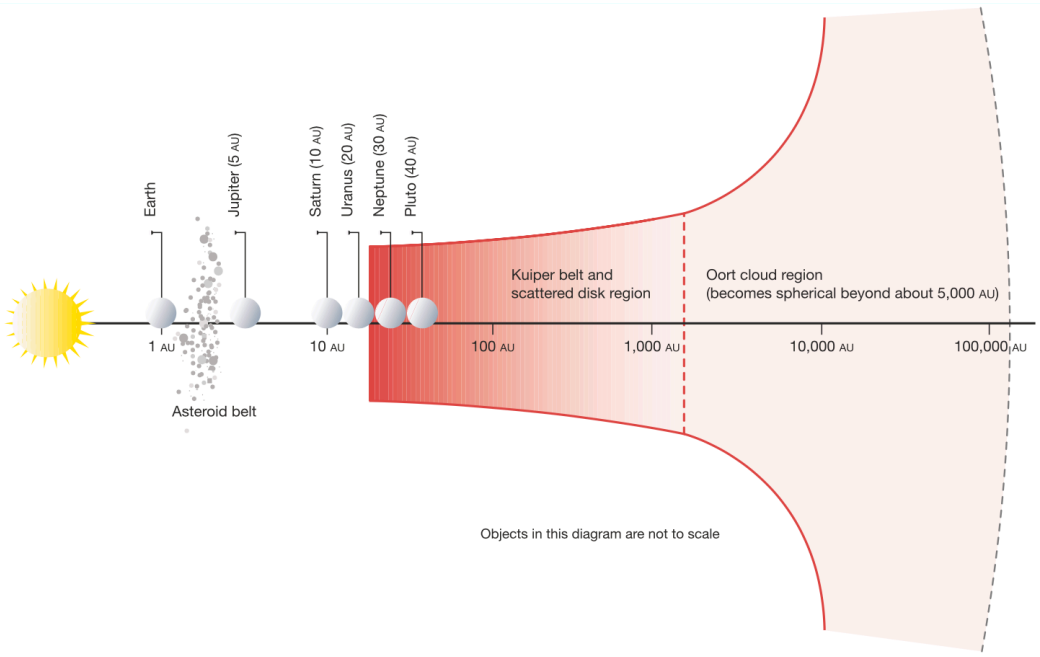

Figure 1.3. Kuiper Belt and Oort Cloud to scale with the planetary system. The figure was taken from Stern (2003).

For a comet with semi-major axis a, eccentricity e, and inclination i with respect to the orbital plane of Jupiter, the Tisserand parameter with respect to Jupiter is $T_J = \frac{a_J}{a} + 2\cos(i)\left[(1-e^2)\frac{a}{a_J}\right]^{\frac{1}{2}}$, where $a_J \sim 5.2$ AU is the semi-major axis of Jupiter. Comets with $T_J < 2$ are categorized as *nearly isotropic comets* (NICs), and those with $2 < T_J < 3$ are classified as *ecliptic* (those whose orbits are near the plane of the solar system). NICs include Halley-type comets (HTCs), which have orbital periods ≤ 200 years, and returning long-period comets (LPCs). Jupiter-family comets (JFCs) have orbital periods of < 20 years and are in the category of ecliptic comets. It is worth noting that the Encke-type comets have $T_J > 3$ (Nesvorný et al., 2017) but due to their orbits lying in the plane of the solar system, they are in the category of ecliptic comets.

The source of ecliptic comets is the KB region (Nesvorný et al., 2017). The NICs originate from the OC region (Vokrouhlický et al., 2019) and are called Oort cloud comets (OCCs). OCCs are weakly gravitationally bound to the Sun due to their large distance (≥ 1000 AU). The two comets presented in this study are the long-period comets C/2020 S3 (Erasmus) and C/2017 K2 (Pan-STARRS), which are from the OC region. Thus, due to their infrequent passage through the inner solar system, the volatile composition contained in the comae of these long-period comets is expected to be relatively well-preserved and thus offer insight into the initial chemical composition of our solar system.

1.4.3. Taxonimical Classification of Comets Based on Composition. Observations have shown that even comets within the same dynamical class were found to exhibit distinctly different compositions (e.g., Bockelée-Morvan et al., 2004), making the taxonomical classification of comets based on dynamical type not unique. In addition, crystalline silicates have been detected in some comets from both dynamical classes, such as 81P/Wild 2 (Zolensky et al., 2006), and C/2001 Q4 (Wooden et al., 2004), 9P/Tempel 1 (Harker et al., 2005), and 1P/Halley (Bregman et al., 1987), which implies that hot material from the inner disk and hypervolatiles from the cold outer disk were incorporated into their nuclei, as well as the results of dynamical disk models (e.g., Levison et al., 2011; Morbidelli et al., 2005; Nesvorný et al., 2017), have revealed a more "spatially mixed" comet formation region. Furthermore, studies that combine the protoplanetary disk (PPD) astrochemical models with near-IR comet composition show that no single time or place can explain the range of molecular abundances found in comets, indicating that comets have incorporated material from wide temporal and spatial stretches in the disk (e.g., Willacy et al., 2022). As a result, the taxonomical classification of comets based on their chemical composition was pursued to build a unique taxonomic classification.

Optical observations of comets based on product species such as OH, C_2, C_3, NH, and CN have led to the classification in terms of whether the comet is depleted or typical in *carbon-chain* molecules (e.g., A'Hearn et al., 1995).

These product species are primarily created in the cometary coma by chemical interactions between coma gases, photolysis and photoionization of gaseous precursors, and degradation of refractory organics on grains (Mumma and Charnley, 2011). However, these product species may come from more than one precursor, making taxonomical classification based on the abundance of daughter species difficult and less conclusive. Therefore, compositional measurements of the primary volatile species (molecules that sublimate directly from the nucleus, indicating its native composition) such as H_2O, C_2H_6, CH_4, CH_3OH, H_2CO, NH_3, HCN, C_2H_2, CO, and OCS are needed in an effort to develop a better taxonomical classification of comets based on chemical composition.

These primary volatile species can be measured at radio (covering sub-mm/mm) or near-infrared (NIR, covering ~2.8- 5.2 μm) wavelength regions. Observations of asymmetric molecules that have pure rotational transitions (e.g., H_2CO, CO, CH_3OH, HCN, and NH_3) can be carried out in the radio and NIR wavelength regimes, while complex molecules such as ethylene glycol ($HOCH_2CH_2OH$) are more easily detectable in the radio than in the NIR (Mumma and Charnley, 2011). A pure rotational transition occurs in a molecule that has a permanent dipole moment due to an asymmetric charge distribution (e.g., Tennyson, 2011). On the other hand, symmetric molecules like CO_2, CH_4, C_2H_2, and C_2H_6 do not have permanent dipole moments and can only be detected in the NIR wavelength region via their ro-vibrational transitions. It is worth noting that CO_2 can only be observed from space due to telluric absorption at the wavelengths where its strongest features occur.

Radio observations have shown that while comets exhibit substantial chemical diversity, there are no distinct differences between comets of different dynamical classes (Crovisier et al., 2009). In the NIR, measurements based on 26 comets (both ecliptic and nearly isotropic) showed three compositional groupings (Mumma and Charnley, 2011): organics-normal, organic-enriched, and organics-depleted.

Subsequent observations showed some comets are outliers in terms of chemical abundances due to outbursts or disintegration during their observations, and Dello Russo et al. (2016a) analyzed observations of 30 comets (both JFCs and OCCs) in the NIR and suggested four major groups and eleven subgroups of chemical taxonomy based on primary molecules. Thus, this indicates that observations of a large sample of comets are needed to build a comprehensive chemical taxonomy in the NIR.

The emission lines of primary molecules in NIR wavelengths are observed by detecting photons produced during their ro-vibrational transitions. In general, molecules are excited by solar radiation from the rotational levels of the ground vibrational states (ν = 0) to the rotational levels in the higher vibrational states (ν = 1, 2, 3, ...) (see e.g., DiSanti et al., 2006; Paganini et al., 2013). These excited molecular levels eventually cascade (fluoresce) to rotational levels in the ground vibrational state by releasing detectable photons. This spontaneous decay can be estimated by calculating the fluorescence efficiencies (g-factors) using statistical weights, absorption line strengths, Einstein A-coefficients, and the total partition function.

The chemical taxonomy of comets in the near-infrared (NIR) is usually carried out using the molecular abundance or mixing ratio (%) of the volatile species, which is the ratio of the production rate of a given molecular species to that of simultaneously measured H_2O. The choice of H_2O as a baseline in calculating the mixing ratio is because it is the most abundant species in the coma of active comets, and cometary activity, especially within 2.0 AU, is thought to be driven by sublimation of H_2O.

The mixing ratios of different volatile species are a good measure in comets as they can provide information such as formation temperature and processing histories of cometary volatile ices (e.g., Mumma et al., 1993). H_2O has a sublimation temperature of ~150 K, making it the least volatile ice in the cometary coma, followed by CH_3OH with a sublimation temperature of ~ 99 K (e.g., Crovisier et al., 2000).

If comet nuclei are homogeneous, once the least volatile species (such as H_2O, CH_3OH, and HCN) are fully activated, volatile abundances should reflect the true composition of the nucleus (e.g., Bonev, 2005; Roth, 2019). However, variability in mixing ratios in some comets has been observed.

For example, Roth et al. (2018) measured the volatile composition of comet 2P/Encke on three post-perihelion dates and reported mixing ratios that are depleted in volatile species CH_3OH, C_2H_6, and CH_4 and enriched in H_2CO and HCN compared to values obtained by Radeva et al. (2013) for the same comet during a different apparition. The possible causes for this discrepancy between apparitions could mainly be due to the comet being compositionally heterogeneous and its different parts observed during each apparition (seasonal differences) or potential evolutionary changes in composition due to multiple perihelion passages. In addition, some comets such as D/2012 S1 (ISON) observed close to the Sun (< 0.80 AU) have shown enrichment in abundances of some volatile species such as H_2CO, NH_3, HCN, and C_2H_2 (Dello Russo et al., 2016b; DiSanti et al., 2016) compared to measurements of the same comet taken at heliocentric distances greater than 0.80 AU from the Sun, possibly due to activation of additional contributing sources in the coma closer to the Sun. Along this line, observations of comet C/2020 S3 (Erasmus), one of the main subjects of this work, at heliocentric distance of ~ 0.50 AU has shown enhancement in the abundances of H_2CO, NH_3 and C_2H_2 compared to their mean abundances from OCCs observed at heliocentric distance greater than 0.80 AU from the Sun. Thus, this necessitates observations of comets over a wider range of heliocentric distances to investigate whether the abundances of volatile species in a given comet remain constant or enhanced as the comet gets closer to the Sun, as with D/2012 S1 (ISON).

As pointed out earlier, cometary activity within ~ 2.0 AU from the Sun is driven by the sublimation of H_2O ice. However, there are a few comets, such as C/2006 (Christensen), C/2016 R2 (Pan-STARRS), C/1995 O1 (Hale-Bopp), C/2009 P1 (Garradd), and C/2017 K2 (Pan-STARRS) another main subject of this study, that showed activity well beyond the sublimation distance of H_2O.

Thus, cometary activity beyond a heliocentric distance of ~2.5 AU is generally thought to be driven by the sublimation of hypervolatiles such as CO and CO_2. As mentioned above, since CO_2 is not detectable using ground-based observations, for comets observed beyond the activation regime of H_2O, CO is usually used as a baseline to compute the mixing ratio of the simultaneously measured volatile species. In particular, comets C/2006 (Christensen) (Bonev et al., 2017) and C/2016 R2 (Pan-STARRS) (McKay et al., 2019) have shown that they are CO-rich comets at the heliocentric distances of their observations.

The studies presented in the next two sections consist of observations of two Oort Cloud comets, one at a small heliocentric distance (R_h) of ~ 0.50 AU, and one at R_h beyond ~ 2.3 AU from the Sun. These observations aim to investigate the effect of heliocentric distance on compositional measurements in comets, thereby adding a crucial sample towards building a comprehensive database for the chemical taxonomy of comets. In particular, the compositional measurements of comet C/2017 K2 beyond ~ 2.3 AU presented in this study covered a wider range of heliocentric distances to address the effect of snapshot bias since most comets are observed over a narrow range of heliocentric distances.

2. ANALYSES OF SPECTRA OF YOUNG STELLAR OBJECTS

2.1. THE L1688 CLOUD

The L1688 cloud of the Rho Ophiuchi molecular complex (Figure. 2.1), one of the closest active star-forming regions, is estimated to be 137 ± 1.2 pc away (Loinard et al., 2008; Lombardi et al., 2008; Mamajek, 2008; Ortiz-León et al., 2017). This cloud is located near the Sco-Cen OB association, which may have compressed and initiated star formation in L1688 (Wilking et al., 2008). Within this cluster are more than 300 known YSOs, and about 55 prestellar cores have been identified that could be collapsing (André et al., 2007). Given that most of the objects in Rho Ophiuchi have masses of approximately ≤ 1 $M_{\odot}$, the Rho Ophiuchi star-forming region is linked to the formation and evolution of low-mass objects. The L1688 molecular cloud is an interesting location for studying star and planet formation because it is close by, relatively young (0.5–2 Myr), and contains a significant number of confirmed (candidate) members (Wilking et al., 2008). The B2V pre-main sequence star HD147889 with an estimated mass of $\sim$10 $M_{\odot}$ (Figure. 2.2) illuminates the L1688 cloud and creates a photodissociation region (where H_2 is decomposed into H atoms and H^+ by UV photons) that delineates the western edge of the molecular cloud (Kulesa et al., 2005).

2.2. OBSERVATIONS

The observations of young stellar objects (YSOs) within the L1688 embedded cluster were acquired using the iSHELL instrument of the NASA Infrared Telescope Facility (IRTF) in Maunakea, Hawaii. iSHELL is a cross-dispersed, high-resolution, echelle infrared spectrograph (Rayner et al., 2022). We used the iSHELL K2 mode for our observations, which covers a wavelength range of 2.084-2.382 μm over 32 orders. Table 2.1 shows the sources we analyzed.

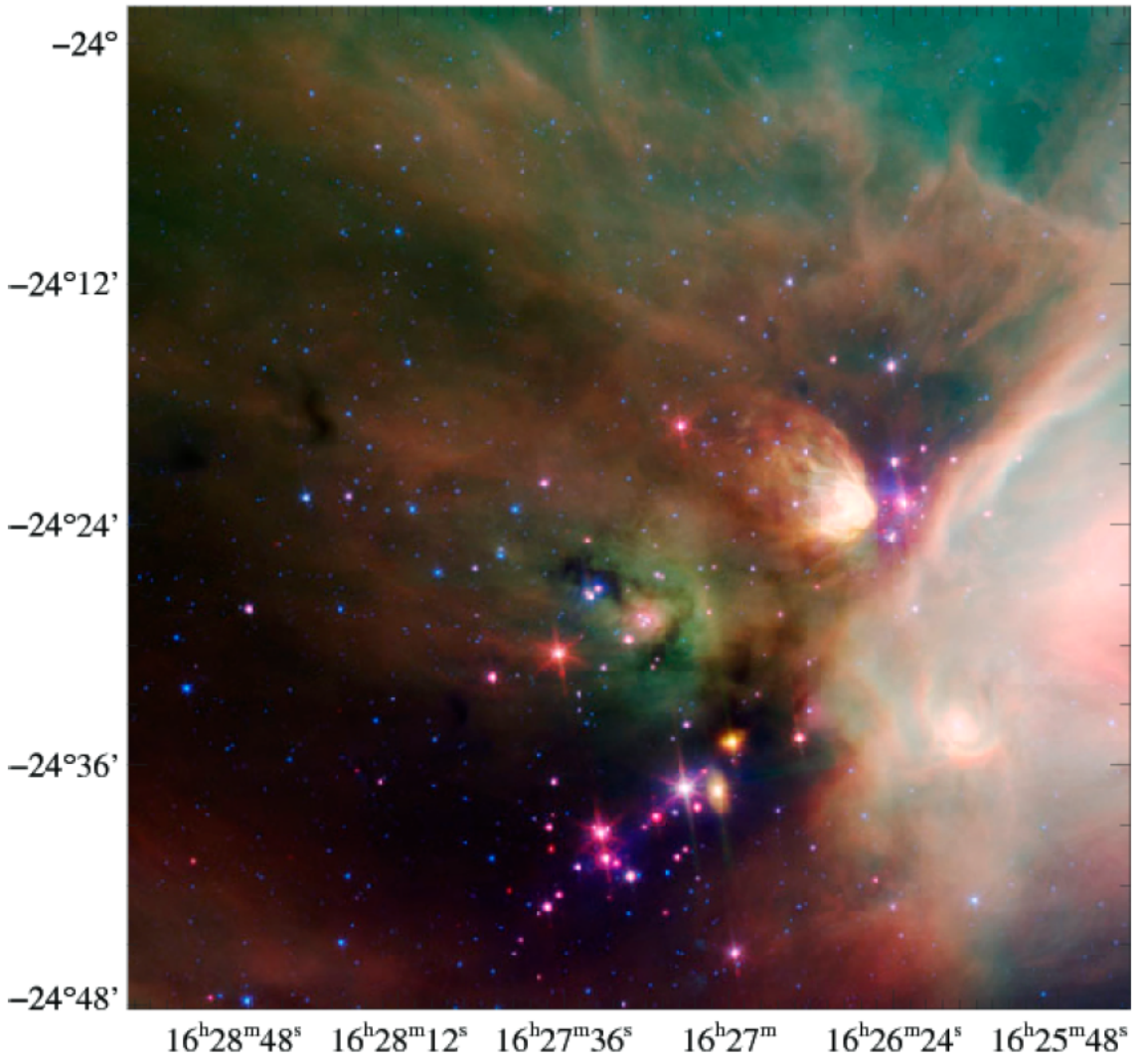

Figure 2.1. The Spitzer Space Telescope image of the L1688 cloud. The image was taken with the Infrared Array Camera (IRAC) and Multiband Imaging Photometry (MIPS) instruments. The red color represents emission in the MIPS 24 μm band, the green color represents the IRAC 8 μm band, and the blue color represents IRAC 4.5 μm. The Photodissociation Region (PDR) is indicated in red on the lower right region. The image was taken by Robert Hurt. The figure is taken from Wilking et al. (2008).

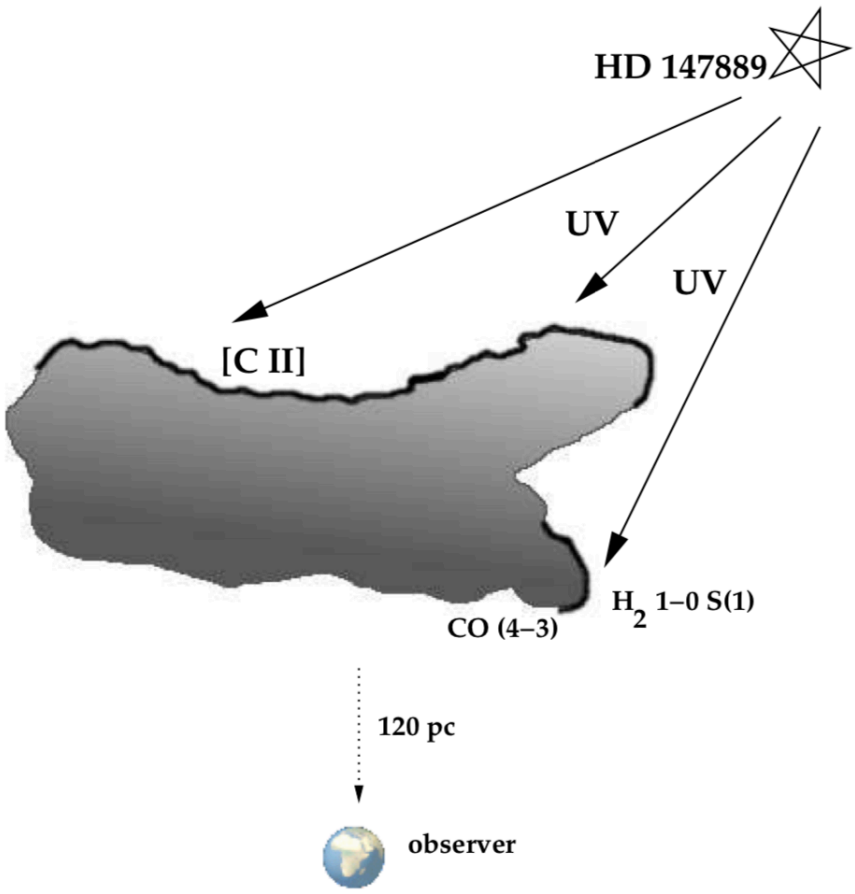

Figure 2.2. Schematic diagram of the ρ Oph dark cloud. The Photo-dissociation Region surfaces are highlighted in black. Fig taken from Kulesa et al. (2005).

Sources were selected based on their infrared brightness (K-magnitudes) and their early *Stage* of evolution (Sullivan et al., 2019). Thus, the K magnitude brightness ($\lambda = 2.2\,\mu m$) of our sources is $\leq$ 10 mag. All the sources used in the analyses of the interstellar absorption lines have completed the main accretion phase or *Stage 0*. The spectra of these YSOs, with the exception of WLY 2-54, showed photospheric absorption lines that are weak or absent in the *longer wavelength orders*. Instead, very narrow interstellar absorption lines, identified to be from the *R* and *P* branch of the CO v = 0 - 2 transitions, were observed (Fig. 2.3).

We have identified these lines in *eight* of our YSOs, mainly in orders 218 (2.37 μm to 2.38 μm), 219 (2.36 μm to 2.37μm), 220 (2.35μm to 2.36 μm), 221 (2.34 μm to 2.35 μm), and 222 (2.33 μm to 2.34 μm).

2.3. DATA REDUCTION

We reduced the data using the latest version of `Spextool` (Spectral Extraction Tool), V5.0.2. Spextool is an Interactive Data Language (IDL)–based data reduction package developed to reduce data obtained with iSHELL (Cushing et al., 2004). The reduction steps include dark subtraction, flat-fielding, wavelength calibration using a ThAr arc lamp, extracting the spectrum, telluric correction using an A0 standard star spectrum, combining extracted spectra to increase the signal-to-noise ratio of the final spectra, and finally, cleaning (and smoothing) spectra. The detailed procedure of data reduction is discussed in the appendix.

Table 2.1. The iSHELL observing Log of YSOs

Source	R. A. (J2000) (hhmmss.s)	Decl. (J2000) (° ′ ″)	Date (UT)	Int. Time (minutes)	Evol. Stage
VSSG 1	16 26 18.9	-24 28 19.7	2017 Apr 26	30	II
GY33	16 26 27.5	-24 41 53.5	2017 Apr 28	60	I
SR 24S	16 26 58.5	-24 45 36.9	2017 Apr 26	30	II
GY 235	16 27 13.8	-24 43 31.7	2017 Apr 27	60	I
WL 20E	16 27 15.9	-24 38 43.4	2017 Apr 28	60	I
WL 4	16 27 18.5	-24 25 05.9	2017 Apr 27	30	I
WLY 2-51	16 27 39.8	-24 43 15.1	2017 Apr 26	30	I
WLY 2-54	16 27 51.8	-24 31 45.5	2017 Apr 26	30	I

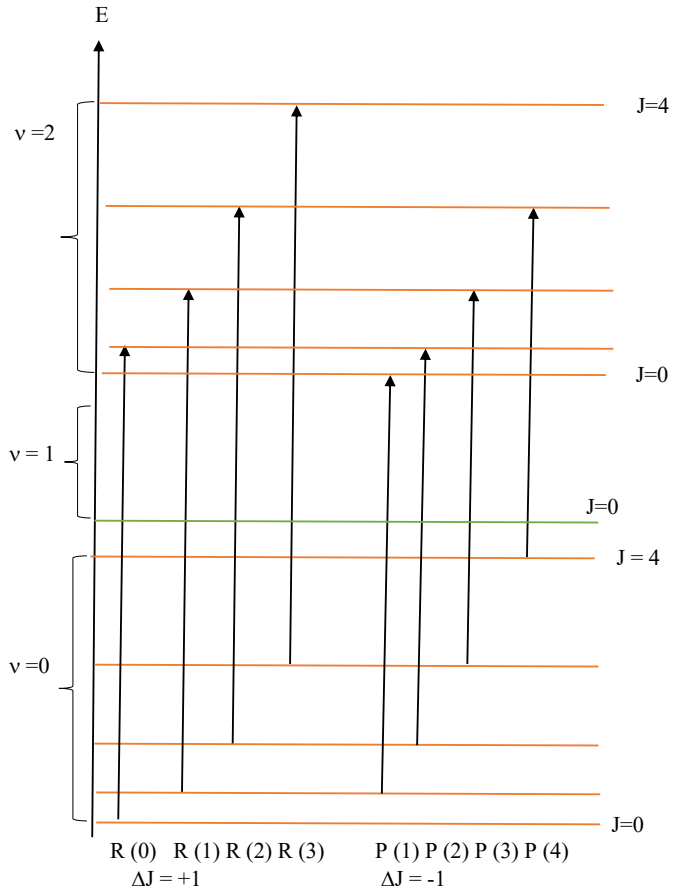

Figure 2.3. Ro-vibrational transition in a diatomic molecule. Vibrational excitation from rotational levels in the ground vibrational band ($v = 0$) to rotational states in the $v = 2$ vibrational band. The band spectrum contains the *R* and *P* branches with rotational levels obeying the selection rules $\Delta J = +1$ and $\Delta J = -1$, respectively. The lines in each branch: R(0), R(1), ... ; P(1), P(2), ..., are labeled by the *J* values of the lower rotational levels.

2.4. ANALYSES OF THE ABSORPTION SPECTRAL LINES

2.4.1. Measuring the Equivalent Widths of the Absorption Lines. The equivalent width of an absorption line expressed in wavelength units (e.g., μm) is the width from the adjacent continuum to zero intensity with the same area taken up by the absorption line. The equivalent widths of the spectral lines must be measured to calculate the column density and temperature.

The spectrum must be normalized (divided by the continuum level) before measuring equivalent width. Measurement of an equivalent width can be accomplished by fitting a Gaussian to the absorption line using the standard package Image Reduction and Analysis Facility (IRAF[1]) which returns the line center, equivalent width along with its uncertainty, and Gaussian Full Width Half Maxima (gFWHMs).

2.4.2. Column Density Calculation. Column density is the number of atoms per unit area in the line of sight in the initial (lower) transition level that produces an absorption line. Thus, the column density of a line in a lower state (in cm^{-2}) for each transition determined from a measurement of the equivalent width is given as:

$$N_{J''} = \frac{W_\lambda}{f\lambda^2(8.853 \times 10^{-13})}, \tag{2.1}$$

where $8.853\times\ 10^{-13}\ cm$ is the classical electron radius, f is the dimensionless oscillator strength of the transition, W_λ is the equivalent width of the line in units of cm, and J″ represents the lower state.

2.4.3. Fractional Population. The fractional population, $\frac{N_{J''}}{N_{tot}}$, is the contribution of each transition to the total population of the gas and is given as:

$$\frac{N_{J''}}{N_{tot}} = \frac{2J''+1}{Q_{tot}} e^{\frac{-hcBJ''(J''+1)}{kT}}, \tag{2.2}$$

where $Q_{tot} \approx \frac{kT}{hcB}$ is the total partition function of a diatomic molecule, k is the Boltzmann constant, T is the temperature, h is the Planck's constant, c is the speed of light, $B = \frac{h}{8\pi^2 Ic}$ is the rotational constant in cm^{-1}, and I is the moment of inertia about the center of mass of the rotating diatomic molecule.

[1]IRAF is distributed by the National Optical Astronomy Observatory, which is operated by the Association of Universities for Research in Astronomy, Inc., under a cooperative agreement with the National Science Foundation.

2.5. TEMPERATURE DETERMINATION FOR THE INTERSTELLAR GAS

2.5.1. Model Fits to the Spectral Absorption Lines. The FITROT model that calculates the rotational temperature of infrared spectral observations was applied to model the interstellar CO absorption lines. The model is written in Interactive Data Language (IDL) and was initially developed at NASA Goddard Space Flight Center. Spectral regions containing the absorption lines were selected to fit the model to the observed spectra. Because a Gaussian line profile better describes the absorption lines, models were convolved to a Gaussian profile line shape. The FITROT model simultaneously fits all the selected absorption lines and is sensitive to baseline fit over 1 to 2 orders. The model is compared to the data through a correlation coefficient ℓ, the difference between the model and the data. The total column density corresponding to the best-fit temperature is computed from the retrieved column densities of each absorption line at the best-fit temperature. It was assumed that the gas was in local thermodynamic equilibrium and optically thin.

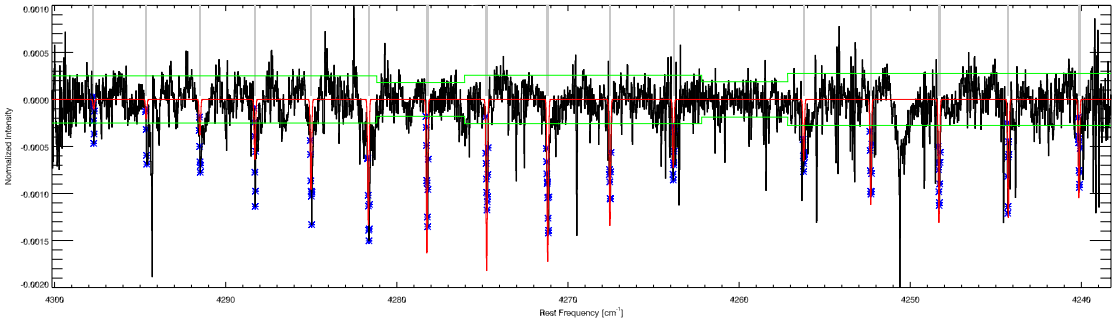

Figure 2.4. FITROT best-fit temperature model to SR 24S spectra. The data consists of combined orders 220, 221, and 222 of the SR 24S spectra. The blue color indicates the pixels (lines) selected, the black is the data, and the red is the model.

2.5.2. Linear Least Square Method of Determining the Gas Temperature . An estimate of the rotational excitation temperature can be obtained by examining the quantity $\frac{N_{J''}}{N_{tot}}$ described in Equation 2.2.

Table 2.2. FITROT Results

Source	Order[a]	Tran.	T_{rot} (K)	N_{tot} ($\times 10^{17}$ cm^{-2})	ℓ
VSSG 1	220 & 221	R_4-R_0, P_1-P_3	22 ± 3	9.22 ± 0.49	0.86
	222	R_{10}-R_5	168^{+85}_{-49}	18.9 ± 1.9	0.45
GY 33	220 & 221	R_4-R_0, P_1 - P_3	56 ± 12	36.5 ± 3.9	0.57
	222 & 219	R_{10}-R_5, P_5-P_9	154^{+54}_{-29}	90.7 ± 4.8	0.80
SR 24S	220, 221 & 222	R_{10}-R_5, R_4-R_0 , P_1-P_5	69^{+8}_{-10}	20.1 ± 1.0	0.56
GY 235	220 & 221	R_4 - R_0, P_1 - P_4	24^{+9}_{-6}	18.1 ± 1.8	0.79
WL 20E	220 & 221	R_4 - R_0, P_1-P_3	19^{+10}_{-5}	18.1 ± 2.2	0.66
WL 4	220 & 221	R_4-R_0, P_1-P_3	22^{+7}_{-5}	24.4 ± 2.5	0.77
WLY 251	220 & 221	R_4-R_0, P_1-P_3	22^{+7}_{-5}	15.7 ± 1.6	0.81
WLY 2-54	220, 221 & 222	R_7-R_5, R_4-R_0 , P_1-P_4	31^{+15}_{-7}	28.7 ± 2.7	0.89

[a] Order 219: 2.36 - 2.37 μm; order 220: 2.35-2.36 μm; order 221: 2.34 - 2.35 μm; order 222: 2.32-2.34 μm.

Assuming local thermodynamic equilibrium (LTE), the excitation temperature can be determined by fitting the derived column densities from the Boltzmann equation. Equation 2.2 can be written as:

$$\ln\left(\frac{N_{J''}}{2J''+1}\right) - \ln\left(\frac{N_{tot}}{Q_{tot}}\right) = -\frac{hcBJ''(J''+1)}{kT} \tag{2.3}$$

Assuming the excitation temperature is constant, the above equation is linear. The term $\ln\left(\frac{N_{tot}}{Q_{tot}}\right)$ is a constant; the term on the right-hand side is the ratio of rotational energy of the state, $E_{J''}$ (in Joules), to the thermal energy, kT. Thus, Eq. 2.3 becomes $\ln\left(\frac{N_{J''}}{2J''+1}\right) = -\frac{E_{J''}}{kT} + constant$, which is an equation of the form y = mx +b, where $x = \frac{E_{J''}}{k}$, b = $\ln\left(\frac{N_{tot}}{Q_{tot}}\right)$, and the slope $m = -\frac{1}{T}$. Hence, by fitting a first-order polynomial to a plot of $\ln\left(\frac{N_{J''}}{2J''+1}\right) vs\ \frac{E_{J''}}{k}$, the negative reciprocal of the slope will yield the temperature of the gas. If a straight line does not represent the plot of the above equation, this could be due to optical depth effects or due to possible variation in the temperature or excitation mechanism within the emitting medium (e.g., Kwok, 2007).

The uncertainty on the quantity, $\ln\left(\frac{N_{J''}}{2J''+1}\right)$, can be determined using the general equation of the form $x = a\ln(bu)$ whose uncertainty is given by $\sigma_x = \frac{ab}{u}\sigma_u$. Thus, the uncertainty on the above quantity is given as: $\left[\frac{1}{N_{J''}(2J''+1)}\right]\sigma_{N_{J''}}$. The correlation coefficient, ℓ (an indicator of the goodness of fit), and the uncertainties on the temperature were derived from a linear least-square curve fitting program `LINEST`; the value of ℓ close to **1** shows a good fit of the model to the data.

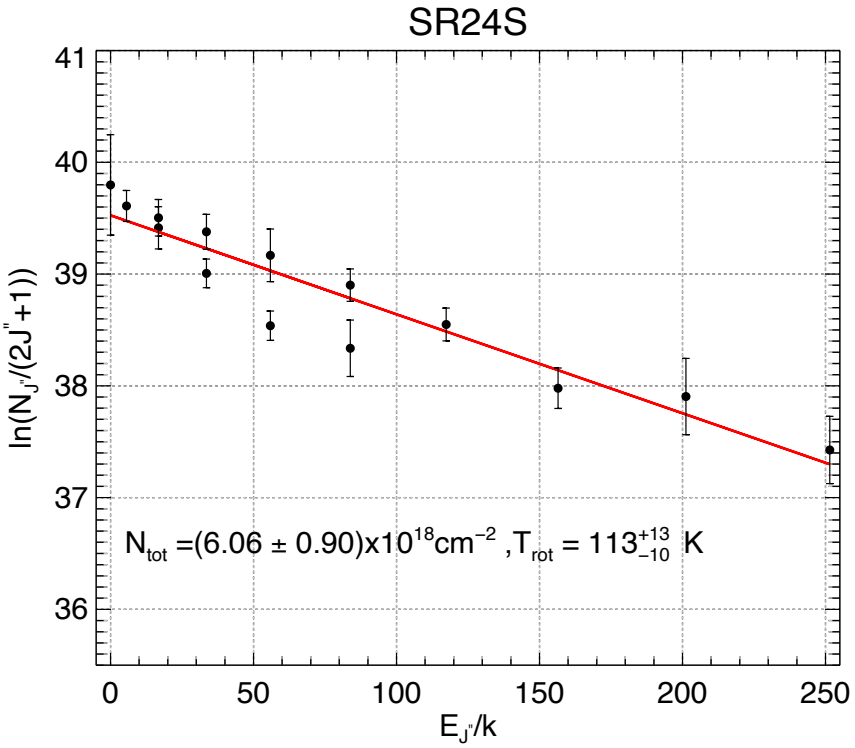

Figure 2.5. Temperature determination for SR 24S using the Linear Least-Square technique. The data consists of combined orders 220, 221, and 222 of the SR 24S spectra.

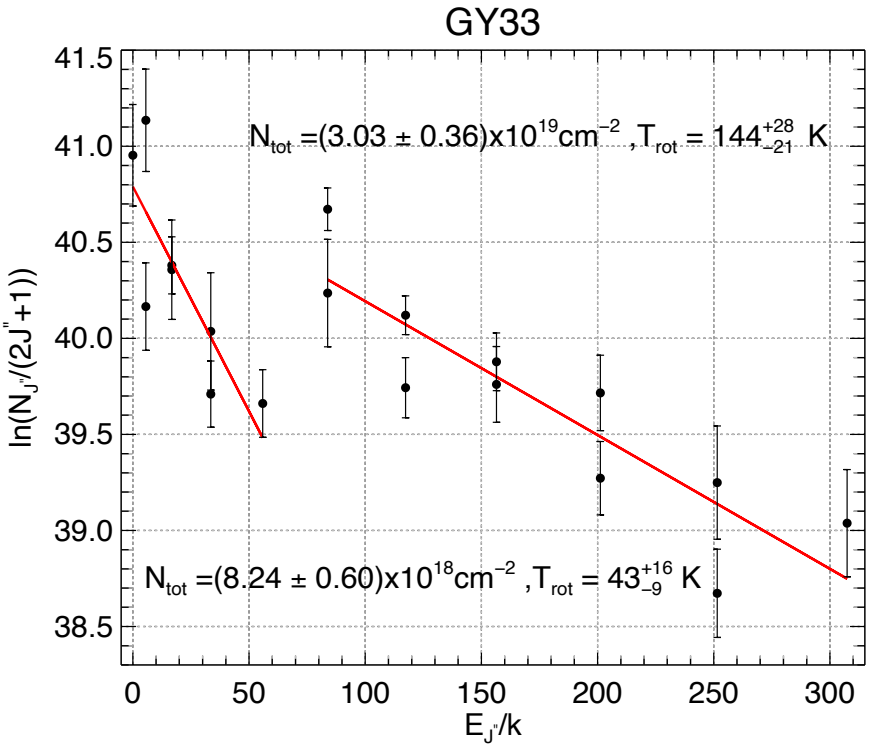

Figure 2.6. Temperature determination for GY 33 using the Linear Least-Square technique. The same as Fig. 2.5 but for GY 33 indicating that low-J transition lines having higher slope (colder temperature) and high-J transition lines have lower slope (hotter temperature).

Table 2.3. The derived Temperatures using Linear Least Squares fits

Source	**Tran.**	$\mathbf{W}_\lambda$ ($\times 10^{-6}$ μm)	$\ln\left(\frac{N_{J''}}{2J''+1}\right)$	$\frac{E_{J''}}{k}$	$\mathbf{T}_{rot}$ (K)	ℓ
VSSG 1	P_1	5.80 ± 1.13	40.05± 0.20	5.59		
	P_2	5.22 ± 1.27	39.26 ± 0.24	16.77		
	P_3	3.34 ± 1.10	38.42 ± 0.33	33.53		
	R_4	2.89 ± 1.33	37.74 ± 0.46	55.89		

Continued on next page

Table 2.3 The derived Temperatures using Linear Least Squares fits (cont.)

Source	**Tran.**	$\mathbf{W}_\lambda$ ($\times 10^{-6}$ μm)	$\ln\left(\frac{N_{J''}}{2J''+1}\right)$	$\frac{E_{J''}}{k}$	$\mathbf{T}_{rot}$ (K)	ℓ
	R_3	4.78 ± 1.00	38.46 ± 0.21	33.53		
	R_2	12.5 ± 1.1	39.72 ± 0.09	16.77		
	R_1	6.36 ± 1.01	39.45 ± 0.16	5.59		
	R_0	7.07 ± 1.19	40.25 ± 0.17	0.00		
					22^{+3}_{-2}	0.96
	R_{10}	6.98 ± 2.01	37.79 ± 0.29	307.39		
	R_9	6.07 ± 1.94	37.74 ± 0.32	251.50		
	R_8	8.54 ± 1.21	38.20 ± 0.14	201.20		
	R_7	9.06 ± 4.80	38.38 ± 0.53	156.49		
	R_6	8.79 ± 1.47	38.49 ± 0.17	117.37		
	R_5	8.61 ± 1.55	38.63 ± 0.18	83.83		
					236^{+37}_{-29}	0.96
WLY 2-54	P_1	14.8 ± 1.3	40.99 ± 0.09	5.59		
	P_2	13.2 ± 1.3	40.18 ± 0.10	16.77		
	P_3	12.5 ± 1.1	39.74 ± 0.08	33.53		
	P_4	6.74 ± 1.19	38.82 ± 0.18	55.89		
	R_4	12.0 ± 2.0	39.16 ± 0.17	55.89		
	R_3	15.4 ±1.5	39.63 ± 0.10	33.53		
	R_2	20.2 ± 1.5	40.20 ± 0.07	16.77		
	R_1	16.2 ± 1.2	40.39 ± 0.07	5.59		
	R_0	13.6 ±1.2	40.91 ± 0.09	0.00		
	R_7	5.22 ± 1.91	37.83 ± 0.37	156.49		
	R_6	8.84 ± 1.24	38.50 ± 0.14	117.37		

Continued on next page

Table 2.3 The derived Temperatures using Linear Least Squares fits (cont.)

Source	**Tran.**	$\mathbf{W}_\lambda$ ($\times 10^{-6}$ μm)	$\ln\left(\frac{N_{J''}}{2J''+1}\right)$	$\frac{E_{J''}}{k}$	$\mathbf{T}_{rot}$ (K)	ℓ
	R_5	13.6 ± 1.6	39.09 ± 0.12	83.83		
					54^{+6}_{-4}	0.94
GY 33	P_1	17.2 ± 4.6	41.14 ± 0.27	5.59		
	P_2	15.7 ± 4.1	40.36 ± 0.26	16.77		
	P_3	16.8 ± 5.1	40.04 ± 0.31	33.53		
	R_4	19.7 ± 3.5	39.66 ± 0.18	55.89		
	R_3	16.7 ± 2.9	39.71 ± 0.17	33.53		
	R_2	24.2 ± 3.6	40.38 ± 0.15	16.77		
	R_1	13.0 ± 3.0	40.17 ± 0.23	5.59		
	R_0	14.3 ± 3.8	40.95 ± 0.26	0.00		
					43^{+16}_{-9}	0.83
	P_5	33.9 ± 9.5	40.24 ± 0.28	83.83		
	P_6	24.5 ± 3.8	39.74 ± 0.16	117.37		
	P_7	37.1 ± 7.3	39.76 ± 0.20	156.49		
	P_8	20.1 ± 3.8	39.27 ± 0.19	201.20		
	P_9	22.0 ± 6.5	39.25 ± 0.30	251.50		
	R_{10}	24.4 ± 6.8	39.04 ± 0.28	307.39		
	R_9	15.4 ± 3.5	38.67 ± 0.23	251.50		
	R_8	39.1 ± 7.7	39.72 ± 0.20	201.20		
	R_7	40.6 ± 6.1	39.88 ± 0.15	156.49		
	R_6	44.9 ± 4.5	40.12 ± 0.10	117.37		
	R_5	66.1 ± 7.3	40.67 ± 0.11	83.83		

Continued on next page

Table 2.3 The derived Temperatures using Linear Least Squares fits (cont.)

Source	**Tran.**	$\mathbf{W}_\lambda$ ($\times 10^{-6}$ μm)	$\ln\left(\frac{N_{J''}}{2J''+1}\right)$	$\frac{E_{J''}}{k}$	$\mathbf{T}_{rot}$ (K)	ℓ
					144^{+28}_{-21}	0.89
SR 24S	P_2	6.66 ± 1.09	39.50 ± 0.16	16.77		
	P_3	8.68 ± 1.36	39.38 ± 0.16	33.53		
	P_4	9.51± 2.24	39.17 ± 0.24	55.89		
	P_5	5.07 ± 1.28	38.34 ± 0.25	83.83		
	R_4	6.41 ± 0.84	38.54 ± 0.13	55.89		
	R_3	8.27 ± 1.06	39.01 ± 0.13	33.53		
	R_2	9.22 ± 1.74	39.41 ± 0.19	16.77		
	R_1	7.43 ± 1.03	39.61 ± 0.14	5.59		
	R_0	4.49 ± 2.02	39.80 ± 0.45	0.00		
	R_9	4.42 ± 1.33	37.43 ± 0.30	251.50		
	R_8	6.39 ± 2.18	37.90 ± 0.34	201.20		
	R_7	6.08 ± 1.10	37.98 ± 0.18	156.49		
	R_6	9.33 ± 1.37	38.55 ± 0.15	117.37		
	R_5	11.3 ± 1.6	38.90 ± 0.15	83.83		
					113^{+13}_{-10}	0.95
GY 235	P_1	12.8 ± 1.6	40.84 ± 0.13	5.59		
	P_2	12.9 ± 1.4	40.17 ± 0.11	16.77		
	P_3	8.19 ± 2.07	39.32 ± 0.25	33.53		
	R_4	5.43 ± 2.51	38.37 ± 0.46	55.89		
	R_3	9.79 ± 1.89	39.18 ± 0.19	33.53		
	R_2	12.0 ± 1.8	39.68 ± 0.15	16.77		
	R_1	9.49 ± 1.84	39.85 ± 0.19	5.59		

Continued on next page

Table 2.3 The derived Temperatures using Linear Least Squares fits (cont.)

Source	**Tran.**	$\mathbf{W}_\lambda$ ($\times 10^{-6}$ μm)	$\ln\left(\frac{N_{J''}}{2J''+1}\right)$	$\frac{E_{J''}}{k}$	$\mathbf{T}_{rot}$ (K)	ℓ
	R_0	13.2 ± 2.3	40.87 ± 0.18	0.00	24^{+5}_{-3}	0.93
WL 20E	P_1	16.2 ± 2.4	41.08 ± 0.15	5.59		
	P_2	9.00 ± 2.02	39.81 ± 0.23	16.77		
	P_3	7.83 ± 2.48	39.28 ± 0.32	33.53		
	R_4	3.97 ± 1.42	38.06 ± 0.36	55.89		
	R_3	8.88 ± 2.24	39.08 ± 0.25	33.53		
	R_2	18.7 ± 2.4	40.12 ± 0.13	16.77		
	R_1	11.5 ± 1.8	40.05 ± 0.16	5.59		
	R_0	12.7 ± 1.8	40.84 ± 0.14	0.00	20^{+3}_{-2}	0.95
WL 4	P_1	15.4 ± 2.9	41.03 ± 0.19	5.59		
	P_2	12.6 ± 2.1	40.14 ± 0.17	16.77		
	P_3	12.5 ± 2.9	39.74 ± 0.23	33.53		
	R_3	12.8 ± 2.5	39.44 ± 0.20	33.53		
	R_2	20.2 ± 2.8	40.20 ± 0.14	16.77		
	R_1	12.8 ± 1.9	40.16 ± 0.15	5.59		
	R_0	14.9 ± 2.3	41.00 ± 0.15	0.00	26^{+8}_{-5}	0.88
WLY 2-51	P_1	12.3 ± 1.0	40.80 ± 0.08	5.59		
	P_2	8.27 ± 1.18	39.72 ± 0.14	16.77		
	P_3	7.38 ± 1.43	39.22 ± 0.19	33.53		
	R_4	4.05 ± 1.45	38.08 ± 0.36	55.89		

Continued on next page

Table 2.3 The derived Temperatures using Linear Least Squares fits (cont.)

Source	**Tran.**	$\mathbf{W}_\lambda$ ($\times 10^{-6}$ μm)	$\ln\left(\frac{N_{J''}}{2J''+1}\right)$	$\frac{E_{J''}}{k}$	$\mathbf{T}_{rot}$ (K)	ℓ
	R_3	8.43 ± 1.07	39.03 ± 0.13	33.53		
	R_2	11.6 ± 1.0	39.64 ± 0.09	16.77		
	R_1	10.1 ± 1.0	39.91 ± 0.10	5.59		
	R_0	10.3 ± 1.4	40.63 ± 0.13	0.00		
					23 ± 3	0.96

2.6. RESULTS

The spatial resolution of the interstellar gas is a pencil beam. On a much larger scale, the gas temperature and column density can be investigated using J=1-0 transitions of ^{12}CO (optically thick) and ^{13}CO (usually optically thin), respectively, from the single-dish COMPLETE survey (Ridge et al., 2006). At a resolution of 40 $''$, nearly all ^{12}CO emission lines are self-absorbed by a cold foreground layer. Lower limits to the brightness temperatures range from 11-33 K.

Rotational temperatures for the interstellar gas were derived from the spectra of eight YSOs and correlate well with the distribution of cold dust and the photodissociation region. However, for some sources, the `FITROT` model could not fit all orders of the spectrum with a single temperature. This could be due to a possible temperature gradient, which we can model as a *two-layered* gas (hot and colder) in front of the star. The results from `FITROT` are presented in Table 2.2, and the results from the least-squares analysis (*lls*) are given in Table 2.3. Figures 2.4 and 2.5 show the `FITROT` and the *lls* output for SR 24S and Figure 2.6 shows the least-squares analysis output for GY 33. The locations of these objects relative to cold dust emission are shown in Fig. 2.7. Table 2.4 indicates the summary of the rotational temperatures derived for the foreground gas from the two methods along with the effective temperature of the YSOs by Sullivan et al. (2019).

Table 2.4. Summary of the derived excitation Temperatures

Source	$T_{\texttt{eff}}$ (K) [a]	Order[b]	$T_{\texttt{FITROT}}$ (K)	$T_{\texttt{lls}}$ (K)
VSSG 1	4370 ± 300	220 & 221	22 ± 3	22^{+3}_{-2}
		222	168^{+85}_{-49}	236^{+37}_{-29}
GY 33	4220 ± 20	220 & 221	56 ± 12	43^{+16}_{-9}
		219 & 222	154^{+54}_{-29}	144^{+28}_{-21}
SR 24S	4900 ± 80	220, 221 & 222	69^{+8}_{-10}	113^{+13}_{-10}
WLY 2-54	—	220, 221 & 222	31^{+15}_{-7}	54^{+6}_{-4}
WLY 2-51	4660 ± 230	220 & 221	22^{+7}_{-5}	23 ± 3
WL 20E	4840 ± 60	220 & 221	19^{+10}_{-5}	20^{+3}_{-2}
WL 4	3260 ± 20	220 & 221	22^{+7}_{-5}	26^{+8}_{-5}
GY 235	3360 ± 20	220 & 221	24^{+9}_{-6}	24^{+5}_{-3}

Notes: $T_{\texttt{lls}}$ is the excitation temperature determined from the linear least square method, and $T_{\texttt{FITROT}}$ is the temperature determined using the `FITROT model`.
[a] Effective surface temperature of the sources are from Sullivan et al. (2019)
[b] Order 219: 2.36 - 2.37 μm; order 220: 2.35-2.36 μm; order 221: 2.34 - 2.35 μm; order 222: 2.32-2.34μm.

The temperatures derived from each source using the two methods generally agree within 3σ. The difference in temperature between the two methods is higher for orders corresponding to higher P and R lines (orders 219 and 222) because the detected lines in these orders are weaker. In all the sources, the total column density derived from the *(lls)* method is higher than that obtained from `FITROT`. Even though it is not clear as to why these differences arise, in all cases, the correlation coefficient from the *(lls)* method is higher than the correlation coefficient from `FITROT` model. It can be noted that both methods depend on the baseline of the data (i.e., how well the spectrum is normalized). The column densities inferred from the integrated intensities of the single-dish ^{13}CO observations are well-correlated with the values derived from both methods. The sole exception is the column density toward GY 33, which is the lowest in the single-dish observations and highest in the pencil beam. One explanation is that the dense molecular gas is very compact around GY 33, and the column density is diluted by the larger beam of the single-dish observations.

2.6.1. Notes on Individual Sources. Most sources were only detected in the low R- and P- branch (order 220 and order 221) lines, but VSSG 1, SR 24S, and GY 33 displayed higher R- and P- branch lines (order 219 and order 222) from warmer gas.

2.6.1.1. WLY 2-54. In terms of evolutionary state, this object is Stage I, as it has finished its main accretion phase, and most of the material has centralized (Sullivan et al., 2019). The spectrum of WLY 2-54 does not show any photospheric absorption lines, and it served as a reference against which we compared the interstellar absorption line features in the other sources. The *lls* method of determining temperature yields 54^{+6}_{-4} K, and is consistent with the temperature derived using the `FITROT` model, which is 31^{+15}_{-7} K. It should be noted, however, that the correlation coefficient for the *lls* fit is slightly higher (0.94) than that of the `FITROT` (0.89), thereby indicating that the temperature determined from the *lls* method is more accurate. This source's spectrum also shows Br γ emission at 2.166 μm indicative of accretion characteristic of Stage I evolution objects; infalling material from an accreting disk follows magnetic field lines and experiences thermal shocks as it hits the stellar photosphere. The shock releases energy that heats the surrounding material of the star and creates an emission spectrum. The spectrum of this source also shows molecular hydrogen emission at ~2.223 μm and ~2.122 μm, most likely from shocked local material due to outflows into the surrounding interstellar medium.

2.6.1.2. WLY 2-51. This source is in Stage I evolutionary state since it has almost finished accreting matter (Sullivan et al., 2019). The effective temperature of this source, as measured by Sullivan et al. (2019), is 4660 K ± 230 K. The temperature derived for the foreground gas at the location of this source using the *lls* method is 23 ± 3 K. This temperature is consistent with what is retrieved using the `FITROT` model, 22^{+7}_{-5} K. The fact that the interstellar lines were not identified in the higher transitions may indicate that *any higher temperature gas has a low column density*.

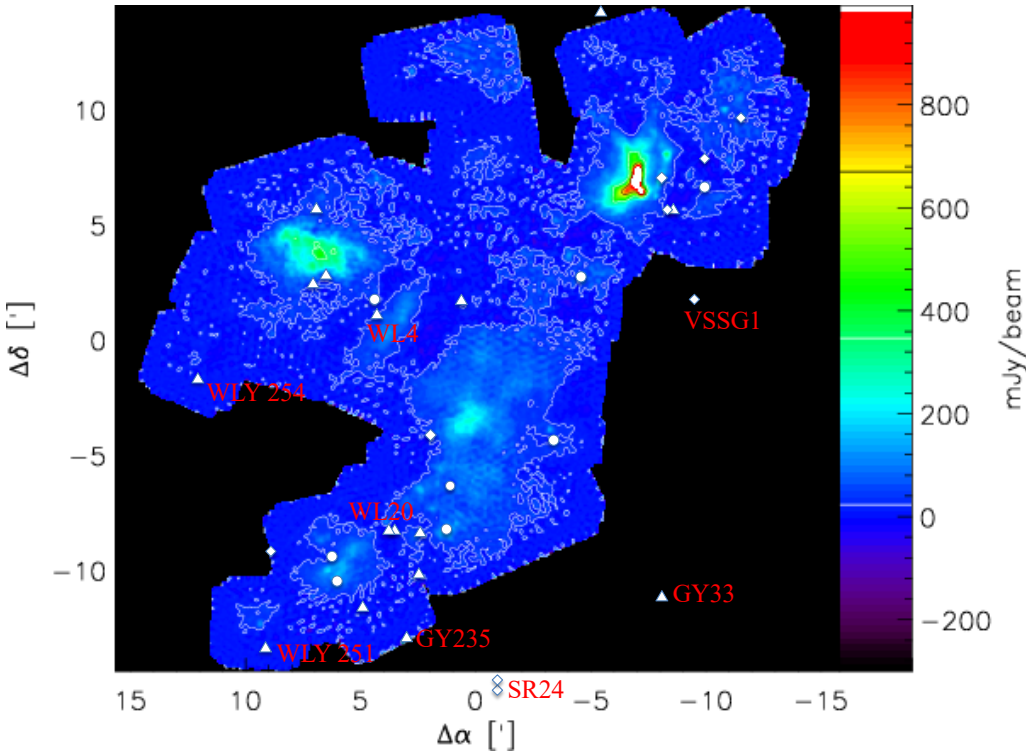

Figure 2.7. High column density cold dust map in the main cloud L1688 at λ = 1.3 mm. The map indicates locations of the sources in the main cloud L1688. The triangle and circle symbols represent Stage I objects, and the diamond symbols are for Stage II objects. The figure is adapted from Ossenkopf et al. (2008).

2.6.2. SR 24S. The SR 24S is in a binary system with a secondary companion SR 24N. The companion SR 24N is also a binary containing SR 24Na, and SR 24Nb (Mayama et al., 2010). It is in Stage II evolutionary state as the infalling envelope of material surrounding it is completely cleared. The temperature of this source, as determined by Sullivan et al. (2019), is 4900 K ± 80 K. The radial velocity derived for SR 24S from the iSHELL infrared data by Sullivan et al. (2019) significantly differs from the value derived from optical data in a different epoch by Rigliaco et al. (2016). Such a large variation in radial velocity value is too large to be due to interactions with SR 24N, but instead, the SR 24S itself could be binary as well (Sullivan et al., 2019).

For SR 24N, the interstellar lines detected in a few orders looked very noisy and blended with other photospheric absorption lines, and thus, we decided not to include them in our analyses. The temperature derived for SR 24S from the *lls* method is 113^{+13}_{-10} K is higher than that derived from the FITROT model, which is 69^{+8}_{-10} K. However, the correlation coefficient from the *lls* method (0.95) is significantly higher than that from the FITROT, which is 0.56. Thus, the temperature obtained from the FITROT is possibly underestimated. It is worth noting that the transitions P_4 and R_4 have the same energy, $\frac{E_{J''}}{k}$, and thus they are expected to have the same column density value, $\ln\left(\frac{N_{J''}}{2J''+1}\right)$. Thus, as seen from Table 2.3, the two transitions have a similar column density within their respective measurement uncertainties. There is Brγ emission in the spectrum of this source, indicating accretion. A molecular hydrogen emission at ~ 2.122 μm indicates shocks and winds as a heating mechanism for the local material.

2.6.2.1. VSSG 1. This source is in a Stage II evolutionary state and is west of the high dust column density region (Fig 2.7). The temperature estimate of this source, as measured by Sullivan et al. (2019), is 4370 K ± 300 K. The plot of $\ln\left(\frac{N_{J''}}{2J''+1}\right)$ vs $\frac{E_{J''}}{k}$ for low-J transition, interstellar absorption lines at the location of this source have a relatively steeper (higher) slope, giving a colder temperature. However, the plot has a lower slope for higher-J transition absorption lines (order 222), giving hotter temperatures. This indicates that there is a two-layered gas (hot and cold) in front of the YSO or a temperature gradient, and as such, the measurements from all orders for this source cannot be fitted with a single temperature value. The temperature derived using the *lls* method from the low-J transition absorption lines is 22 ± 2 K, which agrees very well with the temperature obtained using the FITROT model 22^{+3}_{-2} K. The temperature derived from higher-J transition absorption lines using the *lls* method is 236^{+37}_{-29} K. This temperature overlaps with the upper limit of the temperature 168^{+85}_{-49} K derived from the FITROT model. However, the correlation coefficient of the *lls* (0.96) is much higher than that of the FITROT (0.45), thereby making the temperature derived from the former more reliable.

It is worth noting that the hot gas column densities are higher than that of the cold gas. A Br γ emission is identified in the spectrum of this source, indicating accretion, and there is no indication of wind as a heating source for the surrounding material.

2.6.2.2. GY 235. In terms of the evolutionary state, this is the Stage I object. This source is relatively cool, with an effective temperature estimate of 3360 ± 20, as determined by Sullivan et al. (2019). The temperature derived from these low-J transition absorption lines for the surrounding cloud using the *lls* method 24^{+5}_{-3} K is consistent with the temperature obtained from the `FITROT` model, which is 24^{+9}_{-6} K. The spectrum of this source shows Br γ emission, indicating accretion, and molecular hydrogen emission at 2.122 μm, indicating shock as a heating mechanism.

2.6.2.3. WL 4. This source is a Stage I object in terms of evolutionary state. Like the GY 235, this source is also known to be a cool star with a temperature estimate of the source itself is 3260 K ± 20 K (Sullivan et al., 2019). The temperature derived from the lower-J transition absorption lines using the *lls* method is 26^{+8}_{-5} K, while the temperature derived using the `FITROT`, which is 22^{+7}_{-5} K. These temperatures overlap their respective measurement uncertainties.

2.6.2.4. GY 33. This is a Stage I source in terms of evolutionary state. Like VSSG 1, this source is also located west of the high column density cold dust (Fig. 2.7), and its temperature estimate, as determined by Sullivan et al. (2019), is 4220 K ± 20 K. The data from the low-J transition absorption lines tend to have a steep slope (lower temperature) in the *lls* method. In contrast, the high-J transition absorption lines give a flatter slope predicting higher temperatures (Fig 2.6). The temperature derived from the lower-J transition absorption lines using the *lls* method is 43^{+16}_{-9} K, which overlaps with the temperature derived from `FITROT`, which is 56 ± 12 within their respective measurement uncertainties. However, the correlation coefficient from *lls* (0.85) is higher than that of `FITROT` (0.57), making the temperature derived from the *lls* more reliable.

The temperature derived from the higher-J transition absorption lines using the *lls* method is 144^{+28}_{-21} K, while the temperature derived from FITROT model is 154^{+54}_{-29} K. These temperatures overlap within their measurement uncertainties. The correlation coefficient from the *lls* (0.89) is comparable with that from the FITROT model, which is 0.80. As with the VSSG 1 source, the column density is higher for hotter gas than the colder.

2.6.2.5. WL 20E. This is a Stage I source in terms of evolutionary state. The temperature estimate of this source, as measured by Sullivan et al. (2019), is 4840 ± 60 K. WL 20E is in a wide binary system with a companion WL 20W (Ressler and Barsony, 2001). However, like SR 24N, the interstellar lines detected in a few orders for WL 20W were noisy and looked blended with photospheric lines, and thus, we did not include them in our analyses. The temperature derived for WL 20E from the low-J transition absorption lines using the *lls* method is 20^{+3}_{-2} K agrees with the temperature derived from the FITROT model, which is 19^{+10}_{-5} K. Again, as was the case for the WL 4 source, absorptions from the higher P and R branch transitions were undetected.

2.6.3. Sources of Measurement Uncertainties of Temperature. As mentioned earlier, both methods of determining rotational temperature depend on the normalization of the spectrum, and errors in the normalization introduce systematic errors. Another thing we noticed upon comparing the total column density of the lines determined from the two methods is that the total column density determined by the *lls* method is higher than that determined using the FITROT model. Even though it is not evident as to what is the cause of this discrepancy, in all cases, the correlation coefficient from the *lls* method is significantly higher than that obtained from FITROT model. Thus, the FITROT model might have underestimated the column density values for each transition. Another thing we noticed in the measurement of column density from the *lls* method is that the column density values of P_1 and R_1 transitions are different. Ideally, since both have the same lower energy, they are expected to have the same column density value. The oscillator strength value for P_1 is about twice that of the R_1.

Since, according to Eq.2.1, the oscillator strength is inversely related to the column density, the equivalent width of R_1 has to be about twice that of P_1 for them to have a comparable column density. However, that is not the case. One possible reason we see such a big difference in the column density value between the two transitions is that the gas is generally assumed to be in *local thermodynamic equilibrium*, which may not be the case.

2.7. DISCUSSION AND SUMMARY

The temperatures and column densities derived for the 8 YSOs can be put into context with the larger-scale structure of the molecular gas and dust. The location of the YSOs relative to the warm dust (traced by mid-infrared emission) and cold dust (traced by 1.3 mm continuum emission) are shown in Figs. 1.1 and 2.5, respectively. It is important to note that apart from SR 24S, there is little information with a resolution comparable to our observations (i.e., with a slit width of 0.75″).

2.7.1. Comparisons With Large Scale Structure. The COMPLETE (Coordinated Molecular Probe Line Extinction and Thermal Emission) survey mapped ^{12}CO (J = 1-0) and ^{13}CO(J = 1-0) emission lines over the L1688 cloud with 40 ″ resolution (Ridge et al., 2006). With the possible exception of GY 235, all the ^{12}CO lines of sight are optically thick and self-absorbed. Lower limits to the ^{12}CO brightness temperatures (11-33 K) generally agree with those derived from the low R- and P-branch lines presented in Tables 2.2 and 2.3, with some exceptions. The CO column densities, proportional to the ^{13}CO integrated intensities from the large beam observations, correlate well with that derived for the colder gas in Tables 2.2 and 2.3. The exception is GY 33, for which we derive the highest column density of any source (in both the hot and cold components). This requires the cold CO gas we are sampling to be very compact with a low filling factor in the larger beam. We note that the layers of high-temperature gas toward VSSG 1 and GY 33 (∼140-240 K) would not contribute significantly to CO emission lines in the (J = 1-0) transition.

Relative to the warm dust emission in Fig. 1.1, both VSSG 1 and GY 33 lie in lower column density western region dominated by Polycyclic Aromatic Hydrocarbon (PAH) emission heated by HD147889 as represented by IRAC band 4 (green), and this could account for the warm dust layer we observe. The remainder of the sources lie in the colder part of the cloud, shielded from external heating. WL 4 is part of a small cluster that appears to have created a small bubble of warmer dust, but we do not see any effect on the gas temperature along our line of sight. All but three sources lie in the region of high column density cold dust (Fig. 2.5), but there does not seem to be any correlation between the cold dust column density observed with 12″ resolution (Motte et al., 1998) and the gas column density measured in the 0.75 ″ beam. The strongest emission sources at λ = 1.3 mm are SR 24S (280 mJy), WLY 2-51 (110 mJy), and WL 20E (95 mJy), while our highest gas column density sources are weak or undetected (Andre and Montmerle, 1994; Motte et al., 1998). The high-temperature gas that dominates the 0.75 ″ beam toward SR 24S (∼110 K) is not evident in the 40 ″ beam and may be compact and have a low filling factor. Indeed, ALMA interferometric observations of SR 24S resolve a circumstellar dust disk with a ∼ 0.5″ cavity occupied with small dust grains and the peak of the CO (J = 2-1) molecular emission (Pinilla et al., 2017). The heating source could be gas shock-excited by the stellar wind, accretion, or the YSO itself, which, with a K1 spectral type, is the earliest type star in this sample.

In summary, the ^{12}CO temperatures and column densities derived for each YSO from the *lls* and `FITROT` agree well within their respective uncertainties, with the former having a higher degree of confidence. Four sources (GY 235, WL 20E, WL 4, and WLY 2- 51) have absorption lines only from the lower R and P branch lines and fit well with a single temperature ranging from 20-26 K. In contrast, the remaining sources (VSSG 1, GY 33, SR 24S, and WLY 2-54) show evidence of a gradient in temperature with the cooler temperatures derived from the lowest R and P branch lines. We constructed ^{12}CO line profiles from the COMPLETE survey in a 40″ beam (Ridge et al., 2006) along the lines of sight that include each YSO.

Except for GY 235, ^{12}CO line profiles from the larger beam COMPLETE survey show evidence for self-absorption from foreground gas, suggesting that a range of temperatures along the line of sight may be present. Without more detailed modeling, only a lower limit to the true column density (column of gas along the line of sight to the surface of the YSO) from the lower R and P branch lines can be derived. For comparison with other studies, the ^{12}CO column densities can be converted to hydrogen column densities assuming an abundance ratio [CO]/[H_2] = 1.1×10^{-4} (Pineda et al., 2010). The relationship between hydrogen column density and dust column density has been derived from X-ray observations of Class III YSOs in L1688. It is given by $N_{H,x}/A_J = 5.6 \times 10^{22}$ cm^{-2} mag^{-1} for A_v <45 mag (Vuong et al., 2003). Assuming a standard extinction law, the visual extinctions derived from the *lls* method of 13, 13, and 17 mag for GY 235, WL 20E, and WL 4 agree reasonably well with values derived from infrared colors and template matching with dwarf standards of 9, 16, and 20 mag, respectively, given their uncertainties (Bontemps et al., 2001; Manara et al., 2015; McClure et al., 2010; Natta et al., 2006). The agreement is poor for WLY 2-51, with our extinction estimate about a factor of 3 smaller than that estimated from infrared colors and template matching. This can be attributed to the assumption by the latter of no excess emission in the J band, which is a poor assumption for a YSO with a flat-spectrum SED and would lead to an overestimation of A_v.

2.7.2. VSSG 1 and the Photo-Dissociation Region. VSSG 1 lies within the ρ Oph-W PDR excited by the B2V star HD147889. The PDR is traced by H_2 emission (Habart et al., 2003), which also correlates with extended 2MASS Ks-band emission, PAH emission in the ISO LW2 band and IRAC band 4, and centimeter-wave continuum emission [see Fig. 3 in Casassus et al. (2018); Arce-Tord et al. (2020)]. The H_2 emission is excited by ultraviolet fluorescence and is a cooling line for the PDR from which Habart et al. (2003) derived temperatures of 300-345 K.

While the H_2 map does not show the full extent of the PDR, the PAH emission and centimeter-wave emission indicate it extends further south to include VSSG 1 (e.g., Fig. 2.1). The ~240 K we derive for VSSG 1 is consistent with this association.

2.7.3. Winds and Accretion. Ignoring the hot gas layer observed toward two sources, the warmest CO gas (54 - 110 K) observed in the 0.″75 beam is toward SR 24S and WLY2-54. Both of these YSOs show evidence of emission lines from ionized hydrogen and shocked molecular hydrogen. This suggests accretion and/or stellar winds could be responsible for heating the CO gas along these lines of sight. Conversely, GY 235 and VSSG 1 also show evidence for winds and/or accretion that has had little or no effect on the gas temperatures we derive. The effective temperatures of the YSOs seem to have little effect on the gas temperatures apart from SR 24S.

PAPER

I. COMA ABUNDANCES OF VOLATILES AT SMALL HELIOCENTRIC DISTANCES: COMPOSITIONAL MEASUREMENTS OF LONG-PERIOD COMET C/2020 S3 (ERASMUS)

Chemeda Ejeta[(1)], Erika Gibb[(1)], Nathan Roth[(2,3)], Michael A. DiSanti [(2)], Neil Dello Russo [(4)], Mohammad Saki [(1,5)], Adam J. McKay [(6)], Hideyo Kawakita [(7)], Younas Khan [(8)], Bonch P. Bonev [(9)], Ronald J. Vervack Jr. [(4)], Michael R. Combi [(10)]

[(1)] Department of Physics and Astronomy, University of Missouri-St. Louis, Saint Louis, MO 63121, USA

[(2)] Solar System Exploration Division, Planetary Systems Laboratory, MS 693, NASA Goddard Space Flight Center, Greenbelt, MD 20771, USA

[(3)] Catholic University of America, Washington, DC

[(4)]Johns Hopkins University Applied Physics Laboratory, Laurel, MD 20723, USA

[(5)] Auburn University, Auburn, AL

[(6)] Department of Physics and Astronomy, Appalachian State University, Boone, NC 28608-2106

[(7)] National Astronomical Observatory of Japan, 2-21-1 Osawa, Mitaka, Tokyo 181-8588, Japan

[(8)] University of Alabama at Birmingham, Birmingham, AL, USA

[(9)] Department of Physics, American University, Washington, DC 20016, USA

[(10)] Department of Climate and Space Sciences and Engineering, University of Michigan, Ann Arbor, MI 48109, USA

Email: ctejeta@gmail.com

ABSTRACT

We report production rates of H_2O and nine trace molecules (C_2H_6, CH_4, H_2CO, CH_3OH, HCN, NH_3, C_2H_2, OCS, and CO) in long-period comet C/2020 S3 (Erasmus) using the high-resolution, cross-dispersed infrared spectrograph (iSHELL) at NASA-IRTF, on two pre-perihelion dates at heliocentric distances R_h = 0.49 and 0.52 AU. Our molecular abundances with respect to simultaneously or contemporaneously measured H_2O indicate that S3 is depleted in CH_3OH compared to its mean abundance relative to H_2O among the overall comet population (OCCs and JFCs combined), whereas the eight other measured species have near-average abundances relative to H_2O. In addition, compared to comets observed at $R_h < 0.80$ AU at near-infrared wavelengths, S3 showed enhancement in the abundances of volatile species H_2CO, NH_3, and C_2H_2 indicating possible additional (distributed) sources in the coma for these volatile species. The spatial profiles of volatile species in S3 in different instrumental settings are dramatically different, which might suggest temporal variability in comet outgassing behavior between the non-simultaneous measurements. The spatial distributions of simultaneously measured volatile species C_2H_6 and CH_4 are nearly symmetric and closely track each other, while those of CO and HCN co-measured with H_2O (using different instrument settings) are similar to each other and are asymmetric in the anti-sunward direction.

Keywords: comets, Near Infrared, comae

1. INTRODUCTION

Comets are among the small bodies stored in the outer reaches of our solar system. Having experienced minimal alteration from gravitational self-heating, thermal processing, or radiative processing (e.g., DiSanti et al., 2017), their internal compositions are likely to have changed minimally since the formation of the solar system ($\sim$ 4.5 Gyr ago).

Thus, comets likely retain a compositional record of the protoplanetary disk midplane during planet formation (Bockelée-Morvan et al., 2004; DiSanti et al., 2017; Mumma and Charnley, 2011). Comet C/2020 S3 (Erasmus; hereafter, S3) was discovered by Nicolas Erasmus of the Asteroid Terrestrial-Impact Last Alert System (ATLAS) on UT 2020 September 17. S3 reached perihelion ($R_h \sim 0.4$ AU) on UT 2020 December 12 and was closest to Earth (1.03 AU) on 2020 November 19. The reciprocal semi-major axis after integrating the orbit backward to a time before any planetary perturbations, $1/a_0$, is approximately inversely related to the square of the number of inner Solar System crossings (A'Hearn et al., 1995). Królikowska and Dybczyński (2017) analyzed the dynamical simulation of long-period comets having perihelia farther than 3.1 AU from the Sun. They showed that all dynamically old comets have $1/a_0 > 25 \times 10^{-6}$ AU^{-1} ($a_0 < 40,000$ AU). Thus, with $1/a_0$ of ~ 5 x 10^{-3} AU^{-1} (Nakano Note 4506), S3 is a dynamically old comet that has previously visited the inner solar system.

Comets such as S3 are from the Oort cloud and therefore have long orbital periods (Vokrouhlický et al., 2019). As comets approach the inner solar system, increasing insolation causes nucleus ices to sublimate. The released volatiles and refractory material (dust dragged by sublimating gases) lead to an expanding atmosphere (i.e., coma). High-resolution, near-infrared (NIR) spectroscopy is a valuable tool to characterize the composition of volatiles (ices) in comet nuclei through the analysis of fluorescent emissions from H_2O, CO, CH_4, C_2H_6, HCN, NH_3, C_2 H_2, H_2CO, OCS, and CH_3OH in the coma. The nucleus composition inferred from these studies can also place observational constraints on the nascent protoplanetary disk midplane where comets formed (Eistrup et al., 2019; Willacy et al., 2022).

Although our understanding of comet composition has evolved in recent years, the sample size of ~30 OCCs (dominated by observations at $R_h > 0.8$ AU) is insufficient to fully represent their compositional diversity, making their classification difficult (Crovisier et al., 2004; Dello Russo et al., 2016a).

Due to solar avoidance constraints for daytime observations, OCCs measured at $R_h \leq 0.80$ AU are particularly limited in number. Thus, our observations of S3 at $R_h \sim 0.50$ AU are crucial to not only further the development of a taxonomy for comets based on primary volatile composition but also to investigate possible effects of heliocentric distance on composition measurements.

We present production rates and abundance (i.e., mixing ratios) with respect to H_2O and C_2H_6, measuring eleven molecules having fluorescent emissions between $\sim$ 2.8 and 5.0 μm: H_2O, C_2 H_6, H_2CO, CH_3OH, CH_4, CO, NH_3, HCN, C_2H_2, NH_2, and OCS. In Section 2, we discuss our observations. In Section 3, we discuss our data reduction and analysis. In Section 4, we present our results. Section 5 discusses our results and places them in the context of comets characterized to date.

Table 1. The iSHELL observing Log for S3

Setting[a]	Target	UT time	T_{int} (minutes)	Slit PA (°)
	2020 Nov 29, R_h=0.52 AU, Δ = 1.10 AU, dΔ/dt = 18.65 km s^{-1}			
L-custom	S3	19:32-20:10	40	273
Lp1	S3	20:26-21:05	30	273
	BS 5531	-	-	-
	2020 Dec 01, R_h=0.49 AU, Δ = 1.12 AU, dΔ/dt = 21.67 km s^{-1}			
M2	S3	18:11-18:45	40	272
L-custom	S3	19:04-20:20	55	272
	BS 5531	20:52-20:58	-	-
M2	BS 5531	21:18-21:24	-	-
Lp1	BS 5531	21:31-21:37	-	-
	S3	21:40-22:10	40	272

Notes: R_h, Δ, and dΔ/dt are the heliocentric distance, geocentric distance, and geocentric velocity of S3 at the time of observation, respectively, and Tint is the total on-source integration time. The slit position angle (PA) was oriented along the projected Sun-comet line on both dates.
[a] Spectral setting used to sample molecular lines.

2. OBSERVATIONS

We observed S3 during the daytime on UT 2020, November 29, and UT December 1 with Director's Discretionary Time, using the high-resolution NIR echelle spectrograph iSHELL (Rayner et al., 2022) at the 3-m NASA Infrared Telescope Facility (IRTF) located at Maunakea, HI. iSHELL is a cross-dispersed infrared spectrometer operating at ~ 1-5 μm wavelengths. For the comet observations, we used the 0.″75 (6 pixels) wide and 15″ long slit. On both dates, we utilized the Lp1 setting, which covers ~3.28–3.66 μm, to sample C_2H_6, CH_4, H_2CO, CH_3OH, and NH_2 [plus prompt OH, used as a proxy for the production and spatial distribution of its parent, H_2O; Bonev (2005), Bonev and Mumma (2006)], and a custom L-band setting covering ~ 2.80–3.10 μm and sampling HCN, C_2H_2, NH_3, NH_2 together with H_2O. On December 1, we also used the M2 setting, which covers ~ 4.52–5.25 μm, to sample CO, OCS, and CN together with H_2O. CO and CH_4 have strong corresponding terrestrial absorptions; therefore, sufficient geocentric Doppler velocity ($|d\Delta/dt|$ ~ ≥ 12 km s^{-1}) is required to shift the cometary emission lines away from the (opaque) cores into the wings of their telluric counterparts (Dello Russo et al., 2016a). The magnitude of the geocentric Doppler shift of S3 on the dates of our observations (~ +18 – 21 km s^{-1}; see Table 1) was sufficient to measure both CO and CH_4.

Spectra were obtained using a standard ABBA nod pattern to facilitate sky subtraction, with A and B beams in the (15″ long) slit symmetrically displaced about its center and separated by half its length. Combining spectra as A-B-B+A canceled emissions from the thermal background, instrumental biases, and sky emission (lines and continuum) to second order in air mass. The slit was oriented along the projected Sun-comet direction with a position angle (PA) of ~ 270° on both dates to compare the release of material into sunward versus anti-sunward-facing hemispheres of the comet with a solar phase angle of ~60°. To calibrate fluxes, spectra of the bright infrared flux standard star BS 5531 were obtained, using a 4″ wide slit to minimize slit losses. Our observing log is shown in Table 1.

On UT 2020 November 29, the standard star spectra acquired using the L-custom setting were not usable for flux calibration due to bad weather conditions. As a result, for this date, we computed flux calibration factors (Γ, W/m^2/cm^{-1}/counts/s) from the ratios of their values measured using the Lp1 setting on both nights and the L-custom setting on UT 2020 December 1 (for which photometric conditions persisted throughout the observing period). The atmospheric seeing was also relatively poor ($\sim$ 1.5″) on November 29 compared to December 1 ($\sim$ 0.5 - 1.0″).

3. DATA REDUCTION AND ANALYSES

We followed data reduction procedures that have been rigorously tested and are described extensively in refereed literature(Bonev, 2005; Dello Russo et al., 1998; DiSanti et al., 2006, 2014; Radeva et al., 2010), including their application to unique aspects of iSHELL spectra (DiSanti et al., 2017). Echelle orders were straightened spatially and spectrally so that each row corresponded to a unique position along the slit and each column to a unique wavelength. Spectra were extracted from the processed orders by summing over 15 rows (approximately 2.5″), seven rows to each side of the nucleus, defined as the peak of continuum emission in each spectral order. Individual A-B pairs were spatially registered to correct for potential comet drift during an exposure sequence; however, we note that these corrections were minimal, owing to active IR guiding via narrowband filter imaging near 3.46 μm.

We determined contributions from continuum and gaseous emissions as previously described (e.g., DiSanti et al., 2017) and as illustrated in Fig.1. Column burdens of telluric absorbers were retrieved and quantified using the NASA Planetary Spectrum Generator (Villanueva et al., 2018). The fully resolved transmittance function was convolved to the resolving power of the data ($\sim 4.2 \times 10^4$) and scaled to the comet continuum level. Next, to isolate cometary emission lines, we subtracted the modeled continuum.

After correcting each modeled g-factor (line intensity) for the monochromatic atmospheric transmittance at its Doppler-shifted wavelength (based on the geocentric velocity of the comet at the time of observation), synthetic models of fluorescent emission for each targeted species were compared to observed line intensities. The g-factors used in this study were generated with quantum mechanical models developed for H_2O (Villanueva et al., 2012b), OH^* (Bonev and Mumma, 2006), HCN and NH_3 (Villanueva et al., 2013), NH_2 (Kawakita and Mumma, 2011), C_2H_2 [(Villanueva et al., 2011b), see appendix C], C_2H_6 (Villanueva et al., 2011b), CH_3OH (DiSanti et al., 2013; Villanueva et al., 2012a), H_2CO (DiSanti et al., 2006), CH_4 (Gibb et al., 2003), and CO (DiSanti et al., 2001).

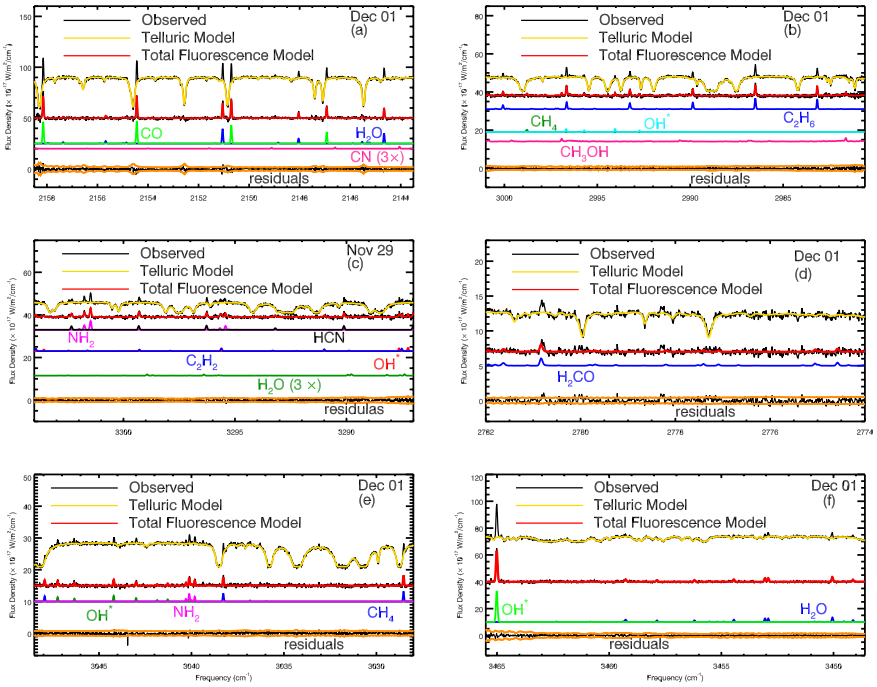

Figure 1. Sample spectra and best-fit fluorescent models of molecular emissions in comet C/2020 S3 (Erasmus) during the observations on 2020 December 01 and November 29. The observed spectra (black) are superimposed with the telluric model (yellow). The red is the total fluorescence model overplotted on the telluric subtracted spectra. Individual fluorescence emission models (color-coded by species) are shown below the observed spectrum in each panel. The bottom trace indicates the residual spectrum (after subtracting modeled continuum and total molecular contributions), with the superimposed $\pm 1\sigma$ stochastic noise envelope shown in orange.

4. RESULTS

We determined rotational temperatures (T_{rot}), volatile production rates (Q, molecules s^{-1}), and abundances (or "mixing" ratios), e.g., Q_X/Q_{H_2O} or $Q_X/Q_{C_2H_6}$, and spatial profiles for volatile species in S3. The details of this analysis are discussed below.

4.1. DETERMINATION OF ROTATIONAL TEMPERATURE

The relative strengths of molecular emission lines are constrained by the excitation conditions in the coma (e.g., Bockelée-Morvan et al., 2004; DiSanti et al., 2016). The strengths of these lines are quantified by a rotational temperature (T_{rot}), which needs to be known (either measured or assumed) to determine accurate molecular production rates for each species. When strong lines of a given molecule spanning a broad range of excitation energies can be measured, Trot is obtained using zero-slope excitation analysis (e.g., Bonev, 2005; Dello Russo et al., 2004; DiSanti et al., 2006). This technique retrieves the rotational temperature corresponding to a zero slope in F_{line}/g vs. E_{up} (or E_{low}), where F_{line} is the observed line flux, g is the temperature-dependent fluorescent g-factor, and E_{up} is the upper (lower) state rotational energy of each measured transition (emission line). In S3, H_2O, C_2H_6, HCN, CH_3OH, CO, and H_2CO provided a sufficient number of lines having high S/N and spanning a wide range of rotational energy to obtain a well-constrained T_{rot}. As indicated in Table 2, the rotational temperatures determined from these species on both dates are consistent within their 1-σ uncertainties. For CH_4, C_2H_2, NH_3, and OCS, accurate rotational temperatures could not be determined, so we assumed the value for H_2O from the same date. This assumption is reasonable, given the consistency among rotational temperatures determined from different species (see Table 2; assumed T_{rot} values are given in parentheses).

4.2. MOLECULAR PRODUCTION RATES

Nucleus-centered molecular production rates, Q_{nc}, are obtained from the line fluxes measured from an extract of 15 spatial rows (as defined in section 3). In our analysis, emission lines are selected if they are not strongly blended with other species and are in regions of adequate atmospheric transmittance. For a given emission line, Q_{nc} is obtained by applying a coma model that assumes a spherically symmetric gas outflow with uniform velocity and direct nucleus release (e.g., DiSanti et al., 2016, 2014):

$$Q_{nc} = \frac{4\pi\Delta^2 F_{line}}{f(x)\tau_1 g_1}, \tag{1}$$

where τ_1(s) is the molecular photo-dissociation lifetime at R_h =1 AU, g_1(W molecule^{-1}) is the fluorescence g-factor at R_h = 1 AU, Δ (m) is the geocentric distance, and F_{line} (W m^{-2}) is the line flux at the top of the terrestrial atmosphere. The photodissociation timescales of each molecular species and the fluorescence g-factors (given at R_h = 1 AU) are scaled to the heliocentric distance of our observations using the heliocentric dependence of each quantity (i.e., $\tau = \tau_1 R_h^2$, $g = g_1 R_h^{-2}$, where the subscript "1" refers to values at R_h = 1 AU). The quantity f(x) is the fraction of the total number of molecules in the coma encompassed by the beam, assuming their release is entirely from the nucleus, and includes the R_h dependent molecular scale length, l, given as $l = V_{gas}(R_h{=}1\mathrm{AU})\tau_1 R_h^{1.5}$ (e.g. DiSanti et al., 2016). The molecular lifetimes used in our analyses are determined using the molecular photodissociation rates in the solar radiation field at R_h = 1 AU as provided by Huebner and Mukherjee (2015). The gas outflow velocity from the nucleus, $v_{gas} = 800 \times R_h^{-0.5}$m s^{-1}, is assumed based on velocity-resolved observations of bright comets at radio wavelengths (e.g., Biver et al., 2006). This quantity is not measured directly from our observations since the spectral resolving power ($\sim 4.2 \times 10^4$) corresponds to a velocity resolution of ~7 km s^{-1} and is thus insufficient to resolve spectral lines and hence gas outflow velocities.

This assumption of the canonical value of v_{gas} introduces a systematic uncertainty in the production rates; however, this has a negligible effect on our derived abundance ratios (Dello Russo et al., 2020).

Compared to the coma model, slit losses due to atmospheric seeing lower the fraction of molecules within nucleus-centered extracts. As a result, production rates derived from nucleus-centered extracts are underestimated. A multiplicative correction factor known as the growth factor (GF) is applied to the Q_{nc} (e.g., Dello Russo et al., 1998, 2020; DiSanti et al., 2001) to compensate for these effects. Thus, the total production rate, Q_{tot}, is given by $Q_{tot} = (Q_{nc})GF$. The GF is determined through the Q-curve method for analyzing the spatial profiles of emissions (Bonev, 2005; Dello Russo et al., 1998, 2020) by averaging signal (summed over multiple lines) from equidistant, diametrically opposite directions along the profile relative to the position of peak emission intensity (DiSanti et al., 2016). We could not calculate a well-constrained GF for some molecules owing to insufficient signal-to-noise ratios in the wings of the profiles (i.e., along lines-of-sight increasingly displaced from the position of peak emission intensity). For these molecules (e.g., CH_3OH, H_2CO, NH_3, and C_2H_2), we assumed the GF of either simultaneously measured C_2H_6 (for those obtained within the Lp1 setting) or H_2O (for those obtained with the L-custom setting). For CH_3OH and H_2CO, the assumption of a GF from C_2H_6 is reasonable, given that their spatial profiles, while noisy, are consistent with nucleus-centered sublimation (Fig. 2). In addition, seeing-related flux losses are a common systematic effect for all molecular species sampled within a given spectrograph setting. Therefore, they will influence the GF (within a setting) in an identical manner (e.g., Bonev et al., 2021; DiSanti et al., 2014; Villanueva et al., 2012a). Production rates for all the species and their mixing ratios relative to water (and ethane) are presented in Table 2.

4.3. MOLECULAR MIXING RATIOS

The compositional taxonomy of comets is based on the measurements of mixing (or abundance) ratios for molecules (DiSanti et al., 2021), usually calculated with respect to H_2O (the most abundant molecule in active comets) and are expressed as the ratio of the total production rate of a given molecule to that of H_2O (Q_X/Q_{H_2O}). H_2O is usually observed simultaneously (within the same instrument setting) or contemporaneously (during the same observing block) as the other molecules. The uncertainty in the mixing ratio is calculated considering the uncertainty due to the GF and the stochastic noise or standard error (depending on which one is higher). The uncertainty due to the conversion factor between measured counts (ADU sec^{-1}) and flux density ($Wm^{-2}cm^{-1}$), Γ, is also included if the species being considered were observed using a different instrument setting. Since ethane (C_2H_6) is routinely measured in the comae of comets at high SNR, it has recently been used as an alternative compositional baseline molecule for calculating mixing ratios to extend the chemical taxonomy of parent volatiles in comets (e.g., Bonev et al., 2021, & references therein). In the case of S3, C_2H_6 was observed on both dates using the Lp1 setting. The mixing ratios (with respect to H_2O and C_2H_6) of the molecules we targeted during our two nights of observations are given in Table 2.

4.4. SPATIAL PROFILES

Studies of coma molecular emission intensity along the slit (spatial profiles) can provide information on the association of volatiles in the comet nucleus and how they are released into the coma (Dello Russo et al., 2004, 2020). Comparing profiles of co-measured volatiles and dust provides information regarding the release and outflow of material in the coma (e.g., Dello Russo et al., 2004). Such comparisons can also disentangle direct release from the nucleus versus potential distributed sources in the coma (Brooke et al., 2003; Dello Russo et al., 1998, 2016a; DiSanti et al., 2001).

We extracted emission profiles for H_2O, OH^* (OH prompt emission, a proxy for H_2O production rate and spatial profile), CH_4, NH_2, HCN, CH_3OH, H_2CO, and C_2H_6 in S3 on both dates. We also generated spatial profiles for H_2O, CO, and CN from the M2 setting on UT 2020 December 1 (see Figs. 2 and 3).

An important caveat in the interpretation of spatial profiles is that the iSHELL slit is 15″ long. When nodding on-chip, the A- and B-beams are separated by 7.5″ (half the slit length, see Section 2). Therefore, if the comet's emission extends beyond about 3.75″ from the nucleus, taking an A-B will result in the subtraction of some flux in the extended wings of the profiles. The broader the emission spatial profile, the more significant this self-subtraction will be. Also, some flux may be lost outside the slit for molecules that exhibit a substantial offset relative to the dust continuum since the telescope was tracking on the optocenter during our observations. In the discussion below, most molecules have sufficiently narrow profiles (FWHM < 3″) and small (< 0.5″) offsets to not be significantly affected by self-subtraction. The exceptions are species such as CN in the M2 setting and H_2O and OH^* in the L-custom setting (those with high offset toward anti-sunward direction and showing highly extended profiles). The variation in OH^*, NH_2, and H_2O profiles among the different dates and settings imply that S3 was exhibiting complex and variable outgassing behavior on relatively short timescales. For this reason, we limit the discussion of the spatial profiles to simultaneously observed molecules for each setting separately.

4.4.1. Lp1. Using the Lp1 setting, we obtained the spatial profiles of C_2H_6, CH_4, CH_3OH, H_2CO, NH_2, and OH^* on both dates (Fig. 2). The spatial profiles of the apolar molecules C_2H_6 and CH_4 (Figs. 2a and 2b) exhibit similar profile shapes and peak positions. While the profile shapes are also very similar to the co-measured, nearly Gaussian-shaped dust profile, there was a slight shift of the gas profiles toward the anti-sunward direction on November 29 that was not present on December 1.

Symmetric spatial distributions and a similar profile shape to the co-observed dust for these apolar species were noted by Villanueva et al. (2011a) in comet C/2007 W1 (Boattini), by DiSanti et al. (2021, 2014) in comets C/2018 Y1 (Iwamoto) and C/2009 P1 (Garradd) as well as by Bonev et al. (2017) in comet C/2006 W3 (Christensen) suggesting that these apolar hydrocarbons may have been released primarily from the nucleus.

The spatial profiles of the polar species CH_3OH and H_2CO [Fig. 2 (e) and (f)], as well as the product species of polar molecules, OH^* and NH_2 (Fig. 2 c and d), are consistent with each other on both dates. They are slightly narrower than the profiles of the apolar molecules and shifted more toward the anti-sunward direction with respect to the co-observed dust profile, with a slightly higher shift on November 29. As discussed in the next section, NH_2 could be produced by fluorescence and prompt emissions, though as we noted in section 4.4.2, most of the lines used in the spatial analysis of NH_2 are of lower rotational states for which prompt emission is expected to be insignificant.

4.4.2. L-custom. HCN, OH, and NH_2 were co-measured with H_2O on both dates using the L-custom setting. They all exhibited asymmetry in the anti-sunward direction as well as comparable and significant anti-sunward offsets relative to the dust [see Fig. 3 (a)-(d)]. On December 1, the spatial profiles for all species were broader than on November 29, similar to the pattern seen in the Lp1 spatial profiles [Figs. 2 and 3 (c) and (d)]. We note that OH^* (prompt emission), which tracks the distribution of H_2O, occurs generally at wavenumbers less than ~ 3410 cm^{-1} (corresponding to higher rotational quantum numbers). Combined OH (fluorescent emission) and OH^* (prompt emission) are expected for lines at larger wavenumbers (lower rotational excitation).

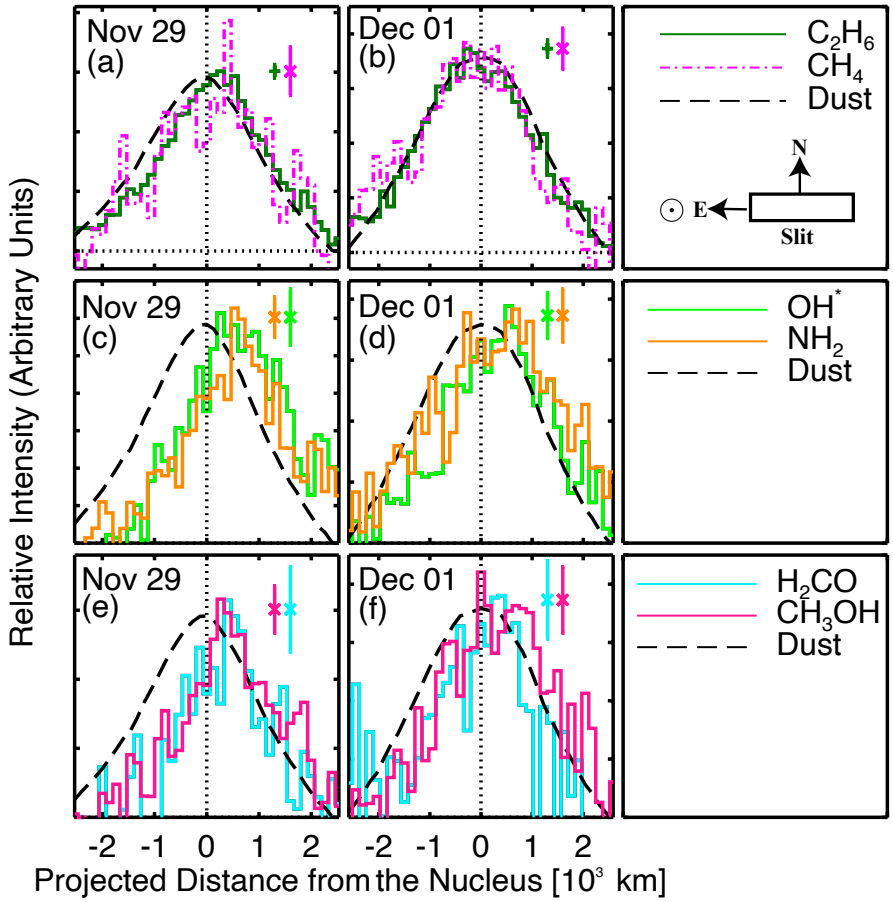

Figure 2. Simultaneously measured spatial profiles on 2020 November 29 [(a), (c), and (e)] and December 1 [(b), (d), and (f)] using the Lp1 setting. The slit was oriented along the Sun-comet direction of ~ 272°, and a favorable phase angle of ~61° on both dates. To ensure uniform spatial registration for all targeted molecular species, the peak of the continuum profile (black-dashed line) is taken to define the nucleus position. The vertical error bars indicated for each volatile species represent ± 1σ stochastic noise.

Compared to the OH* spatial profiles from Lp1, the L-custom OH profile exhibited a greater anti-sunward offset on both dates and was flatter in the anti-sunward direction on December 1, extending well beyond the edge of the slit. Such dramatically different outgassing behavior from simultaneously observed water, coupled with the fact that our prompt emission model does not fit the low-J OH emission lines well, could indicate that fluorescence emission contributed significantly in the L-custom setting [Fig. 3, panel (d)].

This is further supported by noting that the high-J OH lines in Lp1, which are less likely to be excited by fluorescence emission alone, both have similar spatial profiles to other molecules undergoing fluorescent emission and provide a similar water production rate. For this reason, we do not report water production rates inferred from OH lines in the L-custom setting.

NH_2, generally thought to be produced from the photodissociation of NH_3, was also observed for S3. For comets C/2004 Q2 (Machholtz) (Kawakita and Mumma, 2011) and 6P/d'Arrest (Dello Russo et al., 2009a), comparison of the mixing ratio of NH_2 and NH_3 supports NH_3 as the dominant parent molecule of NH_2. In the case of S3, assuming the same growth factor and rotational temperature for both NH_2 and NH_3 results in an NH_2 abundance about twice that of NH_3. Discrepancies in NH_2 and NH_3 abundances have been noted for other comets. For example, Dello Russo et al. (2016b) observed D/2012 S1 (ISON) near R_h = 0.46 AU and derived a production rate or NH_2 less than that of NH_3 by about a factor of five, though this could have been due in part to the non-simultaneous measurement of these molecules and the short-term variability exhibited by comet D/2012 S1, the absence of an appropriate model for a daughter species like NH_2 (Dello Russo et al., 2016b), or the production of NH_2 from a species released when a thermal threshold is reached (Dello Russo et al., 2016a). Even though the R_h at which S3 was observed was similar to that of D/2012 S1, the fact that the production rate of NH_2 was greater than that of NH_3 in S3 as compared to D/2012 S1 (ISON) is intriguing given that the same NH_2 fluorescence model (by Kawakita and Mumma (2011) was used in both comets to obtain the production rates.

In this work, in addition to finding the mixing ratio of NH_2, we also analyzed the spatial profiles of NH_2 to characterize the overall outgassing behavior of S3 (see Fig. 3). Most of the lines used in the analyses of spatial profiles of NH_2 are of lower rotational quantum states and hence are produced mainly by fluorescence emission. The NH_2 spatial profile also shows similar width and offset from the dust as co-measured species HCN and H_2O that also exhibit fluorescence emission (Fig. 3).

Due to weak signal-to-noise ratio (SNR) of NH_3 lines, we were not able to obtain the spatial distribution of NH_3 to compare it to that of NH_2 to accurately determine how different the spatial profile of NH_2 from its likely fluorescent emitted parent molecule NH_3.

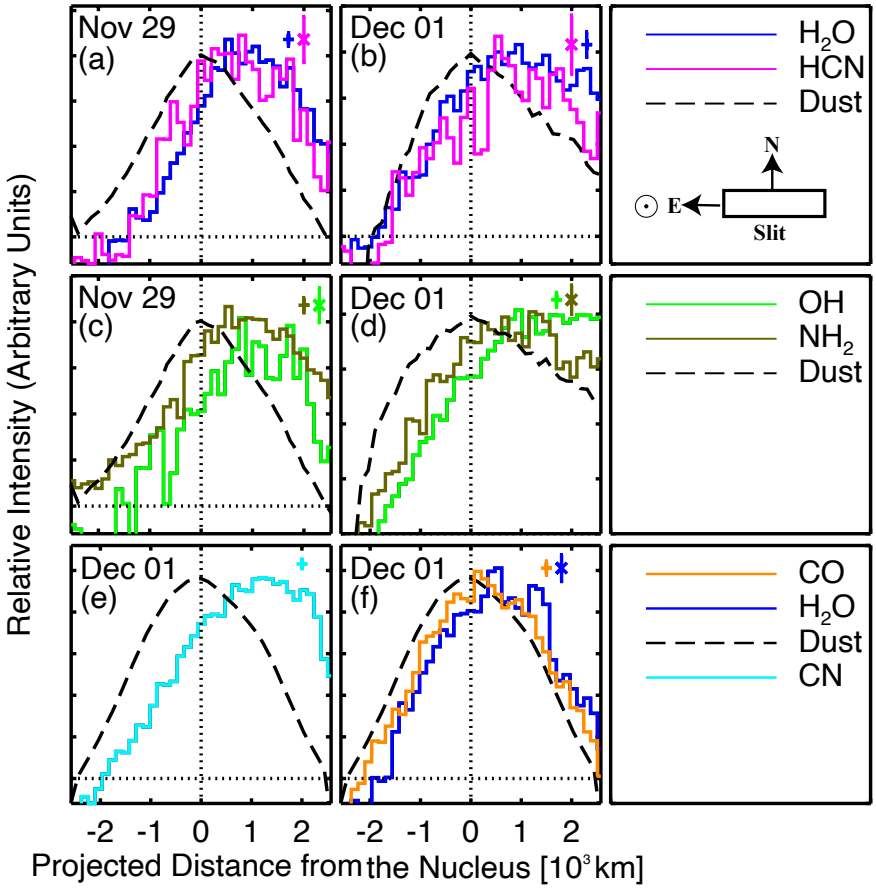

Figure 3. Simultaneously measured spatial profiles using the L-custom and M2-settings on 2020 November 29 and December 1. Panels (a), (b), (c), and (d) indicate the spatial profiles measured on 2020 November 29 and December 1 using the L-custom setting, and panels (e) and (f) indicate the spatial profiles on December 1 using the M2 setting.

4.4.3. M2. Carbon monoxide (CO) and CN were observed simultaneously with H_2O on December 1 using the M2 setting [Fig. 3 (e) and (f)]. CO has a sublimation temperature of ~24K (Crovisier et al., 2000), making it the most volatile species observed in comets at IR wavelengths. While the profile shape and width are very similar to those of H2O, the anti-sunward shift is slightly smaller [Fig. 3(f)].

The CN emission spectra, which include very high energy transitions, require a very high temperature (> 200 K) and are not well fit by the currently existing fluorescent models (e.g., Dello Russo et al., 2016a,b; Roth et al., 2018). This is consistent with what was observed in the optical for comet D/2012 S1 (ISON) at a similar R_h (McKay, priv. comm.), confirming that daughter species have higher rotational excitation temperatures than their parents. Thus, we do not report the production rate nor abundance of CN in this work. The spatial profile of CN is highly asymmetric and broad compared to the co-observed dust, with a greater shift toward the anti-sunward direction than for any other molecule [Figs. 2 and 3]. Similar behavior was noted for comets D/2012 S1 (Dello Russo et al., 2016b) and 153P/Ikeya-Zhang (Dello Russo et al., 2004), which were observed at a similar heliocentric distance. This spatial distribution suggests a different, extended source for CN that does not follow the spatial distribution of the continuum dust. As discussed in section 5.1, this is further supported by the fact that the HCN production rate in S3 is insufficient to account for the CN observed in the optical wavelength range (Jehin et al., 2020a,b), which indicates a possible release of additional CN from an extended source once a thermal threshold is reached (Dello Russo et al., 2016a).

5. DISCUSSION

5.1. PRODUCTION RATES AND MIXING RATIOS

H_2O, the most abundant species in the coma of comets, is routinely detected at infrared wavelengths. The H_2O production rate we measured on November 29 using the L-custom setting was $1.49 \pm 0.18 \times 10^{29}$ molecules s^{-1}, while on December 01, we measured $Q(H_2O)$ of $2.00 \pm 0.23 \times 10^{29}$ molecules s^{-1} and $2.22 \pm 0.29 \times 10^{29}$ molecules s^{-1} using L-custom and M2, respectively. Thus, the H_2O production rate on December 1 was higher than its value on November 29, roughly by a factor of one and a half.

This increase in H_2O production rate before perihelion is consistent with the measurements of Combi et al. (2023), who reported a maximum value five days before perihelion. However, we note that there is a gap in SWAN observations between this maximum water production date until 39 days after the perihelion where the water production rate could have been potentially larger.

To obtain the global production rate, our technique to determine the GFs involves averaging along both sides of a spatial profile to average out asymmetries (e.g., Villanueva et al., 2011a). In the scenario where the spatial profiles were sufficiently offset and were considerably off the chip on the right side, we used the left side of the profile to determine the GF. The agreement of H_2O production rates for the L-custom and M2 settings on December 1 demonstrates the robustness of this method. For abundance ratios, co-observed H_2O was used when available, and for species acquired in the Lp1 setting, L-custom H_2O was used since it was observed on both dates. We note that this may lead to systematic differences in abundance, given that the spatial distributions of volatiles in the Lp1 setting are different from that of H_2O in L-custom. However, since the uncertainties in production rates take into account uncertainties in GFs as well as uncertainty in Γ, the uncertainty introduced into the abundance as a result of using production rates between different settings (non-simultaneous measurements) is accounted for. We also add that the OH prompt emission in Lp1 gives a H_2O production rate that is consistent with the H_2O production rates in the L-custom setting.

Combi et al. (2023) also reported water production rates from 2020 October 29 through 2021 February 13, using the Solar Wind ANisotropies (SWAN) instrument on board the Solar and Heliospheric Observer (SOHO) satellite. They found a steep R_h^{-5} heliocentric distance dependence as S3 approached perihelion. The increase in the H_2O production rate we observed between the two dates is consistent with this increase; however, their absolute production rates are lower than ours by a factor of $\sim$ 2-2.5 compared to the same dates. It is not unusual for the SOHO/SWAN water production rates to differ from those measured in the NIR.

If the SOHO values are larger, it is often attributed to icy grains releasing water into the coma outside the smaller field of view of instruments like iSHELL. One example was 46P/Wirtanen (Combi et al., 2020; McKay et al., 2021). Similarly, water values reported for comet D/2012 S1 in the NIR (Dello Russo et al., 2016b; DiSanti et al., 2016) were slightly less than those reported by Combi et al. (2014). However, the much larger field of view of SOHO/SWAN ($5^\circ \times 5^\circ$ with $1^\circ \times 1^\circ$ pixels) compared to iSHELL (15″ long slit with 0.16″/pixel) means that rapid changes in comet productivity will be detected by and leave the field of view of NIR detectors before filling the beam of SOHO/SWAN. Given the difference in outflow velocities, ~1.2 km s^{-1} for primary volatiles in the NIR and ~8-20 km s^{-1} for H atoms produced from photodissociation measured by SOHO (e.g., Combi et al., 2019), a time delay on the order of days would be expected between sensing dramatic production rate changes with iSHELL vs. SWAN. Our production rates on November 29 and December 1 are in agreement with those measured by SWAN about three to five days later, consistent with this scenario.

Carbonyl sulfide (OCS) is the only sulfur-bearing species with strong fluorescence emission lines at infrared wavelengths and is only measured in ~ ten comets to date, including radio observations (Saki et al., 2020). Thus, our study of S3 provides a vital addition to the abundance measurements of OCS within the comet population. The OCS abundance we measured in S3 is consistent with measurements in other comets (both OCCs and JFCs) obtained over R_h ranging from 0.47-1.04 AU: C/2012 S1 (Dello Russo et al., 2016b), C/2015 ER61 (Saki et al., 2021), 2P/Encke (Roth et al., 2018), and C/2021 A1 (Leonard) (Faggi et al., 2023).

We compared the abundances of secondary species C_2 and CN with respect to simultaneously measured OH from the TRAPPIST in the optical (Jehin et al., 2020a,b) at R_h = 0.87 AU and 1.42 AU to the abundances of HCN, C_2H_2 with respect to co-measured H_2O during both nights of our observations at R_h = 0.52 AU and 0.49 AU.

The abundances of C_2H_2 and HCN with respect to H_2O are significantly less than that of C_2 and CN, respectively. This possibly indicates additional sources for these daughter molecules. The inconsistency between abundances of secondary species in the optical and their potentially primary molecules in the NIR is also reported by Lippi et al. (2023) in comet C/2021 A1 (Leonard). In general, the inconsistency between abundances of daughter species from cometary ices in the optical and their potential parents in the infrared have been noted in many comets possibly due to a significant source of C_2 and CN from grians in those comets (Dello Russo et al., 2016a).

5.2. COMPARISON OF S3 ABUNDANCE RATIOS WITH COMETS OBSERVED AT SIMILAR R_h

To better place S3 in context, we compare our measured abundances with other Oort cloud comets. It was noted by Dello Russo et al. (2016a) that many comets observed within $R_h \sim 0.8$ AU exhibited a systematic enrichment in H_2CO, NH_3, and C_2H_2 relative to comets measured at larger R_h. For example, comet D/2012 S1 was observed on several UT dates spanning R_h = 1.21-0.35 AU and exhibited significant enhancements in abundances of those three molecules, plus HCN, when observed within $R_h \sim 0.6$ AU compared with $R_h > 0.8$ AU (DiSanti et al., 2016). This suggests an additional source in the coma, possibly from the photodissociation of more complex progenitors associated with dust grains. This gives rise to the question of whether NIR spectroscopic measurements of comets near the Sun (within approximately 0.8 AU) truly measure only the nucleus composition of these molecules or whether the actual ice abundances are lower than implied by the coma measurements. Since observations of individual comets over a wide range of R_h are generally unavailable, primarily due to observational constraints, we compare the S3 abundances to those obtained for the sample of OCCs measured within ~ 0.8 AU and those observed at $R_h > 0.8$ AU. Table 3 summarizes the abundances of these molecules from comets observed at $R_h \leq 0.80$ AU.

Table 4 compares the average abundances of S3 to those of all OCCs observed at R_h greater than 0.8 AU from the Sun, all OCCs observed within 0.8 AU from the Sun, and the overall average for all comets. As can be seen from this comparison, when there is a systematic difference in composition for comets observed close to the Sun (as for H_2CO, NH_3, and C_2H_2), the abundance of each molecule in S3 is more similar to the sample of comets observed at small R_h (see Fig. 4), consistent with what was found by DiSanti et al. (2016) and Dello Russo et al. (2016b) for comet ISON.

The enhancement in these three volatile species at such a close distance to the Sun might be due to semi-volatile sources for these molecular species. For example, ammonium salt species ($NH_4^+Cl^-$, $NH_4^+CN^-$, $NH_4^+OCN^-$, $NH_4^+HCOO^-$, and $NH_4^+CH_3COO^-$) were detected by the Rosetta mission in comet 67P/Churyumov-Gerasimenko (Altwegg et al., 2020). At low temperatures, ammonia easily reacts with acids, such as HCN, HNCO, and HCOOH, to create ammonium salts ($NH_4^+X^-$), thus, they may be present in other cometary nuclei as well (e.g., Altwegg et al., 2020; Poch et al., 2020). Ammonium salts are degraded to ammonia at higher temperatures (at small R_h). Dello Russo et al. (2016b) found a double-peaked NH_3 spatial profile in comet D/2012 ISON, indicative of NH_3 being produced in the coma. The NH_3 lines in S3 were too weak to provide a quality spatial profile, but the strongly enriched NH_3 abundance in S3 possibly hints at ammonium salt as a distributed source in the coma.

The production rate of H_2CO obtained from radio observation for comet C/1995 O1 (Hale-Bopp) also showed an increase with decreasing heliocentric distance (Biver et al., 2002). Apart from additional H_2CO possibly coming from a distributed source (less volatile than H_2CO itself) in a coma, it has been suggested that thermal degradation of formaldehyde polymers, polyoxymethylene (POM), on grains into gaseous H_2CO can explain this increase in production rate (Cottin et al., 2001; Fray et al., 2006).

Thus, even though we do not see any clear indication of distributed sources for H_2CO in the spatial distribution for S3 during both dates of our observations, it is possible that the enhancement of H_2CO abundance for S3 at such small R_h could be explained by the same mechanism.

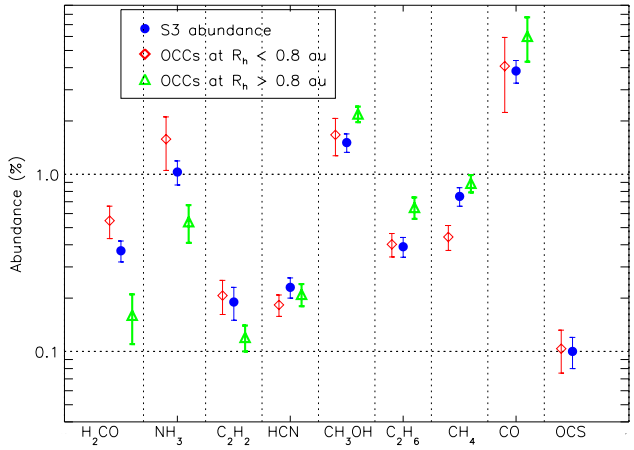

Figure 4. The abundance of primary volatiles in comet C/2020 S3 compared with OCCs. The filled blue circles are measurements for S3 compared with weighted average abundance ratios in OCC populations observed in the near-IR (at $R_h \leq 0.80$ AU and $R_h > 0.80$ AU).

Our results indicate that compared to the mean abundances among OCCs characterized in the NIR at $R_h > 0.80$ AU, S3 is more strongly enriched in H_2CO and NH_3, slightly enriched in C_2H_2, depleted in CH_3OH and C_2H_6, while it is near-average in HCN, CH_4, and CO (see Fig. 4). We note that the enrichment in abundances we measured for H_2CO, NH_3, and C_2H_2 is consistent with what DiSanti et al. (2016) and Dello Russo et al. (2016b) found for comet ISON and for the average of comets measured at $R_h < 0.80$ AU. We also compared the abundances measured in S3 to the mean abundances of each species from the overall comet population (JFCs and OCCs together). This comparison indicates that S3 is depleted in CH_3OH and near-average in all eight other species measured (see Table 4).

We note that even though the relatively large GFs determined for the volatile species of S3 might point to the evidence for an extended source, it can also be due to bad seeing for daytime observations of S3, given that the spatial profiles of H_2CO on both dates of our observations do not indicate the presence of a clear extended (distributed) source in the coma (see Fig. 2). In general, if the trends in enrichments of some volatile species observed for comets close to the Sun is consistent with the hypothesis that some molecules originate from alternative sources, comets observed beyond 0.8 AU might be preferred for overall compositional studies of the nucleus. On the other hand, this implies that comets observed close to the Sun may provide crucial information for explaining processes and molecules that are not generally observable when further from the Sun.

6. SUMMARY

On UT dates 2020, November 29, and December 1, we obtained pre-perihelion spectra of comet C/2020 S3 (Erasmus) using the echelle spectrograph iSHELL at the NASA IRTF. Our observations spanned a heliocentric distance of R_h = 0.49 - 0.53 AU. We report production rates and abundance ratios (relative to simultaneously or contemporaneously measured H_2O) for nine detected trace NIR-active volatiles (C_2H_2, HCN, NH_3, H_2CO, CH_3OH, C_2H_6, CH_4, OCS, and CO). We compared the abundance ratios of molecules measured in S3 to their overall mean abundances in all comets (JFCs and OCCs) measured at NIR wavelengths. Our main conclusions are summarized below.

1. Compared to the mean abundances in the overall comet population, our results indicate that CH_3OH is depleted; the remaining eight species are consistent with the average comet composition (rightmost column of Table 4). In addition, compared to OCCs measured to date at $R_h > 0.80$ AU, S3 is enriched in H_2CO, NH_3, and C_2H_2, which may be due in part to an additional source(s) released in the coma at smaller heliocentric distances (e.g., Dello Russo et al., 2016a,b; DiSanti et al., 2016).

Spatial profiles for apolar molecules (CH_4 and C_2H_6) were similar to each other but different from the co-observed polar molecules (H_2CO and CH_3OH or NH_2 and OH^*). Daughter molecules in S3 generally exhibited outgassing behavior with large offsets from the nucleus (Figs. 2 and 3). Compared to parent species, daughter molecules (e.g., OH-fluorescent, CN, and NH_2) generally had broad, flat spatial distributions.

2. Even though the spatial profiles of most volatile species within the same setting on both dates generally show similar profile shapes and shifts towards the anti-sunward direction, there are notable differences in the profiles between non-simultaneous settings, which could be due to temporal variability in outgassing between these non-simultaneous measurements. Compared to Lp1, the spatial profiles from the L-custom setting show stronger asymmetry in the anti-sunward direction. Variable outgassing behavior between the settings may be expected as outgassing sources rotate in or out of the field of view (i.e., change in observing geometry).

3. The variable outgassing behavior of comet S3, which is revealed by the spatial profiles measured non-simultaneously, along with the compositional variations between comets observed at $R_h \leq 0.80$ AU and $R_h > 0.80$ AU, highlight the necessity of observing more comets over a wider range of heliocentric distances, including those that are close to the Sun. The flexible scheduling of IRTF over numerous dates makes these serial measurements a good fit for the iSHELL instrument.

Table 2. Volatile composition of comet S3 obtained using iSHELL

Setting	Mol.	$T_{rot}^{(a)}$ (K)	GF$^{(b)}$	Q$^{(c)}$ (10^{26} mol s^{-1})	$\frac{Q_X}{Q_{H_2O}}^{(d)}$ (%)	$\frac{Q_X}{Q_{C_2H_6}}^{(e)}$
	2020 Nov 29, R_h=0.52 AU, Δ = 1.10 AU, dΔ/dt = 18.65 km s^{-1}					
L-custom	H_2O	95 ± 3	3.36 ± 0.32	1490 ± 180	100	266 ± 48.34
	HCN	101^{+8}_{-7}	3.43 ± 0.32	3.47 ± 0.41	0.23 ± 0.04	0.62 ± 0.11
		(95)	3.43	3.43 ± 0.41	0.23 ± 0.04	0.61 ± 0.11
	C_2H_2	(95)	(3.36)	2.76 ± 0.42	0.19 ± 0.04	0.49 ± 0.10
	NH_3	(95)	(3.36)	16.30 ± 1.80	1.09 ± 0.19	2.90 ± 0.51
	NH_2	(95)	(3.36)	22.80 ± 2.50	1.53 ± 0.27	4.06 ± 0.71
Lp1	C_2H_6	107^{+17}_{-14}	2.84 ± 0.14	5.90 ± 0.56	0.40 ± 0.06	1.00
		(95)	2.84	5.61 ± 0.54	0.38 ± 0.06	1.00
	CH_4	(95)	(2.84)	11.20 ± 1.10	0.75 ± 0.12	2.00 ± 0.22
	OH*	(95)	(2.84)	1140 ± 102	76.5 ± 11.5	203 ± 18
	CH_3OH	106^{+7}_{-6}	(2.84)	24.1 ± 2.20	1.62 ± 0.26	4.29 ± 0.44
		(95)	(2.84)	22.3 ± 2.10	1.50 ± 0.24	3.99 ± 0.41
	H_2CO	106^{+10}_{-9}	(2.84)	5.79 ± 0.63	0.39 ± 0.07	1.03 ± 0.12
		(95)	(2.84)	5.48 ± 0.60	0.37 ± 0.06	0.98 ± 0.12
	2020 Dec 01, R_h=0.49 AU, Δ = 1.12 AU, dΔ/dt = 21.67 km s^{-1}					
M2	H_2O	114 ± 9	3.39 ± 0.38	2210 ± 290	100	267.67 ± 53.56
	CO	121^{+8}_{-7}	3.19 ± 0.32	85.80 ± 9.70	3.89 ± 0.57	10.40 ± 1.89
		(114)	(3.19)	84.4 ± 9.6	3.83 ± 0.56	10.24 ± 1.86
	OCS	(121)	(3.39)	2.25 ± 0.37	0.10 ± 0.02	0.27 ± 0.06
		(114)	(3.39)	2.21 ± 0.37	0.10 ± 0.02	0.27 ± 0.06
L-custom	H_2O	98± 4	3.69 ± 0.70	2000 ± 230	100	242.13 ± 59.33
	HCN	86^{+6}_{-5}	(3.69)	4.66 ± 0.94	0.23 ± 0.07	0.57 ± 0.17
		(98)	(3.69)	4.81 ± 0.97	0.24 ± 0.07	0.58 ± 0.17
	C_2H_2	(98)	(3.69)	4.69 ± 1.06	0.24 ± 0.16	0.57 ± 0.18
	NH_3	(98)	(3.69)	16.7 ± 4.4	0.84 ± 0.33	2.02 ± 0.69
	NH_2	(98)	(3.69)	35.7 ± 6.9	1.79 ± 0.54	4.33 ± 1.25
Lp1	C_2H_6	107^{+17}_{-14}	3.14 ± 0.28	8.52 ± 0.86	0.43 ± 0.08	1.00
		(98)	(3.14)	8.23 ± 0.83	0.41 ± 0.07	1.00
	CH_4	(98)	3.19 ± 0.13	14.7 ± 1.90	0.74 ± 0.13	1.79 ± 0.27
	OH*	(98)	(3.14)	1732 ± 119	86.8 ± 11.8	210 ±25
	CH_3OH	107 ± 8	(3.14)	32.1 ± 3.10	1.61 ± 0.28	3.89 ± 0.51
		(98)	(3.14)	30.4 ± 3.0	1.53 ± 0.27	3.69 ± 0.60
	H_2CO	85 ± 10	(3.14)	6.73 ± 0.79	0.34 ± 0.06	0.82 ± 0.11
		(98)	(3.14)	7.20 ± 0.84	0.36 ± 0.07	0.87 ± 0.15

Notes: [a] Rotational temperature. Values in parentheses are assumed.

[b] Growth factor. Values in the parentheses are assumed.

[c] Global production rate. Production rate uncertainty includes line-by-line deviation between the modeled and observed intensities and photon noise (e.g., Bonev et al., 2007; Dello Russo et al., 2004)

[d] Molecular abundance with respect to H_2O.

[e] Molecular abundance with respect to C_2H_6

Table 3. The volatile composition of OCCs measured at $R_h \leq 0.80$ AU

Comet[a]	R_h (AU)	Molecules			
		H_2CO	NH_3	C_2H_2	HCN
S3	0.49 - 0.52	0.37 ± 0.05	1.09 ± 0.19	0.19 ± 0.04	0.23 ± 0.03
S1	0.35-0.59	1.10 ± 0.30	3.63 ± 0.56	0.24 ± 0.02	0.28 ± 0.02
E4	0.66	0.36 ± 0.03	1.86 ± 0.36	0.14 ± 0.02	0.17 ± 0.02
V5	0.70-0.79	0.13 ± 0.02	0.74 ± 0.08	0.07 ± 0.01	0.08 ± 0.01
153P	0.51-0.78	0.83 ± 0.24	-	0.21 ± 0.05	0.21 ± 0.03
T7	0.69	0.79 ± 0.09	-	-	-
P1	0.55	0.49 ± 0.09	1.50 ± 0.30	0.45 ± 0.08	0.24 ± 0.03
F6	0.75	0.54 ± 0.12	-	-	-
B2	0.64-0.73	-	-	0.25 ± 0.10	0.20 ± 0.03
A1	0.62-0.68	0.14 ± 0.01	< 0.34	0.09 ± 0.01	0.11 ± 0.01

Notes: [a] S1 ≡ C/2012 S1 ISON (Dello Russo et al., 2016b; DiSanti et al., 2016), E4 ≡ C/2017 E4 (Faggi et al., 2018), V5 ≡ C/2013 V5 (DiSanti et al., 2018), 153P ≡153P/Ikeya-Zhang (Dello Russo et al., 2004, 2016a; Disanti et al., 2002; Gibb et al., 2003), T7 ≡ C/2002 T7 Linear (DiSanti et al., 2006), P1 ≡ C/2006 P1 (Dello Russo et al., 2009b), F6 ≡ C/2012 F6 (Paganini et al., 2014), B2 ≡ C/1996 B2 (Brooke et al., 1996; Dello Russo et al., 2002; DiSanti et al., 2003; Magee-Sauer et al., 2002) , A1 ≡ C/2021 A1 (Faggi et al., 2023).

Table 4. Weighted mean abundances for the detected molecules in S3

Molecule	Weighted mean in S3	OCC Average [a] ($R_h > 0.80$ AU)	OCC Average [b] $R_h \leq 0.80$ AU)	Average in all comets[d] (%)
C_2H_2	0.19 ± 0.06	0.12 ± 0.02	0.21 ± 0.05	0.12 ± 0.02
HCN	0.23 ± 0.03	0.21 ± 0.03	0.18 ± 0.03	0.20 ± 0.02
NH_3	1.03 ± 0.16	0.54 ± 0.13	1.58 ± 0.53	0.78 ± 0.16
H_2CO	0.37 ± 0.05	0.16 ± 0.05	0.55 ± 0.11	0.27 ± 0.05
CH_3OH	1.51 ± 0.18	2.19 ± 0.22	1.67 ± 0.40	2.20 ± 0.19
C_2H_6	0.39 ± 0.05	0.65 ± 0.09	0.40 ± 0.06	0.53 ± 0.05
CH_4	0.75 ± 0.09	0.89 ± 0.10	0.44 ± 0.07	0.71 ± 0.07
CO	3.83 ± 0.56	6.01 ± 1.69	4.08 ± 1.85	4.15 ± 1.04
OCS	0.10 ± 0.02	-	0.10 ± 0.03[c]	0.15 ± 0.04[e]

Notes: [a] Average abundance values among OCCs measured in NIR at $R_h > 0.8$ AU. The uncertainties associated with the unweighted average values correspond to the standard deviation from the mean abundances divided by the square root of the number of measurements.
[b] Average abundance values among OCCs measured in near-IR at $R_h \leq 0.80$ AU, which includes comets listed in Table 3.
[c] Weighted average of OCS from comets observed in the near-IR at $R_h \leq 0.80$ AU: C/2021 A1 (Faggi et al., 2023), C/2012 S1 (Dello Russo et al., 2016b), and C/2002 T7 (Saki et al., 2020).
[d] Average abundance in all comets (OCCs and JFCs) observed in near-IR at all R_h values.
[e] C/1995 O1 (Dello Russo et al., 1998), 2P/Encke (Roth et al., 2018), 21P/Giacobini-Zinner (Saki et al., 2020), and OCCs from which the weighted average OCS measurements are indicated in the table.

ACKNOWLEDGEMENTS

Data for this study were obtained with Director's Discretionary Time at the NASA Infrared Telescope Facility (IRTF), operated by the University of Hawai'i under contract NNH14CK55B with NASA. The authors gratefully acknowledge the support of the IRTF staff for their help in acquiring the S3 data. EG, YK, and CE acknowledge support from NSF under award AST-2009910. This work was supported by the Planetary Science Division Internal Scientist Funding Program through the Fundamental Laboratory Research (FLaRe) work package (NXR). MC gratefully acknowledges the support from NASA SSO Program grant 80NSSC23K0030. BPB acknowledges the NFS award AST-2009398 and NASA award EW 80NSSC20K0341.

REFERENCES

A'Hearn, M. F., Millis, R. C., Schleicher, D. O., Osip, D. J., and Birch, P. V. (1995). The ensemble properties of comets: Results from narrowband photometry of 85 comets, 1976-1992. Icarus, 118(2):223–270.

Altwegg, K., Balsiger, H., Hänni, N., Rubin, M., Schuhmann, M., Schroeder, I., Sémon, T., Wampfler, S., Berthelier, J.-J., Briois, C., Combi, M., Gombosi, T. I., Cottin, H., De Keyser, J., Dhooghe, F., Fiethe, B., and Fuselier, S. A. (2020). Evidence of ammonium salts in comet 67P as explanation for the nitrogen depletion in cometary comae. *Nature Astronomy*, 4:533–540.

Biver, N., Bockelée-Morvan, D., Colom, P., Crovisier, J., Henry, F., Lellouch, E., Winnberg, A., Johansson, L. E. B., Gunnarsson, M., Rickman, H., Rantakyrö, F., Davies, J. K., Dent, W. R. F., Paubert, G., Moreno, R., Wink, J., Despois, D., Benford, D. J., Gardner, M., Lis, D. C., Mehringer, D., Phillips, T. G., and Rauer, H. (2002). The 1995 2002 Long-Term Monitoring of Comet C/1995 O1 (HALE BOPP) at Radio Wavelength. *Earth Moon and Planets*, 90(1):5–14.

Biver, N., Bockelée-Morvan, D., Crovisier, J., Lis, D. C., Moreno, R., Colom, P., Henry, F., Herpin, F., Paubert, G., and Womack, M. (2006). Radio wavelength molecular observations of comets C/1999 T1 (McNaught-Hartley), C/2001 A2 (LINEAR), C/2000 WM_1 (LINEAR) and 153P/Ikeya-Zhang. A&A, 449(3):1255–1270.

Bockelée-Morvan, D., Crovisier, J., Mumma, M. J., and Weaver, H. A. (2004). The composition of cometary volatiles. In Festou, M. C., Keller, H. U., and Weaver, H. A., editors, *Comets II*, page 391. University of Arizona Press.

Bonev, B. P. (2005). *Towards a Chemical Taxonomy of Comets: Infrared Spectroscopic Methods for Quantitative Measurements of Cometary Water*. PhD thesis, University of Toledo, Ohio.

Bonev, B. P., Dello Russo, N., DiSanti, M. A., Martin, E. C., Doppmann, G., Vervack, Ronald J., J., Villanueva, G. L., Kawakita, H., Gibb, E. L., Combi, M. R., Roth, N. X., Saki, M., McKay, A. J., Cordiner, M. A., Bodewits, D., Crovisier, J., Biver, N., Cochran, A. L., Shou, Y., Khan, Y., and Venkataramani, K. (2021). First Comet Observations with NIRSPEC-2 at Keck: Outgassing Sources of Parent Volatiles and Abundances Based on Alternative Taxonomic Compositional Baselines in 46P/Wirtanen. *Planetary Science Journal*, 2(2):45.

Bonev, B. P. and Mumma, M. J. (2006). A Comprehensive Study of Infrared OH Prompt Emission in Two Comets. II. Implications for Unimolecular Dissociation of H_2O. ApJ, 653(1):788–791.

Bonev, B. P., Mumma, M. J., Villanueva, G. L., Disanti, M. A., Ellis, R. S., Magee-Sauer, K., and Dello Russo, N. (2007). A Search for Variation in the H_2O Ortho-Para Ratio and Rotational Temperature in the Inner Coma of Comet C/2004 Q2 (Machholz). ApJ, 661(1):L97–L100.

Bonev, B. P., Villanueva, G. L., DiSanti, M. A., Boehnhardt, H., Lippi, M., Gibb, E. L., Paganini, L., and Mumma, M. J. (2017). Beyond 3 au from the Sun: The Hypervolatiles CH_4, C_2H_6, and CO in the Distant Comet C/2006 W3 (Christensen). AJ, 153(5):241.

Brooke, T. Y., Tokunaga, A. T., Weaver, H. A., Crovisier, J., Bockelée-Morvan, D., and Crisp, D. (1996). Detection of acetylene in the infrared spectrum of comet Hyakutake. Nature, 383(6601):606–608.

Brooke, T. Y., Weaver, H. A., Chin, G., Bockelée-Morvan, D., Kim, S. J., and Xu, L. H. (2003). Spectroscopy of Comet Hale-Bopp in the infrared. Icarus, 166(1):167–187.

Combi, M. R., Fougere, N., Mäkinen, J. T. T., Bertaux, J. L., Quémerais, E., and Ferron, S. (2014). Unusual Water Production Activity of Comet C/2012 S1 (ISON): Outbursts and Continuous Fragmentation. ApJ, 788(1):L7.

Combi, M. R., Mäkinen, T., Bertaux, J. L., Quémerais, E., and Ferron, S. (2023). Water production rates from SOHO/SWAN observations of comets C/2020 S3 (Erasmus), C/2021 A1 (Leonard) and C/2021 O3 (PanSTARRS). Icarus, 398:115543.

Combi, M. R., Mäkinen, T., Bertaux, J. L., Quémerais, E., Ferron, S., and Coronel, R. (2020). Comet 41P/Tuttle-Giacobini-Kresak, 45P/Honda-Mrkos-Pajdusakova, and 46P/Wirtanen: Water Production Activity over 21 yr with SOHO/SWAN. *Planetary Science Journal*, 1(3):72.

Combi, M. R., Mäkinen, T. T., Bertaux, J. L., Quémerais, E., and Ferron, S. (2019). A survey of water production in 61 comets from SOHO/SWAN observations of hydrogen Lyman-alpha: Twenty-one years 1996-2016. Icarus, 317:610–620.

Cottin, H., Gazeau, M. C., Benilan, Y., and Raulin, F. (2001). Polyoxymethylene as Parent Molecule for the Formaldehyde Extended Source in Comet Halley. ApJ, 556(1):417–420.

Crovisier, J., Bockelée-Morvan, D., Colom, P., Biver, N., Despois, D., Lis, D. C., and Target-of-opportunity Radio Observations of Comets Team (2004). The composition of ices in comet C/1995 O1 (Hale-Bopp) from radio spectroscopy. Further results and upper limits on undetected species. A&A, 418:1141–1157.

Crovisier, J., Encrenaz, T., Lyle, S., and Bonnet, F. b. R. M. (2000). *Comet Science*. Cambridge University Press.

Dello Russo, N., DiSanti, M. A., Magee-Sauer, K., Gibb, E. L., Mumma, M. J., Barber, R. J., and Tennyson, J. (2004). Water production and release in Comet 153P/Ikeya-Zhang (C/2002 C1): accurate rotational temperature retrievals from hot-band lines near 2.9-μm. Icarus, 168(1):186–200.

Dello Russo, N., DiSanti, M. A., Mumma, M. J., Magee-Sauer, K., and Rettig, T. W. (1998). Carbonyl Sulfide in Comets C/1996 B2 (Hyakutake) and C/1995 O1 (Hale-Bopp): Evidence for an Extended Source in Hale-Bopp. Icarus, 135(2):377–388.

Dello Russo, N., Kawakita, H., Bonev, B. P., Vervack, R. J., Gibb, E. L., Shinnaka, Y., Roth, N. X., DiSanti, M. A., and McKay, A. J. (2020). Post-perihelion volatile production and release from Jupiter-family comet 45P/Honda-Mrkos-Pajdušáková. Icarus, 335:113411.

Dello Russo, N., Kawakita, H., Vervack, R. J., and Weaver, H. A. (2016a). Emerging trends and a comet taxonomy based on the volatile chemistry measured in thirty comets with high-resolution infrared spectroscopy between 1997 and 2013. Icarus, 278:301–332.

Dello Russo, N., Mumma, M. J., DiSanti, M. A., and Magee-Sauer, K. (2002). Production of ethane and water in comet C/1996 B2 Hyakutake. *Journal of Geophysical Research (Planets)*, 107(E11):5095.

Dello Russo, N., Vervack, R. J., J., Weaver, H. A., Kawakita, H., Kobayashi, H., Biver, N., Bockelée-Morvan, D., and Crovisier, J. (2009a). The Parent Volatile Composition of 6p/d'Arrest and a Chemical Comparison of Jupiter-Family Comets Measured at Infrared Wavelengths. ApJ, 703(1):187–197.

Dello Russo, N., Vervack, R. J., Kawakita, H., Cochran, A., McKay, A. J., Harris, W. M., Weaver, H. A., Lisse, C. M., DiSanti, M. A., Kobayashi, H., Biver, N., Bockelée-Morvan, D., Crovisier, J., Opitom, C., and Jehin, E. (2016b). The compositional evolution of C/2012 S1 (ISON) from ground-based high-resolution infrared spectroscopy as part of a worldwide observing campaign. Icarus, 266:152–172.

Dello Russo, N., Vervack, R. J., Weaver, H. A., and Lisse, C. M. (2009b). Infrared measurements of the chemical composition of C/2006 P1 McNaught. Icarus, 200(1):271–279.

DiSanti, M. A., Bonev, B. P., Dello Russo, N., McKay, A. J., Roth, N. X., Saki, M., Gibb, E. L., Vervack, Ronald J., J., Khan, Y., and Kawakita, H. (2021). Volatile Composition and Outgassing in C/2018 Y1 (Iwamoto): Extending Limits for High-resolution Infrared Cometary Spectroscopy between 2.8 and 5.0 μm. *Planetary Science Journal*, 2(6):225.

DiSanti, M. A., Bonev, B. P., Gibb, E. L., Paganini, L., Villanueva, G. L., Mumma, M. J., Keane, J. V., Blake, G. A., Dello Russo, N., Meech, K. J., Vervack, R. J., J., and McKay, A. J. (2016). En Route to Destruction: The Evolution in Composition of Ices in Comet D/2012 S1 (ISON) between 1.2 and 0.34 AU from the Sun as Revealed at Infrared Wavelengths. ApJ, 820(1):34.

DiSanti, M. A., Bonev, B. P., Gibb, E. L., Roth, N. X., Dello Russo, N., and Vervack, Ronald J., J. (2018). Comet C/2013 V5 (Oukaimeden): Evidence for Depleted Organic Volatiles and Compositional Heterogeneity as Revealed through Infrared Spectroscopy. AJ, 156(6):258.

DiSanti, M. A., Bonev, B. P., Magee-Sauer, K., Dello Russo, N., Mumma, M. J., Reuter, D. C., and Villanueva, G. L. (2006). Detection of Formaldehyde Emission in Comet C/2002 T7 (LINEAR) at Infrared Wavelengths: Line-by-Line Validation of Modeled Fluorescent Intensities. ApJ, 650(1):470–483.

DiSanti, M. A., Bonev, B. P., Russo, N. D., Vervack, Ronald J., J., Gibb, E. L., Roth, N. X., McKay, A. J., Kawakita, H., Feaga, L. M., and Weaver, H. A. (2017). Hypervolatiles in a Jupiter-family Comet: Observations of 45P/Honda-Mrkos-Pajdušáková Using iSHELL at the NASA-IRTF. AJ, 154(6):246.

DiSanti, M. A., Bonev, B. P., Villanueva, G. L., and Mumma, M. J. (2013). Highly Depleted Ethane and Mildly Depleted Methanol in Comet 21P/Giacobini-Zinner: Application of a New Empirical ν_2-band Model for CH_3OH near 50 K. ApJ, 763(1):1.

Disanti, M. A., dello Russo, N., Magee-Sauer, K., Gibb, E. L., Reuter, D. C., and Mumma, M. J. (2002). CO, H_2CO, and CH_3OH in comet 2002 C1 Ikeya-Zhang. In Warmbein, B., editor, *Asteroids, Comets, and Meteors: ACM 2002*, volume 500 of *ESA Special Publication*, pages 571–574.

DiSanti, M. A., Mumma, M. J., Dello Russo, N., Magee-Sauer, K., and Griep, D. M. (2003). Evidence for a dominant native source of carbon monoxide in Comet C/1996 B2 (Hyakutake). *Journal of Geophysical Research (Planets)*, 108(E6):5061.

DiSanti, M. A., Mumma, M. J., Russo, N. D., and Magee-Sauer, K. (2001). Carbon Monoxide Production and Excitation in Comet C/1995 O1 (Hale-Bopp): Isolation of Native and Distributed CO Sources. Icarus, 153(2):361–390.

DiSanti, M. A., Villanueva, G. L., Paganini, L., Bonev, B. P., Keane, J. V., Meech, K. J., and Mumma, M. J. (2014). Pre- and post-perihelion observations of C/2009 P1 (Garradd): Evidence for an oxygen-rich heritage? Icarus, 228:167–180.

Eistrup, C., Walsh, C., and van Dishoeck, E. F. (2019). Cometary compositions compared with protoplanetary disk midplane chemical evolution. An emerging chemical evolution taxonomy for comets. A&A, 629:A84.

Faggi, S., Lippi, M., Mumma, M. J., and Villanueva, G. L. (2023). Strongly Depleted Methanol and Hypervolatiles in Comet C/2021 A1 (Leonard): Signatures of Interstellar Chemistry? *Planetary Science Journal*, 4(1):8.

Faggi, S., Villanueva, G. L., Mumma, M. J., and Paganini, L. (2018). The Volatile Composition of Comet C/2017 E4 (Lovejoy) before its Disruption, as Revealed by High-resolution Infrared Spectroscopy with iSHELL at the NASA/IRTF. AJ, 156(2):68.

Fray, N., Bénilan, Y., Biver, N., Bockelée-Morvan, D., Cottin, H., Crovisier, J., and Gazeau, M.-C. (2006). Heliocentric evolution of the degradation of polyoxymethylene: Application to the origin of the formaldehyde (H $_2$CO) extended source in Comet C/1995 O1 (Hale-Bopp). Icarus, 184(1):239–254.

Gibb, E. L., Mumma, M. J., Dello Russo, N., DiSanti, M. A., and Magee-Sauer, K. (2003). Methane in Oort cloud comets. Icarus, 165(2):391–406.

Huebner, W. and Mukherjee, J. (2015). Photoionization and photodissociation rates in solar and blackbody radiation fields. *Planetary and Space Science*, 106:11–45.

Jehin, E., Moulane, Y., Manfroid, J., Pozuelos, F., Ferrais, M., and Hutsemekers, D. (2020a). TRAPPIST comet production rates: 88/Howell, C/2020 M3 (ATLAS), C/2020 S3 (Erasmus), 156P/Russell-LINEAR. *The Astronomer's Telegram*, 14174:1.

Jehin, E., Moulane, Y., Manfroid, J., Pozuelos, F., and Hutsemekers, D. (2020b). TRAPPIST comet production rates: 88/Howell, C/2020 M3 (ATLAS), C/2020 S3 (Erasmus), 156P/Russell-LINEAR. *The Astronomer's Telegram*, 14101:1.

Kawakita, H. and Mumma, M. J. (2011). Fluorescence Excitation Models of Ammonia and Amidogen Radical (NH_2) in Comets: Application to Comet C/2004 Q2 (Machholz). ApJ, 727(2):91.

Królikowska, M. and Dybczyński, P. A. (2017). Oort spike comets with large perihelion distances. MNRAS, 472(4):4634–4658.

Lippi, M., Vander Donckt, M., Faggi, S., Moulane, Y., Mumma, M. J., Villanueva, G. L., and Jehin, E. (2023). The volatile composition of C/2021 A1 (Leonard): Comparison between infrared and UV-optical measurements. A&A, 676:A105.

Magee-Sauer, K., Mumma, M. J., DiSanti, M. A., and Dello Russo, N. (2002). Hydrogen cyanide in comet C/1996 B2 Hyakutake. *Journal of Geophysical Research (Planets)*, 107(E11).

McKay, A. J., DiSanti, M. A., Cochran, A. L., Bonev, B. P., Dello Russo, N., Vervack, Ronald J., J., Gibb, E., Roth, N. X., Saki, M., Khan, Y., and Kawakita, H. (2021). Quantifying the Hypervolatile Abundances in Jupiter-family Comet 46P/Wirtanen. *Planetary Science Journal*, 2(1):21.

Mumma, M. J. and Charnley, S. B. (2011). The Chemical Composition of Comets—Emerging Taxonomies and Natal Heritage. ARA&A, 49(1):471–524.

Paganini, L., DiSanti, M. A., Mumma, M. J., Villanueva, G. L., Bonev, B. P., Keane, J. V., Gibb, E. L., Boehnhardt, H., and Meech, K. J. (2014). The Unexpectedly Bright Comet C/2012 F6 (Lemmon) Unveiled at Near-infrared Wavelengths. AJ, 147(1):15.

Poch, O., Istiqomah, I., Quirico, E., Beck, P., Schmitt, B., Theulé, P., Faure, A., Hily-Blant, P., Bonal, L., Raponi, A., Ciarniello, M., Rousseau, B., Potin, S., Brissaud, O., Flandinet, L., Filacchione, G., Pommerol, A., Thomas, N., Kappel, D., Mennella, V., Moroz, L., Vinogradoff, V., Arnold, G., Erard, S., Bockelée-Morvan, D., Leyrat, C., Capaccioni, F., De Sanctis, M. C., Longobardo, A., Mancarella, F., Palomba, E., and Tosi, F. (2020). Ammonium salts are a reservoir of nitrogen on a cometary nucleus and possibly on some asteroids. *Science*, 367(6483):aaw7462.

Radeva, Y. L., Mumma, M. J., Bonev, B. P., DiSanti, M. A., Villanueva, G. L., Magee-Sauer, K., Gibb, E. L., and Weaver, H. A. (2010). The organic composition of Comet C/2000 WM $_1$ (LINEAR) revealed through infrared spectroscopy. Icarus, 206(2):764–777.

Rayner, J., Tokunaga, A., Jaffe, D., Bond, T., Bonnet, M., Ching, G., Connelley, M., Cushing, M., Kokubun, D., Lockhart, C., Vacca, W., and Warmbier, E. (2022). iSHELL: a 1-5 micron R = 80,000 Immersion Grating Spectrograph for the NASA Infrared Telescope Facility. PASP, 134(1031):015002.

Roth, N. X., Gibb, E. L., Bonev, B. P., DiSanti, M. A., Dello Russo, N., Vervack, Ronald J., J., McKay, A. J., and Kawakita, H. (2018). A Tale of "Two" Comets: The Primary Volatile Composition of Comet 2P/Encke Across Apparitions and Implications for Cometary Science. AJ, 156(6):251.

Saki, M., Gibb, E. L., Bonev, B. P., Roth, N. X., DiSanti, M. A., Dello Russo, N., Vervack, Ronald J., J., McKay, A. J., and Kawakita, H. (2020). Carbonyl Sulfide (OCS): Detections in Comets C/2002 T7 (LINEAR), C/2015 ER61 (PanSTARRS), and 21P/Giacobini-Zinner and Stringent Upper Limits in 46P/Wirtanen. AJ, 160(4):184.

Saki, M., Gibb, E. L., Bonev, B. P., Roth, N. X., DiSanti, M. A., Khan, Y., Dello Russo, N., Vervack, Ronald J., J., McKay, A. J., and Kawakita, H. (2021). Chemical Composition of Outbursting Comet C/2015 ER61 (PanSTARRS). AJ, 162(4):145.

Villanueva, G. L., DiSanti, M. A., Mumma, M. J., and Xu, L. H. (2012a). A Quantum Band Model of the ν_3 Fundamental of Methanol (CH_3OH) and Its Application to Fluorescence Spectra of Comets. ApJ, 747(1):37.

Villanueva, G. L., Magee-Sauer, K., and Mumma, M. J. (2013). Modeling of nitrogen compounds in cometary atmospheres: Fluorescence models of ammonia (NH_3), hydrogen cyanide (HCN), hydrogen isocyanide (HNC) and cyanoacetylene (HC_3N). J. Quant. Spec. Radiat. Transf., 129:158–168.

Villanueva, G. L., Mumma, M. J., Bonev, B. P., Novak, R. E., Barber, R. J., and Disanti, M. A. (2012b). Water in planetary and cometary atmospheres: H_2O/HDO transmittance and fluorescence models. J. Quant. Spec. Radiat. Transf., 113(3):202–220.

Villanueva, G. L., Mumma, M. J., DiSanti, M. A., Bonev, B. P., Gibb, E. L., Magee-Sauer, K., Blake, G. A., and Salyk, C. (2011a). The molecular composition of Comet C/2007 W1 (Boattini): Evidence of a peculiar outgassing and a rich chemistry. Icarus, 216(1):227–240.

Villanueva, G. L., Mumma, M. J., and Magee-Sauer, K. (2011b). Ethane in planetary and cometary atmospheres: Transmittance and fluorescence models of the ν_7 band at 3.3 μm. *Journal of Geophysical Research (Planets)*, 116(E8):E08012.

Villanueva, G. L., Smith, M. D., Protopapa, S., Faggi, S., and Mandell, A. M. (2018). Planetary Spectrum Generator: An accurate online radiative transfer suite for atmospheres, comets, small bodies and exoplanets. J. Quant. Spec. Radiat. Transf., 217:86–104.

Vokrouhlický, D., Nesvorný, D., and Dones, L. (2019). Origin and Evolution of Long-period Comets. AJ, 157(5):181.

Willacy, K., Turner, N., Bonev, B., Gibb, E., Dello Russo, N., DiSanti, M., Vervack, Ronald J., J., and Roth, N. X. (2022). Comets in Context: Comparing Comet Compositions with Protosolar Nebula Models. ApJ, 931(2):164.

II. COMPOSITIONAL MEASUREMENTS IN COMET C/2017 K2 (PAN-STARRS) BEYOND 2.3 AU

Chemeda Ejeta[1], Erika Gibb[1], Michael A. DiSanti [2], Hideyo Kawakita [3], Boncho P. Bonev [4], Neil Dello Russo [5], Nathan Roth[2,6], Mohammad Saki [1], Adam J. McKay [7], Younas Khan [8], Ronald J. Vervack Jr. [5], Lori Feaga[9], Michael R. Combi[10], Yinisi Shou[10]

[1] Department of Physics and Astronomy, University of Missouri-St. Louis, Saint Louis, MO 63121, USA

[2] Solar System Exploration Division, Planetary Systems Laboratory, MS 693, NASA Goddard Space Flight Center, Greenbelt, MD 20771, USA

[3] National Astronomical Observatory of Japan, 2-21-1 Osawa, Mitaka, Tokyo 181-8588, Japan

[4] Department of Physics, American University, Washington, DC 20016, USA

[5] Johns Hopkins Applied Physics Lab Laurel, MD 20723, USA

[6] Catholic University of America, Washington, DC

[7] Department of Physics and Astronomy, Appalachian State University, Boone, NC 28608-2106

[8] University of Alabama at Birmingham, Birmingham, AL, USA

[9]University of Maryland, College Park, MD

[10] Department of Climate and Space Sciences and Engineering, University of Michigan, Ann Arbor, MI 48109, USA

Email: ctejeta@gmail.com

ABSTRACT

Comet C/2017 K2 (Pan-STARRS) provided a rare opportunity to investigate the evolution of coma composition and outgassing patterns over a transitional heliocentric distance range where activity drivers in comets are thought to change from hypervolatile dominated to H_2O dominated. We performed high-resolution ($\lambda/\Delta\lambda$ > 25,000), cross-dispersed, near-infrared spectroscopy of C/2017 K2 with iSHELL at the NASA Infrared Telescope Facility (IRTF) and NIRSPEC at the W. M. Keck 2 observatory. We report gas rotational temperatures (T_{rot}) and molecular production rates (Q; mol/s) or upper limits of hypervolatile species such as CO and CH_4, and other parent volatiles such as C_2H_6, CH_3OH, H_2O, HCN, C_2H_2, NH_3, OCS, CN, and OH^* (a proxy for H_2O production) in long-period comet C/2017 K2 (Pan-STARRS) over a range of heliocentric distance 3.15-2.35 AU during its pre-perihelion passage. We also report mixing ratios (or stringent upper limits) of the targeted species with respect to CO, C_2H_6, and (when it was active) H_2O. All volatiles were found to be enriched relative to water in C/2017 K2 when compared to their mean values from Oort Cloud comets, though abundances relative to C_2H_6 were consistent with their average values from other long-period comets.

Keywords: Comets, Comae, Infrared

1. INTRODUCTION

Because of their ~ 4.5 Gyr residence in the far-out, cold Oort cloud region, returning long-period comets are thought to be least affected by solar radiation, making them the most primitive small icy bodies in the solar system. They are, therefore, used to constrain conditions present in the protoplanetary disk when (and where) they formed and, thus, the subsequent evolution of the early solar system (Dello Russo et al., 2016). Although coma volatile abundances provide an excellent proxy for bulk nucleus abundance when comets are close to the Sun, more distant comets may be affected by preferential outgassing of hypervolatiles.

The critical region for this transition is thought to be between ~2.5 -3 AU (e.g., Ootsubo et al., 2012). Thus, to more accurately determine the volatile abundances of comets for comparison to protoplanetary disk models, it is crucial to understand when comets are fully activated. Our observations addressed this critical question by observing comet C/2017 K2 as it traversed an important diagnostic range of heliocentric distances (3.15 AU - 2.35 AU) while inbound to perihelion.

For comets such as C/2017 K2 observed to be active outside of the region where H_2O ice can sublimate ($R_h \geq 3$ AU), the possible drivers of activity include hypervolatile ices such as CO and CO_2 (A'Hearn et al., 2012; Ootsubo et al., 2012) or exothermic crystallization of amorphous H_2O ice (e.g., Guilbert-Lepoutre, 2012; Jewitt, 2009; Prialnik and Bar-Nun, 1992). For comets that have been observed to be active at large distances post-perihelion, heat acquired near perihelion could be slowly transferred into the interior of the nucleus through conduction. This could cause subsurface volatiles to activate later and fuel distant outbursts (e.g., Prialnik, 1992).

Comet C/2017 K2 (hereafter K2) is a long-period comet detected by the Panoramic Survey Telescope and Rapid Response System (Pan-STARRS) at Haleakala, Hawai'i, on UT 2017 May 21, when it was on its pre-perihelion path at R_h = 15.9 AU from the Sun (Wainscoat et al., 2017). Analysis of prediscovery archival data later showed that K2 was active even at R_h = 23.7 AU from the Sun (Hui et al., 2018; Jewitt et al., 2017; Meech et al., 2017). As this was well beyond the distance at which water crystallization should occur, the activity was likely due to the sublimation of hypervolatile ices (Jewitt et al., 2017; Meech et al., 2017). This is supported by the detection of CO in K2 at R_h = 6.72 AU (Yang et al., 2021). Atomic oxygen emission at 2.80 AU also suggests significant CO_2-driven activity (Cambianica et al., 2023).

In this paper, we report high-resolution, near-infrared spectroscopic observations of K2 to characterize its volatile composition, organized as follows. We discuss observations of K2 in section 2; in section 3, we present data reduction and analysis; in section 4, we discuss our results. In section 5, we present our detailed discussion, and in section 6, we present a summary of our observation results.

2. OBSERVATIONS

Observations of K2 were carried out from UT 2022 May 08-Aug 21, covering a heliocentric distance (R_h) range of ~3.15 – 2.35 AU during its pre-perihelion passage. The observations were performed using both the iSHELL instrument (Rayner et al., 2022) at the NASA Infrared Telescope Facility (IRTF) and the NIRSPEC instrument at the keck II telescope (Martin et al., 2018, 2016) to sample mainly the volatile species CO, CH_4, and C_2H_6 and to test whether H_2O was fully activated in K2 at these ranges of R_h. The observations were acquired using the 0.75″ wide and 15″ long slit for iSHELL and 0.43″ wide and 24″ long slit for NIRSPEC, resulting in a resolving power ($\lambda/\Delta\lambda$) of $\sim 4.2 \times 10^4$ and ~ 25,000, respectively. The comet frames were obtained using a sequence of A-B-B+A exposures with the beams A and B placed equidistant from the center of the slit and separated by half of the slit length (e.g., Bonev et al., 2021; DiSanti et al., 2006). We acquired the spectra using three different iSHELL settings: Lp1 to sample C_2H_6, CH_4, CH_3OH, and OH^*, M2 to sample CO, OCS, and H_2O, and a custom L-setting to sample H_2O, HCN, C_2H_2, and NH_3. The NIRSPEC observations were performed using the KL1 setting to sample H_2O, C_2H_6, and CH_3OH and the KL2 setting to sample H_2O, HCN, C_2H_6, and CH_4. Table 1 shows the observing log for K2. The hypervolatiles CO and CH_4 require sufficiently large geocentric velocities (dΔ/dt) to separate cometary CO and CH_4 emission lines from their strong terrestrial counterpart absorptions. The dΔ/dt of ~14 km s^{-1} and higher during our observations (see Table 1) enabled measuring these molecular species.

Table 1. The iSHELL* and NIRSPEC observing Log for K2

Setting[a]	Target	UT time	T_{int} (minutes)	Slit PA (°)
	2022 May 18, R_h=3.15 AU, Δ = 2.44 AU, dΔ/dt = -34.73 km s^{-1}			
Lp1	BS 6117	11:16-11:28	-	-
M2	BS 6117	11:32-11:42	-	-
M2	K2	11:52-13:20	80	236
Lp1	K2	13:29-15:00	80	236
	2022 June 08, R_h=2.97 AU, Δ = 2.08 AU, dΔ/dt = -25.37 km s^{-1}			
Lp1	BS 5867	08:47-08:55	-	-
M2	BS 5867	09:03-09:13	-	-
M2	K2	09:23-11:27	96	207
Lp1	K2	11:36-12:57	72	207
	2022 June 18, R_h=2.88 AU, Δ = 1.95 AU, dΔ/dt = -18.95 km s^{-1}			
Lp1	BS 5867	08:18-08:27	-	-
M2	BS 5867	08:35-08:47	-	-
M2	K2	08:57-10:47	84	183
Lp1	K2	10:55-12:25	80	183
	2022 July 28, R_h = 2.54 AU, Δ = 1.85 AU, dΔ/dt = +9.06 km s^{-1}			
KL1	K2	06:38-08:03	56	-
KL1	BS6175		-	-
KL2	K2	08:04-09:29	60	-
KL2	BS7950		-	-
	2022 Aug 4, R_h = 2.48 AU, Δ = 1.89 AU, dΔ/dt = +12.33 km s^{-1}			
KL2	K2	08:04-08:49	-	-
	2022 Aug 10, R_h=2.43 AU, Δ = 1.93 AU, dΔ/dt = 14.24 km s^{-1}			
Lp1	K2	05:07-06:35	64	102
M2	K2	06:46-08:45	90	102
M2	BS 7236	08:58-09:07	-	-
Lp1	BS 7236	09:09-09:17	-	-
	2022 Aug 19, R_h=2.36 AU, Δ = 2.01 AU, dΔ/dt = 16.57 km s^{-1}			
Lp1	K2	05:11-07:26	120	101
Lp1	BS 7236	07:36-07:47	-	-
	2022 Aug 20, R_h=2.35 AU, Δ = 2.02 AU, dΔ/dt = 16.76 km s^{-1}			
Lcustom	K2	05:09-07:28	116	101
Lcustom	BS 7236	07:39-07:50	-	-
	2022 Aug 21, R_h=2.35 AU, Δ = 2.03 AU, dΔ/dt = 16.92 km s^{-1}			
M2	K2	05:04-07:32	106	101
M2	BS 7236	07:42-07:54	-	-

Notes: R_h, Δ, and dΔ/dt are the heliocentric distance, geocentric distance, and geocentric velocity of K2 at the time of the observation, respectively, and T_{int} is the total on-source integration time. The slit position angle (PA) was oriented along the projected Sun-comet line on all dates.

[a] iSHELL and NIRSPEC spectral setting used to sample molecular lines.

* Program ID & PI: 2022A055 [Investigation of CO vs. H_2O driven outgassing in comet C/2017 K2 (PanSTARRS)], 2022B089 [Compositional measurements as comet C/2017 K2 (PanSTARRS) transitions from hypervolatile to water-dominated activity]; Ejeta

3. DATA REDUCTION AND ANALYSES

We followed a data reduction procedure tailored to iSHELL and NIRSPEC spectra (e.g., Bonev et al., 2021, 2023; Dello Russo et al., 2020; DiSanti et al., 2021, 2017). The iSHELL echelle orders were flat-fielded, dark subtracted, cleaned for cosmic ray hits, and spectrally and spatially straightened such that each row corresponded to a unique position along the slit and each column to a unique wavelength. Comet spectra were extracted from the processed orders by summing over 15 rows, seven rows to each side of the nucleus, defined as the peak of emission lines in each order. Contributions from continuum and gaseous emissions (shown in Fig. 1) were determined as outlined in DiSanti et al. (2017) Bonev et al. (2023). Telluric burdens were retrieved using the NASA Planetary Spectrum Generator (Villanueva et al., 2018) using IR standard star spectra acquired for each instrument setting with the widest slit (4″ for ishell and 0.72″ for NIRSPEC) and then applied to the comet spectra. The fully resolved transmittance function was convolved to the resolving power of the comet data ($\sim 4.2 \times 10^4$) and scaled to the level of the comet continuum. The cometary emission lines were isolated by subtracting the modeled continuum.

Finally, each modeled g-factor (line intensity) is corrected for the monochromatic atmospheric transmittance at its Doppler-shifted wavelength based on the geocentric velocity of the comet at the time of the observation. Synthetic models of fluorescent emission for each targeted species were then compared to the observed line intensities. The g-factors used in this study were generated with quantum mechanical models developed for H_2O (Villanueva et al., 2012b), OH^* Bonev and Mumma (2006), HCN and NH_3 (Villanueva et al., 2013), C_2H_2 [(Villanueva et al., 2011b), see appendix C], C_2H_6 (Villanueva et al., 2011b), CH_3OH (DiSanti et al., 2013; Villanueva et al., 2012a), CH_4 (Gibb et al., 2003), and CO (DiSanti et al., 2001).

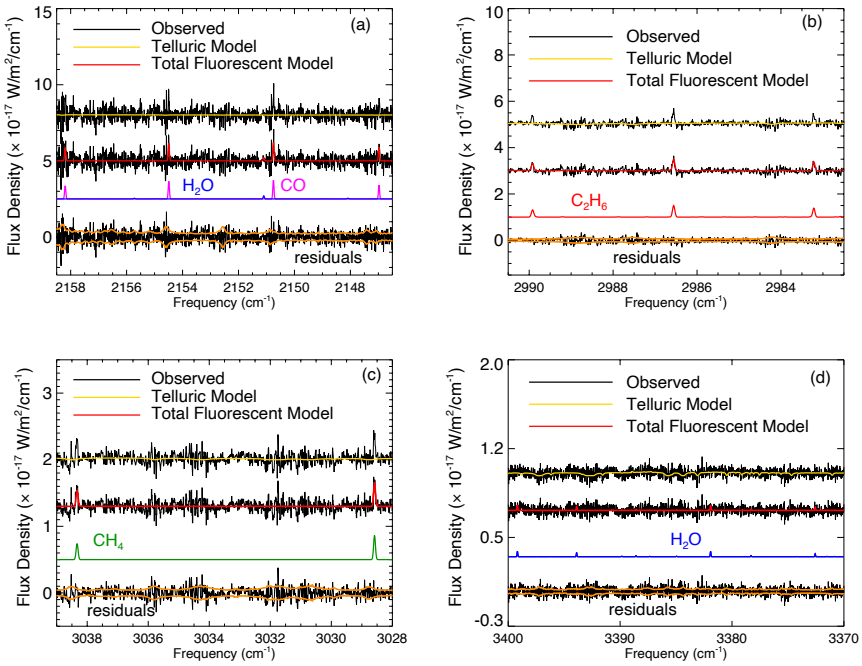

Figure 1. Sample spectra and best-fit fluorescent models of molecular emissions in comet C/2017 K2. Panel (a) is for observation on 2022 August 10 (a), panels (b) and (c) are for observations on August 19, and panel (d) is for August 20. The observed spectra (black) are superimposed with the telluric model (yellow). Individual fluorescence emission models (color-coded by species) are shown below the observed spectrum in each panel. The bottom trace indicates the residual spectrum (after subtracting the modeled continuum and total molecular contributions), with the superimposed ±1 σ stochastic noise envelope shown in orange.

3.1. DETERMINATION OF ROTATIONAL TEMPERATURE

The excitation condition in the cometary coma can be quantified by the rotational temperature (T_{rot}). The technique of obtaining T_{rot} involves analysis of a graph of F_{line}/g vs. rotational energies of the upper states (E_u), where F_{line} is the transmittance corrected molecular line flux, and g is the fluorescence efficiency (or the g-factors) of the ro-vibrational lines. At the optimum T_{rot}, the quantity F_{line}/g is constant for all E_u, and this T_{rot} value corresponds to the zero slopes of the best fit of the graph of F_{line}/g vs. E_u (Dello Russo et al., 2004; DiSanti et al., 2006).

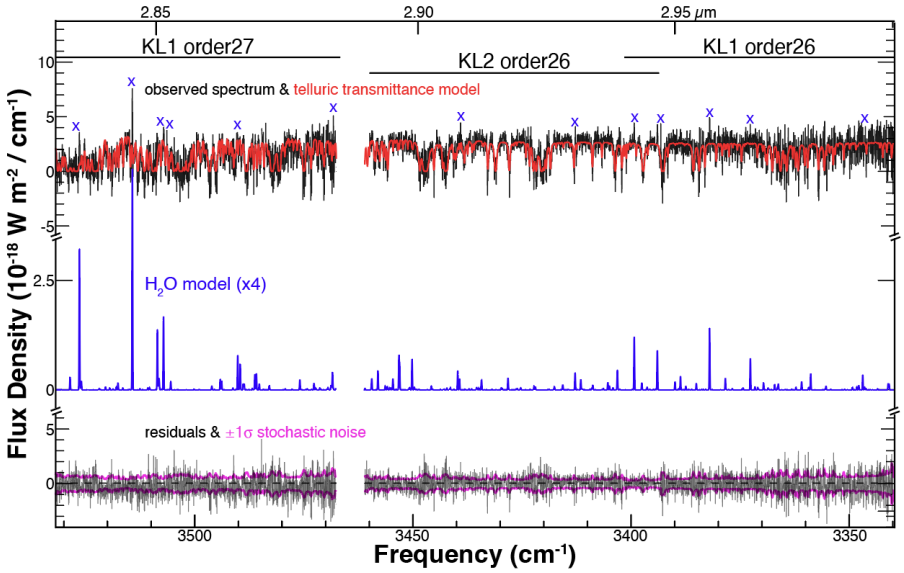

Figure 2. A composite spectra of H_2O in K2 acquired using the NIRSPEC. The spectra were acquired using KL1 and KL2 settings on UT on 28 July 2022 with ~ 55 minutes on source.

For each date of our observations, we obtained consistent rotational temperatures for all species with sufficient signal-to-noise ratio (SNR) (see Table 2 below). When the SNR for a given species was insufficient, we assumed a T_{rot} determined from species measured on the same night. This assumption is reasonable given that T_{rot} obtained from contemporaneously measured volatile species (both within the setting and across the settings) are genearally found to be consistent (e.g., Gibb et al., 2012), and that thermodynamic models for the inner collisional coma also show roughly the same effective temperature for all species observed within a given field of view (Combi et al., 2004; Fougere et al., 2012).

3.2. MOLECULAR PRODUCTION RATES and MIXING RATIOS

The nucleus-centered molecular production rate, Q_{nc} (molecules s^{-1}), is given as (DiSanti et al., 2014):

$$Q_{nc} = \frac{4\pi\Delta^2 F_i}{f(x)\tau_1 g_1}, \quad (1)$$

where F_i (Wm^{-2}) is the flux of the i^{th} emission line at the top of the terrestrial atmosphere, g_1 (W $molecule^{-1}$) and τ_1(s) are the fluorescence efficiency (g-factor) and the photo-dissociation lifetime, respectively at R_h =1 au (both R_h dependent through the relations $g = g_1 R_h^{-2}$ and $\tau = \tau_1 R_h^2$, where the subscript **1** indicates R_h= 1 au), f(x) is the fraction of molecules of the species contained in the beam at each position, assuming entirely native release (nucleus release), and Δ (m) is the geocentric distance. The technique of obtaining the nucleus-centered production rate is based on the Q-curve analysis (e.g., Bonev, 2005). The production rates at different positions along the slit were computed assuming uniform symmetric outflow and were symmetrized by averaging the production rates at diametrically opposite positions about the center along the slit to account for axi-symmetric outflow (Villanueva et al., 2011a). The weighted mean of these symmetrized production rates gives the terminal (total) production rate, Q_{term}. The increase of production rate from the nucleus-centered position (Q_{nc}) to a terminal (off-nucleus) value (Q_{term}) establishes a quantity called a growth factor ($GF = Q_{nc}/Q_{nc}$) which accounts for the flux loss (or slit losses). Generally, the same atmospheric seeing conditions will affect molecules measured within the same instrument setting (Villanueva et al., 2011a). Thus, when low SNR precluded determining a reliable GF, we assumed a value determined from a simultaneously or contemporaneously measured species. The total production rates obtained for each molecular species are indicated in Table 2.

The chemical taxonomy of comets is established based on the chemical abundance of molecular species, which is quantified using the mixing ratio (Bonev, 2005), typically given as the ratio of the production rate of a given molecule to that of simultaneously or contemporaneously measured H_2O [i.e., Q_X/Q_{H_2O}], usually the most abundant species in a cometary coma. We also calculated mixing ratios with respect to simultaneously or contemporaneously measured CO or C_2H_6 since H_2O was not always detected (Table 2).

Table 2. Volatile measurements in comet K2 obtained using iSHELL and NIRSPEC

Setting	**Molecule**	$\mathbf{T}_{rot}^{(a)}$ (K)	$\mathbf{GF}^{(b)}$	$\mathbf{Q}^{(c)}$ (10^{26} molecules s^{-1})
	2022 May 18, R_h = 3.15 AU, Δ = 2.44 AU, dΔ/dt = -34.73 km s^{-1}			
M2	CO	18^{+6}_{-4}	2.40 ± 0.20	33.4 ± 5.1
		(20)	2.40 ± 0.20	34.1 ± 5.1
	H_2O	(18)	(2.40)	< 438
		(20)	(2.40)	< 463
Lp1	C_2H_6	20^{+7}_{-4}	(2.52)	4.25 ± 0.58
		(18)	(2.52)	4.13 ± 0.57
	CH_4	(20)	2.52 ± 0.14	7.10 ± 1.01
		(18)	2.52	6.72 ± 1.10
	2022 June 08, R_h = 2.97 AU, Δ = 2.08 AU, dΔ/dt = -25.37 km s^{-1}			
M2	CO	24^{+7}_{-5}	2.09 ± 0.10	31.7 ± 2.8
		(28)	2.09 ± 0.10	33.4 ± 3.1
	H_2O	(24)	(2.09)	< 231
		(28)	(2.09)	< 246
Lp1	C_2H_6	(28)	(2.09)	3.01 ± 0.38
		(24)	(2.09)	2.85 ± 0.37

Continued on next page

Table 2. Volatile Measurements in Comet K2 obtained using iSHELL and NIRSPEC (cont.)

Setting	**Molecule**	$\mathbf{T}_{rot}^{(a)}$ (K)	**GF**$^{(b)}$	**Q**$^{(c)}$ (10^{26} molecules s^{-1})
	CH_4	28^{+4}_{-3}	(2.09)	8.49 ± 0.39
		(24)	(2.09)	7.59 ± 0.46
	2022 June 18, R_h = 2.88 AU, Δ = 1.95 AU, dΔ/dt = -18.95 km s^{-1}			
M2	CO	34^{+9}_{-7}	2.54 ± 0.15	40.4 ± 8.5
		(32)	2.54 ± 0.15	39.8 ± 8.4
	H_2O	(34)	(2.54)	< 336
		(32)	(2.54)	< 334
Lp1	C_2H_6	32^{+5}_{-4}	2.16 ± 0.21	4.49 ± 0.61
		(34)	2.16 ± 0.21	4.56 ± 0.62
	CH_4	(32)	2.12 ± 0.21	8.48 ± 1.17
		(34)	2.12 ± 0.21	9.06 ± 1.25
	2022 July 28, R_h = 2.54 AU, Δ = 1.85 AU, dΔ/dt = +9.06 km s^{-1}			
KL1	H_2O	31^{+9}_{-5}	1.78 ± 0.18	122 ± 15
	C_2H_6	44^{+3}_{-2}	1.76 ± 0.12	4.08 ± 0.28
	CH_3OH	40^{+10}_{-8}	1.64 ± 0.32	9.03 ± 1.88
KL2	H_2O	(31)	1.79 ± 0.27	119 ± 22
	HCN	33^{+7}_{-5}	1.80 ± 0.18	0.83 ± 0.10
	C_2H_6	(44)	1.74 ± 0.37	4.22 ± 0.97
	2022 Aug 4, R_h = 2.48 AU, Δ = 1.89 AU, dΔ/dt = +12.33 km s^{-1}			
KL2	H_2O	(50)	1.73 ± 0.22	173 ± 35
	CH_4	(50)	1.77 ± 0.20	15.6 ± 3.2
	2022 Aug 10, R_h = 2.43 AU, Δ = 1.93 AU, dΔ/dt = 14.24 km s^{-1}			
M2	CO	49^{+12}_{-10}	(1.93)	40.9 ± 8.3

Continued on next page

Table 2. Volatile Measurements in Comet K2 obtained using iSHELL and NIRSPEC (cont.)

Setting	**Molecule**	$\mathbf{T}_{rot}^{(a)}$ (K)	$\mathbf{GF}^{(b)}$	$\mathbf{Q}^{(c)}$ (10^{26} molecules s^{-1})
	H_2O	(49)	(1.93)	< 243
Lp1	C_2H_6	(49)	1.93 ± 0.12	5.09 ± 0.49
	CH_4	(49)	(1.93)	12.2 ± 3.1
	OH^*	(49)	(1.93)	< 454
	CH_3OH	(49)	(1.93)	15.7 ± 2.3
	2022 Aug 19, R_h = 2.36 AU, Δ = 2.01 AU, dΔ/dt = 16.57 km s^{-1}			
Lp1	C_2H_6	52^{+7}_{-6}	2.18 ± 0.23	5.25 ± 0.67
	CH_4	(52)	2.14 ± 0.13	15.7 ± 2.3
	CH_3OH	(52)	(2.18)	17.1 ± 1.9
	OH^*	(52)	(2.18)	< 323
	2022 Aug 20, R_h = 2.35 AU, Δ = 2.02 AU, dΔ/dt = 16.76 km s^{-1}			
L-custom	H_2O	(53)	2.44 ± 0.26	365 ± 66
	HCN	(53)	(2.44)	1.75 ± 0.16
	C_2H_2	(53)	(2.44)	1.97 ± 0.34
	NH_3	(53)	(2.44)	< 6.24
	2022 Aug 21, R_h = 2.35 AU, Δ = 2.03 AU, dΔ/dt = 16.92 km s^{-1}			
M2	CO	53^{+5}_{-4}	2.65 ± 0.15	63.7 ± 4.0
	H_2O	(53)	(2.65)	< 300
	CN	(53)	(2.65)	< 2.58
	OCS	(53)	(2.65)	<1.2

Notes: [a] Rotational temperature. Values in parentheses are assumed.

[b] Growth factor. Values in the parentheses are assumed.

[c] Global production rate. Production rate uncertainty includes line-by-line deviation between the modeled and observed intensities and photon noise (e.g., Bonev et al., 2007; Dello Russo et al., 2004).

Table 3. Volatile abundances in comet K2

Molecule	$\mathbf{R}_h$ (AU)	$\mathbf{T}_{rot}$ (K)	$\frac{Q_X}{Q_{CO}}$ [d] (%)	$\frac{Q_X}{Q_{C_2H_6}}$ [e]	$\frac{Q_X}{Q_{H_2O}}$ [f] (%)
CO	3.15	18	100	8.10 ± 1.67	> 7.62
		(20)	100	8.08 ± 1.65	> 7.37
H_2O	3.15	(18)	<1313	<106	
		(20)	< 1357	<109	
C_2H_6	3.15	20	12.5 ± 2.5	1.00	> 0.92
		(18)	12.4 ± 2.5	1.00	> 0.94
CH_4	3.15	(20)	20.8 ± 4.3	1.68 ± 0.32	>1.53
		(18)	20.1 ± 4.5	1.63 ± 0.34	> 1.53
CO	2.97	24	100	11.1 ± 1.8	> 13.8
		(28)	100	11.1 ± 1.7	> 13.6
H_2O	2.97	(24)	< 727	< 81.1	
		(28)	< 735	< 81.5	
C_2H_6	2.97	(28)	9.02 ± 1.41	1.00	> 1.23
		(24)	8.97 ± 1.43	1.00	> 1.23
CH_4	2.97	28	25.4 ± 2.6	2.82 ± 0.37	> 3.46
		(24)	23.9 ± 2.6	2.67 ± 0.38	> 3.29
CO	2.88	34	100	8.86 ± 2.22	>12
		(32)	100	8.87 ± 2.22	>11.9
H_2O	2.88	(34)	< 831	< 73.6	
		(32)	< 839	< 74.4	
C_2H_6	2.88	32	11.3 ± 2.8	1.00	> 1.34
		(34)	11.3 ± 2.8	1.00	> 1.36

Continued on next page

Table 3. Volatile Abundances in Comet K2 (cont.)

Molecule	$\mathbf{R}_h$ (AU)	$\mathbf{T}_{rot}$ (K)	$\frac{Q_X}{Q_{CO}}^{(d)}$ (%)	$\frac{Q_X}{Q_{C_2H_6}}^{(e)}$	$\frac{Q_X}{Q_{H_2O}}^{(f)}$ (%)
CH_4	2.88	(32)	21.3 ± 5.4	1.89 ± 0.36	> 2.54
		(34)	22.4 ± 5.7	1.99 ± 0.38	> 2.70
H_2O	2.54	31	299 ±71	29.9 ± 4.3	100
C_2H_6	2.54	44	9.98 ± 2.14	1.00	3.34 ± 0.48
CH_3OH	2.54	40	22.1 ± 6.43	2.21 ± 0.49	7.40 ± 1.80
H_2O	2.54	(31)	291 ± 81	28.1 ± 8.4	100
HCN	2.54	33	2.02 ± 0.48	0.20 ± 0.05	0.70 ± 0.16
C_2H_6	2.54	(44)	10.3 ± 3.2	1.00	3.56 ± 1.06
H_2O	2.48	(50)	424 ± 122	41.0 ± 12.6	100
CH_4	2.48	(50)	38.3 ± 11.1	3.70 ±1.15	9.03 ± 2.63
CO	2.43	49	100	8.02 ± 1.80	> 16.8
H_2O	2.43	(49)	< 596	< 47.7	
C_2H_6	2.43	(49)	12.47 ± 2.80	1.00	> 1.04
CH_4	2.43	(49)	29.9 ± 9.6	2.40 ± 0.64	> 5.02
OH^*	2.43	(49)	< 1111	< 89.1	
CH_3OH	2.43	(49)	38.3 ± 9.6	3.07 ± 0.57	> 6.43
C_2H_6	2.36	52	8.24 ± 1.25	1.00	1.44 ± 0.32
CH_4	2.36	(52)	24.6 ± 4.1	2.98 ± 0.55	4.29 ± 1.0
CH_3OH	2.36	(52)	26.9 ± 3.7	3.27 ± 0.52	4.69 ± 1.0
OH^*	2.36	(52)	< 507	< 61.5	> 16.2
H_2O	2.35	(53)	573 ± 114	69.6 ± 15.4	100
HCN	2.35	(53)	2.77 ± 0.34	0.34 ± 0.05	0.48 ± 0.10
C_2H_2	2.35	(53)	3.09 ± 0.59	0.38 ± 0.08	0.54 ± 0.13

Continued on next page

Table 3. Volatile Abundances in Comet K2 (cont.)

Molecule	$\mathbf{R}_h$ (AU)	$\mathbf{T}_{rot}$ (K)	$\frac{Q_X}{Q_{CO}}^{(d)}$ (%)	$\frac{Q_X}{Q_{C_2H_6}}^{(e)}$	$\frac{Q_X}{Q_{H_2O}}^{(f)}$ (%)
NH_3	2.35	(53)	< 9.79	< 1.19	< 1.71
CO	2.35	53	100	12.1 ± 1.9	17.5 ± 3.5
H_2O	2.35	(53)	< 471	< 57.2	
CN	2.35	(53)	< 4.06	< 0.49	< 0.71
OCS	2.35	(53)	< 1.84	< 0.22	< 0.32

Notes:

[d] Molecular abundance with respect to CO. *For Aug 19 and 20, Q(CO) from Aug 21 was assumed; for July 28 and July 4, Q(CO) from Aug 10 was assumed*

[e] Molecular abundance with respect to C_2H_6. *For Aug 20 and 21, Q(C_2H_6) from Aug 19 was assumed; for July 4, Q(C_2H_6) from July 28 was assumed*

[f] Molecular abundance with respect to H_2O. *For Aug 19 and 21, Q(H_2O) from Aug 20 was assumed*

4. DISCUSSION

4.1. CHANGE OF PRODUCTION RATES WITH HELIOCENTRIC DISTANCES IN COMET K2

We investigated volatile activity in comet K2 between R_h = 3.15 AU and 2.35 AU inbound from the Sun. The comet activity was relatively consistent beyond ~ 2.5 AU (within uncertainty) but showed an increase within that (see Fig. 3). While only CO, CH_4, and C_2H_6 were detected beyond 2.5 AU, K2 was sufficiently bright and active within that to also detect H_2O, HCN, C_2H_2, and CH_3OH. The H_2O production rate increases more steeply than other molecules near ~ 2.3 AU. The increase in production at a smaller heliocentric distance is generally expected as the comet's activity increases typically with decreasing R_h.

We compared the molecular abundances measured with respect to H_2O as well as C_2H_6 (see Table 3) to other OCCs (Figs. 4, 5). When compared to water, the abundances of all volatile species are significantly higher than their mean values from OCCs measured to date at NIR wavelengths within ~ 2.0 AU, with the enhancements being very strong for the hypervolatile molecules CO and CH_4.

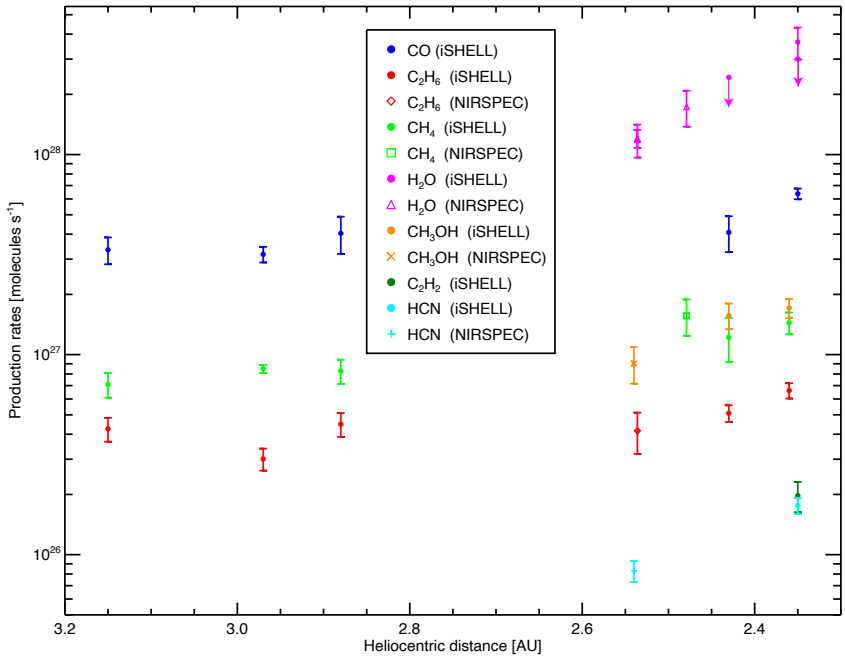

Figure 3. Molecular production rates of detected molecular species in comet C/2017 K2 (Pan-STARRS) as a function of heliocentric distances of observations.

On the other hand, the abundances of these volatile species relative to C_2H_6 are within the range of values from OCCs measured to date within ~ 2 AU (see Fig. 3). Thus, the enhanced abundances of volatile species with respect to H_2O might imply that either H_2O was fully activating as the comet approached ~ 2.0 AU or that the comet K2 is unusually enriched in these volatiles, as was the case for comet C/2001 A2 (Gibb et al., 2007; Magee-Sauer et al., 2008).

4.2. VOLATILE ABUNDANCES IN COMET K2

To put K2 in context, we compared its volatile abundance measurements to those of other comets (see Fig. 6).

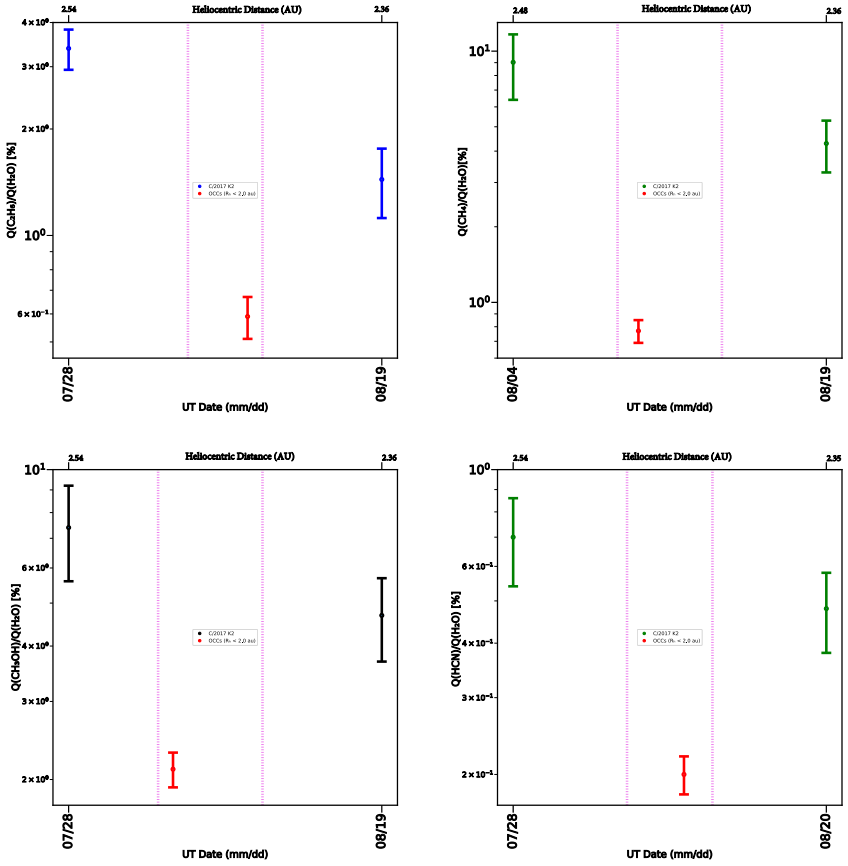

Figure 4. Comparison of volatile abundances of species in comet C/2017 K2 (Pan-STARRS) relative to simultaneously (contemporaneously) measured H_2O with their average values in OCCs measured within ~2 AU. The average abundances in OCCs are from Dello Russo et al. (2016) and from comets observed after that: C/2020 S3 (Ejeta et al., 2024), E4 C/2017 E4 (Faggi et al., 2018), V5 C/2013 V5 (DiSanti et al., 2018), C/2021 A1 (Faggi et al., 2023; Lippi et al., 2023), C/2002 T7 and C/2015 ER61 (Saki et al., 2021), C/2018 Y1 (DiSanti et al., 2021), C/2014 Q2 (Dello Russo et al., 2022), and C/2012 K1 (Roth et al., 2017).

While the CH_4 abundance relative to CO in K2 remained roughly consistent over the heliocentric distance covered, it is significantly higher than for comets C/2006 W3 (Christensen) and C/2016 R2 (Pan-STARRS) at about similar R_h (Bockelée-Morvan et al., 2010; Bonev et al., 2017; McKay et al., 2019; Wierzchos and Womack, 2018).

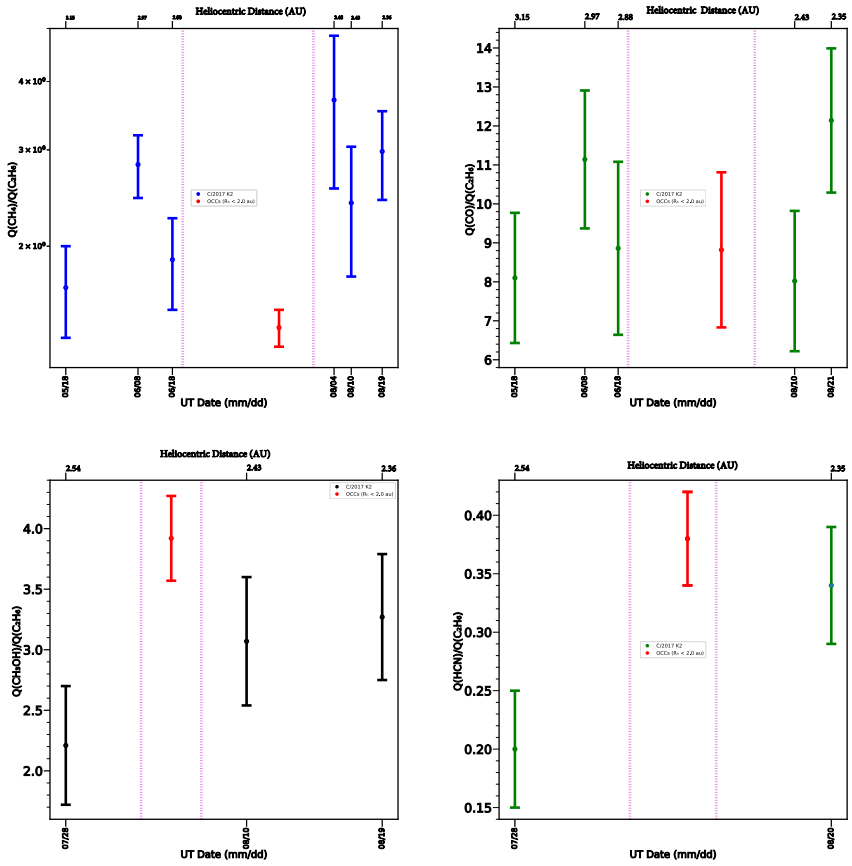

Figure 5. Abundances of CH_4, CO, CH_3OH, and HCN in comet C/2017 K2 (Pan-STARRS) relative to simultaneously (contemporaneously) measured C_2H_6 . The abundance of each molecule relative to C_2H_6 in OCCs measured to date in the Infrared within $\sim$ 2.0 au are shown (in red) for comparison.

In addition, the CO abundance relative to C_2H_6 in K2 is lower than that for comets C/1995 O1 (Hale-Bopp) and C/2006 W3 (see Bockelée-Morvan et al., 2010; Bonev et al., 2017; Dello Russo et al., 2001; DiSanti et al., 2001). This is due to these comets being significantly CO-rich compared to K2. Yang et al. (2021) measured a 3.6 σ CO detection at R_h = 6.72 AU in comet K2. They attributed the low production rate of K2 compared to Hale-Bopp at a similar heliocentric distance to K2 being dusty (dust/gas ratio > 1) and smaller on size.

Using imaging observations, Jewitt et al. (2017) determined an upper limit for the size of the radius of the nucleus of K2 to ≤ 9 km, which is roughly a fifth of the size of the radius of Hale-Bopp. Even though the nucleus radius size of C/2016 R2 is unknown, Wierzchos and Womack (2018) suggested that its radius is ≤ ~ 15 km if its CO production rate is proportional to the surface area of its nucleus. Thus, even though there were no accurate measurements of the sizes of the nuclei of comets C/2006 W3 and C/2016 R2, it is possible that the significantly lower CO production rates we measured for comet K2 compared to those measured for these comets at about similar Rh could be due to, among other factors, the dusty nature of K2 and its smaller in size compared to these comets. On the other hand, Ootsubo et al. (2012) observed different comets over a range of R_h = 2.43 AU - 3.29 AU and measured only 3 σ upper limits for the CO production rates. This indicates that apart from the R_h, the overall production rates strongly depend on the nucleus radius size of a comet, an active fraction of surface area, and the dust-to-gas ratio. As such, differences in production rates among comets observed at similar heliocentric distances could be due to any combination of these factors.

Measurements of hypervolatiles CH_4 and CO relative to C_2H_6 from OCCs measured to date in the infrared wavelength region are shown in Fig. 6 for comparison. It can be noted that the ratio of CH_4 relative to C_2H_6 in comet K2 is generally consistent with some OCCs observed within ~3.5 AU. In addition, the ratio of CO relative to C_2H_6 is consistent with some OCCs measured within 2.0 AU. On the other hand, Ootsubo et al. (2012) observed comets C/2006 OF2, C/2006 Q1, C/2007 Q3, and C/2007 N3 during multiple nights over R_h ~ 2.4-3.6 AU and measured only a 3-σ upper limits (ranging 1-10 %) for CO abundance (relative to H_2O) for all of these comets. Thus, more measurements of CO and C_2H_6 beyond ~2.0 AU are required to draw any conclusion.

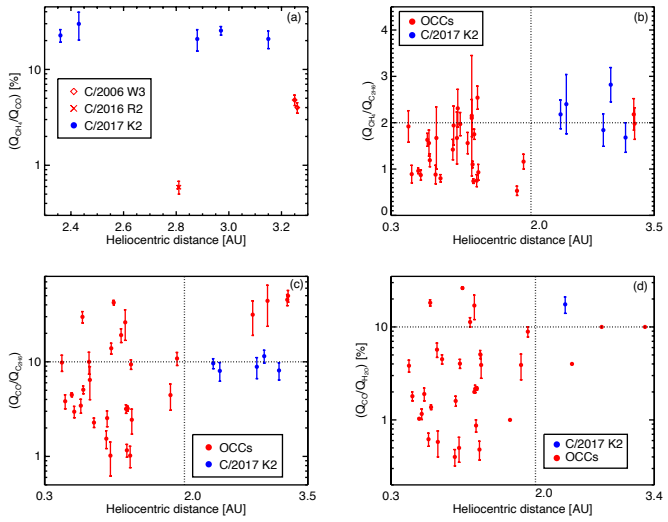

Figure 6. Abundance of volatile species in comet C/2017 K2 (Pan-STARRS) relative to simultaneously measured CO and C_2H_6. Panels (a) and (b) indicate abundance of CH_4 relative to CO and C_2H_6, and panels (c) and (d) indicate abundance CO relative to C_2H_6 and H_2O, respectively. The abundances of OCCs measured in the infrared wavelength (in red) are also shown for comparison.

5. SUMMARY

We obtained pre-perihelion observations of K2 covering a heliocentric distance range of R_h ~ 3.15 -2.35 AU to sample the volatile composition and to test the activation of H_2O and other volatile species (C_2H_2, NH_3, HCN, CH_3OH, CN, and OCS). Our main results are summarized below:

Abundances of volatile species with respect simultaneously or contemporaneously H_2O in K2 were significantly higher than the average values from OCCs measured to date within 2.0 AU. On the other hand, the abundances of these volatiles relative to C_2H_6 are generally consistent with their mean values from OCCs. This might imply that comet K2 is either enriched in these volatiles (depleted in water) or that the H_2O was not yet fully activated as the comet approached 2.0 AU. This necessitates that perhaps observations of comets at the critical heliocentric distance region of ~ 2-2.50 AU to conclusively decide the full activation of H_2O.

ACKNOWLEDGEMENTS

Data for this study were obtained at the NASA Infrared Telescope Facility (IRTF), operated by the University of Hawai'i under contract NNH14CK55B with NASA. Some of the data presented herein were obtained at W.M. Keck Observatory, operated as a scientific partnership among the California Institute of Technology, the University of California, and NASA. The Observatory was made possible by the generous financial support of the W. M. Keck Foundation. The authors gratefully acknowledge the support of the IRTF and Keck 2 staff for their help in acquiring the K2 data. E.G. and C.E. acknowledge support from NSF under award 2009910.

REFERENCES

A'Hearn, M. F., Feaga, L. M., Keller, H. U., Kawakita, H., Hampton, D. L., Kissel, J., Klaasen, K. P., McFadden, L. A., Meech, K. J., Schultz, P. H., Sunshine, J. M., Thomas, P. C., Veverka, J., Yeomans, D. K., Besse, S., Bodewits, D., Farnham, T. L., Groussin, O., Kelley, M. S., Lisse, C. M., Merlin, F., Protopapa, S., and Wellnitz, D. D. (2012). Cometary Volatiles and the Origin of Comets. ApJ, 758(1):29.

Bockelée-Morvan, D., Hartogh, P., Crovisier, J., Vandenbussche, B., Swinyard, B. M., Biver, N., Lis, D. C., Jarchow, C., Moreno, R., Hutsemékers, D., Jehin, E., Küppers, M., Lara, L. M., Lellouch, E., Manfroid, J., de Val-Borro, M., Szutowicz, S., Banaszkiewicz, M., Bensch, F., Blecka, M. I., Emprechtinger, M., Encrenaz, T., Fulton, T., Kidger, M., Rengel, M., Waelkens, C., Bergin, E., Blake, G. A., Blommaert, J. A. D. L., Cernicharo, J., Decin, L., Encrenaz, P., de Graauw, T., Leeks, S., Medvedev, A. S., Naylor, D., Schieder, R., and Thomas, N. (2010). A study of the distant activity of comet C/2006 W3 (Christensen) with Herschel and ground-based radio telescopes. A&A, 518:L149.

Bonev, B. P. (2005). *Towards a Chemical Taxonomy of Comets: Infrared Spectroscopic Methods for Quantitative Measurements of Cometary Water*. PhD thesis, University of Toledo, Ohio.

Bonev, B. P., Dello Russo, N., DiSanti, M. A., Martin, E. C., Doppmann, G., Vervack, Ronald J., J., Villanueva, G. L., Kawakita, H., Gibb, E. L., Combi, M. R., Roth, N. X., Saki, M., McKay, A. J., Cordiner, M. A., Bodewits, D., Crovisier, J., Biver, N., Cochran, A. L., Shou, Y., Khan, Y., and Venkataramani, K. (2021). First Comet Observations with NIRSPEC-2 at Keck: Outgassing Sources of Parent Volatiles and Abundances Based on Alternative Taxonomic Compositional Baselines in 46P/Wirtanen. *Planetary Science Journal*, 2(2):45.

Bonev, B. P., Dello Russo, N., Kawakita, H., Vervack, Ronald J., J., DiSanti, M. A., Shinnaka, Y., Ootsubo, T., Gibb, E. L., Combi, M. R., Altwegg, K., Biver, N., Crovisier, J., Doppmann, G., Villanueva, G. L., Khan, Y., Ejeta, C. T., Saki, M., McKay, A. J., Cochran, A. L., Jehin, E., Roth, N. X., Cordiner, M. A., and Shou, Y. (2023). The Return of the Rosetta Target: Keck Near-infrared Observations of Comet 67P/Churyumov-Gerasimenko in 2021. AJ, 166(6):233.

Bonev, B. P. and Mumma, M. J. (2006). A Comprehensive Study of Infrared OH Prompt Emission in Two Comets. II. Implications for Unimolecular Dissociation of H_2O. ApJ, 653(1):788–791.

Bonev, B. P., Mumma, M. J., Villanueva, G. L., Disanti, M. A., Ellis, R. S., Magee-Sauer, K., and Dello Russo, N. (2007). A Search for Variation in the H_2O Ortho-Para Ratio and Rotational Temperature in the Inner Coma of Comet C/2004 Q2 (Machholz). ApJ, 661(1):L97–L100.

Bonev, B. P., Villanueva, G. L., DiSanti, M. A., Boehnhardt, H., Lippi, M., Gibb, E. L., Paganini, L., and Mumma, M. J. (2017). Beyond 3 au from the Sun: The Hypervolatiles CH_4, C_2H_6, and CO in the Distant Comet C/2006 W3 (Christensen). AJ, 153(5):241.

Cambianica, P., Munaretto, G., Cremonese, G., Podio, L., Codella, C., and Boschin, W. (2023). CO_2 as the main parent source of atomic oxygen in comet C/2017 K2 (Pan-STARRS). A&A, 674:L14.

Combi, M. R., Harris, W. M., and Smyth, W. H. (2004). Gas dynamics and kinetics in the cometary coma: theory and observations. In Festou, M. C., Keller, H. U., and Weaver, H. A., editors, *Comets II*, page 523. University of Arizona Press.

Dello Russo, N., DiSanti, M. A., Magee-Sauer, K., Gibb, E. L., Mumma, M. J., Barber, R. J., and Tennyson, J. (2004). Water production and release in Comet 153P/Ikeya-Zhang (C/2002 C1): accurate rotational temperature retrievals from hot-band lines near 2.9-μm. Icarus, 168(1):186–200.

Dello Russo, N., Kawakita, H., Bonev, B. P., Vervack, R. J., Gibb, E. L., Shinnaka, Y., Roth, N. X., DiSanti, M. A., and McKay, A. J. (2020). Post-perihelion volatile production and release from Jupiter-family comet 45P/Honda-Mrkos-Pajdušáková. Icarus, 335:113411.

Dello Russo, N., Kawakita, H., Vervack, R. J., and Weaver, H. A. (2016). Emerging trends and a comet taxonomy based on the volatile chemistry measured in thirty comets with high-resolution infrared spectroscopy between 1997 and 2013. Icarus, 278:301–332.

Dello Russo, N., Mumma, M. J., DiSanti, M. A., Magee-Sauer, K., and Novak, R. (2001). Ethane Production and Release in Comet C/1995 O1 Hale-Bopp. Icarus, 153(1):162–179.

Dello Russo, N., Vervack, R. J., Kawakita, H., Bonev, B. P., DiSanti, M. A., Gibb, E. L., McKay, A. J., Cochran, A. L., Weaver, H. A., Biver, N., Crovisier, J., Bockelée-Morvan, D., Kobayashi, H., Harris, W. M., Roth, N. X., Saki, M., and Khan, Y. (2022). Volatile Abundances, Extended Coma Sources, and Nucleus Ice Associations in Comet C/2014 Q2 (Lovejoy). *Planetary Science Journal*, 3(1):6.

DiSanti, M. A., Bonev, B. P., Dello Russo, N., McKay, A. J., Roth, N. X., Saki, M., Gibb, E. L., Vervack, Ronald J., J., Khan, Y., and Kawakita, H. (2021). Volatile Composition and Outgassing in C/2018 Y1 (Iwamoto): Extending Limits for High-resolution Infrared Cometary Spectroscopy between 2.8 and 5.0 μm. *Planetary Science Journal*, 2(6):225.

DiSanti, M. A., Bonev, B. P., Gibb, E. L., Roth, N. X., Dello Russo, N., and Vervack, Ronald J., J. (2018). Comet C/2013 V5 (Oukaimeden): Evidence for Depleted Organic Volatiles and Compositional Heterogeneity as Revealed through Infrared Spectroscopy. AJ, 156(6):258.

DiSanti, M. A., Bonev, B. P., Magee-Sauer, K., Dello Russo, N., Mumma, M. J., Reuter, D. C., and Villanueva, G. L. (2006). Detection of Formaldehyde Emission in Comet C/2002 T7 (LINEAR) at Infrared Wavelengths: Line-by-Line Validation of Modeled Fluorescent Intensities. ApJ, 650(1):470–483.

DiSanti, M. A., Bonev, B. P., Russo, N. D., Vervack, Ronald J., J., Gibb, E. L., Roth, N. X., McKay, A. J., Kawakita, H., Feaga, L. M., and Weaver, H. A. (2017). Hypervolatiles in a Jupiter-family Comet: Observations of 45P/Honda-Mrkos-Pajdušáková Using iSHELL at the NASA-IRTF. AJ, 154(6):246.

DiSanti, M. A., Bonev, B. P., Villanueva, G. L., and Mumma, M. J. (2013). Highly Depleted Ethane and Mildly Depleted Methanol in Comet 21P/Giacobini-Zinner: Application of a New Empirical ν_2-band Model for CH_3OH near 50 K. ApJ, 763(1):1.

DiSanti, M. A., Mumma, M. J., Russo, N. D., and Magee-Sauer, K. (2001). Carbon Monoxide Production and Excitation in Comet C/1995 O1 (Hale-Bopp): Isolation of Native and Distributed CO Sources. Icarus, 153(2):361–390.

DiSanti, M. A., Villanueva, G. L., Paganini, L., Bonev, B. P., Keane, J. V., Meech, K. J., and Mumma, M. J. (2014). Pre- and post-perihelion observations of C/2009 P1 (Garradd): Evidence for an oxygen-rich heritage? Icarus, 228:167–180.

Ejeta, C., Gibb, E., Roth, N., DiSanti, M. A., Dello Russo, N., Saki, M., McKay, A. J., Kawakita, H., Khan, Y., Bonev, B. P., Vervack, R. J., and Combi, M. R. (2024). Coma Abundances of Volatiles at Small Heliocentric Distances: Compositional Measurements of Long-period Comet C/2020 S3 (Erasmus). AJ, 167(1):32.

Faggi, S., Lippi, M., Mumma, M. J., and Villanueva, G. L. (2023). Strongly Depleted Methanol and Hypervolatiles in Comet C/2021 A1 (Leonard): Signatures of Interstellar Chemistry? *Planetary Science Journal*, 4(1):8.

Faggi, S., Villanueva, G. L., Mumma, M. J., and Paganini, L. (2018). The Volatile Composition of Comet C/2017 E4 (Lovejoy) before its Disruption, as Revealed by High-resolution Infrared Spectroscopy with iSHELL at the NASA/IRTF. AJ, 156(2):68.

Fougere, N., Combi, M. R., Tenishev, V., Rubin, M., Bonev, B. P., and Mumma, M. J. (2012). Understanding measured water rotational temperatures and column densities in the very innermost coma of Comet 73P/Schwassmann-Wachmann 3 B. Icarus, 221(1):174–185.

Gibb, E. L., Bonev, B. P., Villanueva, G., DiSanti, M. A., Mumma, M. J., Sudholt, E., and Radeva, Y. (2012). Chemical Composition of Comet C/2007 N3 (Lulin): Another "Atypical" Comet. ApJ, 750(2):102.

Gibb, E. L., DiSanti, M. A., Magee-Sauer, K., Dello Russo, N., Bonev, B. P., and Mumma, M. J. (2007). The organic composition of C/2001 A2 (LINEAR). II. Search for heterogeneity within a comet nucleus. Icarus, 188(1):224–232.

Gibb, E. L., Mumma, M. J., Dello Russo, N., DiSanti, M. A., and Magee-Sauer, K. (2003). Methane in Oort cloud comets. Icarus, 165(2):391–406.

Guilbert-Lepoutre, A. (2012). Survival of Amorphous Water Ice on Centaurs. AJ, 144(4):97.

Hui, M.-T., Jewitt, D., and Clark, D. (2018). Pre-discovery Observations and Orbit of Comet C/2017 K2 (PANSTARRS). AJ, 155(1):25.

Jewitt, D. (2009). The Active Centaurs. AJ, 137(5):4296–4312.

Jewitt, D., Hui, M.-T., Mutchler, M., Weaver, H., Li, J., and Agarwal, J. (2017). A Comet Active Beyond the Crystallization Zone. ApJ, 847(2):L19.

Lippi, M., Vander Donckt, M., Faggi, S., Moulane, Y., Mumma, M. J., Villanueva, G. L., and Jehin, E. (2023). The volatile composition of C/2021 A1 (Leonard): Comparison between infrared and UV-optical measurements. A&A, 676:A105.

Magee-Sauer, K., Mumma, M. J., DiSanti, M. A., Dello Russo, N., Gibb, E. L., Bonev, B. P., and Villanueva, G. L. (2008). The organic composition of Comet C/2001 A2 (LINEAR). I. Evidence for an unusual organic chemistry. Icarus, 194(1):347–356.

Martin, E. C., Fitzgerald, M. P., McLean, I. S., Doppmann, G., Kassis, M., Aliado, T., Canfield, J., Johnson, C., Kress, E., Lanclos, K., Magnone, K., Sohn, J. M., Wang, E., and Weiss, J. (2018). An overview of the NIRSPEC upgrade for the Keck II telescope. In Evans, C. J., Simard, L., and Takami, H., editors, *Ground-based and Airborne Instrumentation for Astronomy VII*, volume 10702 of *Society of Photo-Optical Instrumentation Engineers (SPIE) Conference Series*, page 107020A.

Martin, E. C., Fitzgerald, M. P., McLean, I. S., Kress, E., and Wang, E. (2016). Optical design of the slit-viewing camera for the NIRSPEC upgrade. In Evans, C. J., Simard, L., and Takami, H., editors, *Ground-based and Airborne Instrumentation for Astronomy VI*, volume 9908 of *Society of Photo-Optical Instrumentation Engineers (SPIE) Conference Series*, page 99082R.

McKay, A. J., DiSanti, M. A., Kelley, M. S. P., Knight, M. M., Womack, M., Wierzchos, K., Harrington Pinto, O., Bonev, B., Villanueva, G. L., Dello Russo, N., Cochran, A. L., Biver, N., Bauer, J., Vervack, Ronald J., J., Gibb, E., Roth, N., and Kawakita, H. (2019). The Peculiar Volatile Composition of CO-dominated Comet C/2016 R2 (PanSTARRS). AJ, 158(3):128.

Meech, K. J., Kleyna, J. T., Hainaut, O., Micheli, M., Bauer, J., Denneau, L., Keane, J. V., Stephens, H., Jedicke, R., Wainscoat, R., Weryk, R., Flewelling, H., Schunová-Lilly, E., Magnier, E., and Chambers, K. C. (2017). Co-driven activity in comet c/2017 k2 (panstarrs). *The Astrophysical Journal Letters*, 849(1):L8.

Ootsubo, T., Kawakita, H., Hamada, S., Kobayashi, H., Yamaguchi, M., Usui, F., Nakagawa, T., Ueno, M., Ishiguro, M., Sekiguchi, T., Watanabe, J.-i., Sakon, I., Shimonishi, T., and Onaka, T. (2012). AKARI Near-infrared Spectroscopic Survey for CO_2 in 18 Comets. ApJ, 752(1):15.

Prialnik, D. (1992). Crystallization, Sublimation, and Gas Release in the Interior of a Porous Comet Nucleus. ApJ, 388:196.

Prialnik, D. and Bar-Nun, A. (1992). Crystallization of amorphous ice as the cause of Comet P/Halley's outburst at 14 AU. A&A, 258(2):L9–L12.

Rayner, J., Tokunaga, A., Jaffe, D., Bond, T., Bonnet, M., Ching, G., Connelley, M., Cushing, M., Kokubun, D., Lockhart, C., Vacca, W., and Warmbier, E. (2022). iSHELL: a 1-5 micron R = 80,000 Immersion Grating Spectrograph for the NASA Infrared Telescope Facility. PASP, 134(1031):015002.

Roth, N. X., Gibb, E. L., Bonev, B. P., DiSanti, M. A., Mumma, M. J., Villanueva, G. L., and Paganini, L. (2017). The Composition of Comet C/2012 K1 (PanSTARRS) and the Distribution of Primary Volatile Abundances among Comets. AJ, 153(4):168.

Saki, M., Gibb, E. L., Bonev, B. P., Roth, N. X., DiSanti, M. A., Khan, Y., Dello Russo, N., Vervack, Ronald J., J., McKay, A. J., and Kawakita, H. (2021). Chemical Composition of Outbursting Comet C/2015 ER61 (PanSTARRS). AJ, 162(4):145.

Villanueva, G. L., DiSanti, M. A., Mumma, M. J., and Xu, L. H. (2012a). A Quantum Band Model of the ν_3 Fundamental of Methanol (CH_3OH) and Its Application to Fluorescence Spectra of Comets. ApJ, 747(1):37.

Villanueva, G. L., Magee-Sauer, K., and Mumma, M. J. (2013). Modeling of nitrogen compounds in cometary atmospheres: Fluorescence models of ammonia (NH_3), hydrogen cyanide (HCN), hydrogen isocyanide (HNC) and cyanoacetylene (HC_3N). J. Quant. Spec. Radiat. Transf., 129:158–168.

Villanueva, G. L., Mumma, M. J., Bonev, B. P., Novak, R. E., Barber, R. J., and Disanti, M. A. (2012b). Water in planetary and cometary atmospheres: H_2O/HDO transmittance and fluorescence models. J. Quant. Spec. Radiat. Transf., 113(3):202–220.

Villanueva, G. L., Mumma, M. J., DiSanti, M. A., Bonev, B. P., Gibb, E. L., Magee-Sauer, K., Blake, G. A., and Salyk, C. (2011a). The molecular composition of Comet C/2007 W1 (Boattini): Evidence of a peculiar outgassing and a rich chemistry. Icarus, 216(1):227–240.

Villanueva, G. L., Mumma, M. J., and Magee-Sauer, K. (2011b). Ethane in planetary and cometary atmospheres: Transmittance and fluorescence models of the ν_7 band at 3.3 μm. *Journal of Geophysical Research (Planets)*, 116(E8):E08012.

Villanueva, G. L., Smith, M. D., Protopapa, S., Faggi, S., and Mandell, A. M. (2018). Planetary Spectrum Generator: An accurate online radiative transfer suite for atmospheres, comets, small bodies and exoplanets. J. Quant. Spec. Radiat. Transf., 217:86–104.

Wainscoat, R. J., Wells, L., Micheli, M., and Sato, H. (2017). Comet C/2017 K2 (Panstarrs). *Central Bureau Electronic Telegrams*, 4393:1.

Wierzchos, K. and Womack, M. (2018). C/2016 R2 (PANSTARRS): A Comet Rich in CO and Depleted in HCN. AJ, 156(1):34.

Yang, B., Jewitt, D., Zhao, Y., Jiang, X., Ye, Q., and Chen, Y.-T. (2021). Discovery of Carbon Monoxide in Distant Comet C/2017 K2 (PANSTARRS). ApJ, 914(1):L17.

SECTION

3. SUMMARY AND CONCLUSIONS

3.1. ANALYSES OF YSO DATA

Observations of young stellar objects (YSOs) in the core of the L1688 cloud were obtained using the iSHELL instrument of the NASA IRTF telescope. These sources are stars that have completed the main accretion evolutionary stage but are still surrounded by gas and dust (i.e., they are deeply embedded). Analyses of spectroscopic observations of these sources have shown the presence of narrow absorption lines from molecular CO ν = 0-2 transitions. These absorption lines have been identified in eight YSO sources in the wavelength range 2.33 μm - 2.38 μm. By measuring the equivalent width of these absorption lines, the gas column density (column of gas along the line of sight to the surface of the YSO) was calculated to determine the excitation temperature of the transitions, which, at the spatial location of the source, gives temperature information of the foreground gas (gas in front of the YSO source). Some of the YSOs considered in the analyses (GY 235, WL 20E, WL 4, and WLY 2-51) have absorption lines only from the lower R and P branch lines and fit well with a single temperature that ranges from 20-26 K, while the remaining sources (VSSG 1, GY 33, SR 24S, and WLY 2-54) show evidence for a gradient in temperature with the cooler temperatures derived from the lowest R and P branch lines. For these sources, the entire spectrum (i.e., from multiple orders) could not be fit with a single temperature but a two-layered foreground gas temperature.

The ^{12}CO line profiles from the COMPLETE (Coordinated Molecular Probe Line Extinction and Thermal Emission) survey in a 40″ beam (Ridge et al., 2006) were constructed along the lines of sight that include each YSO. Except for GY 235, the ^{12}CO line profiles show evidence of self-absorption from the foreground gas, suggesting that a range of temperatures along the line of sight may be present. Lower limit estimates to the ^{12}CO brightness temperatures (11-33 K) generally agree with the gas temperature derived from the low R- and P-branch lines for some of our sources (GY 235, WL 4, and WL 20E). The CO column densities, proportional to the ^{13}CO integrated intensities from the large beam COMPLETE observations, correlate well with that derived in our analyses. The exception is GY 33, for which we derive the highest column density of any source (in both the hot and cold components). Without more detailed modeling, only a lower limit to the true column density from the lower R and P branch lines can be derived. Thus, this effort to determine the temperature of the foreground gas at the locations of the YSO sources from ground-based observation could be used as a good starting input to characterize the temperature profiles in conjunction with the satellite observations of CO.

3.2. STUDY OF THE CHEMICAL COMPOSITION OF COMETS AND CONTRIBUTION OF THIS RESEARCH

Following their formation in the cold, dense regions of the protoplanetary disk (PPD) midplane, comets were scattered out to the outer solar system, where they have been stored cryogenically for 4.5 Gyr. Thus, they preserve a record of volatile ices and refractory materials included in their nuclei from the PPD. By measuring coma molecular abundances (which reflect the nucleus ice composition) of Oort Cloud comets, one can thus explore the retained records of the midplane chemistry of the PPD.

In addition, a comparison of the protosolar nebula astrochemical predictions to the volatile emission measurements of the ices in the comets unveil the physical and chemical processes involved during the early formation of our solar system (e.g., Bergner and Ciesla, 2021; Eistrup et al., 2019; Willacy et al., 2022). Furthermore, since the disk midplane of extrasolar PPDs are generally optically thick to observations, the comet-forming region and the ice-phase chemistry occurring within is primarily obtained from dynamical and astrochemical models (e.g., Drozdovskaya et al., 2016; Willacy et al., 2022). Thus, the molecular abundances preserved in comets can be utilized as one of the few constraints on these models. In this context, Oort Cloud comets (OCCs), such as the two comets presented in this study (C/2020 S3 and C/2017 K2), are particularly relevant owing to their infrequent perihelion passages through the inner solar system due to their long orbital periods and thus contain relatively unaltered nucleus compositions. Furthermore, studies on interstellar molecules in the gas phase indicate that the primary source of ices found in cometary nuclei is likely interstellar ices, which are formed in the pre-solar molecular cloud core (Altwegg et al., 2019; Bockelée-Morvan and Biver, 2017; Mumma and Charnley, 2011). On the other hand, a comparison of sublimed cometary volatile ices to interstellar ices that is not in the gas phase has shown that the mixing ratios of interstellar ices (with respect to H_2O) are typically enriched compared to cometary ices (Öberg et al., 2011). These variations in mixing ratios could result from the thermal evolution of the cometary nuclei during repeated passages through the inner solar system. Therefore, determining mixing ratios in long-period comets, such as C/2020 S3 and C/2017 K2, that are less subject to thermal evolution due to their infrequent passage through the inner solar system is crucial for investigating the chemical similarity between cometary ices and interstellar ices.

3.2.1. Comet C/2020 S3 (Erasmus). The observations of comet S3 were obtained during two nights on November 29 and December 1, 2020, when the comet was in its pre-perihelion orbit at heliocentric distances of 0.49 AU and 0.52 AU, respectively.

There is a paucity of measurements of the volatile composition of comets (both JFCs and OCCs) at small heliocentric distances ($R_h \leq 0.80$ AU) at near-infrared wavelengths mainly due to observational circumstances such as the solar elongation limit for daytime observations of comets like C/2020 S3 (e.g., DiSanti et al., 2017). Those very few comets observed at $R_h < 0.8$ AU showed enrichment in abundances in some volatile species such as C_2H_2, NH_3, and H_2CO compared to the measurements obtained at $R_h > 0.80$ AU (Dello Russo et al., 2016b; DiSanti et al., 2016). This enrichment is possibly due to the contribution from additional sources in the coma related to the thermal decomposition of organic dust as the comet gets closer to the Sun (Dello Russo et al., 2016a). Our measurements of abundances of volatile species in comet S3 showed enrichment in abundances for H_2CO, NH_3 and C_2H_2, compared to their average abundances from OCCs measured at $R_h > 0.80$ AU. Thus, the compositional measurements of comet S3 add valuable measurements to the sample of comets observed at small R_h to build the trend of volatile abundances of comets for measurements made at $R_h < 0.80$ AU. The general implication of such measurement is that comets observed beyond 0.8 AU may be preferred for overall compositional investigations of the nucleus if the trends in the enrichment of some volatile species seen for comets observed closer to the Sun are compatible with the theory that some molecules originate from alternate sources. Conversely, this suggests that comets observed closer to the Sun could yield important insights into molecules and processes often not exhibited when the comet is relatively far from the Sun. Another interesting contribution of comets observed at small R_h is that high energy lines of certain species like CN are excited owing to their proximity to the Sun. These high-energy lines can only be fit by fluorescence models produced at higher temperatures.

However, currently, there is no available fluorescence model for CN lines at temperatures greater than 100 K due to a lack of good spectra to fully parameterize the model for CN bands at higher temperatures. Thus, measurements for bright comets such as S3 add to the sample of the few comets observed close to the Sun (e.g., Roth et al., 2018) that can be used to develop CN fluorescence models for temperatures greater than 100 K.

3.2.2. Comet C/2017 K2 (Pan-STARRS). The main goal of the project in studying comet K2 was to *study the transition of cometary activity as it approaches the H_2O ice-line, and H_2O supplants CO as the dominant driver of activity*. At $R_h > 3$ AU, outgassing in comets is driven mainly by the sublimation of more volatile ices such as CO and CO_2 (Bonev et al., 2017; McKay et al., 2019; Ootsubo et al., 2012). Within $R_h \sim 2.0$ AU, where most comet primary volatile measurements are performed (Crovisier et al., 2004; Meech et al., 2017), comets are thought to have completed the transition from hypervolatile-dominated to H_2O-dominated activity. To date, while ~ 30 OCCs have been characterized using high-resolution infrared spectroscopy, very few have been observed at the transitional heliocentric distance ranges of $R_h \sim 2.0$ - 3.0 AU (e.g., Dello Russo et al., 2016a) owing to most comets being quite faint, or their activity levels being too low to accurately measure CO and H_2O over this range of R_h. As a result, where the transition from hypervolatile-driven activity to water activation occurs remains uncertain. Towards the goal of investigating this less explored transition region of cometary activity, comet K2 offered a rare opportunity to measure these molecules in this critical range of R_h as it started to show activity (based on the prediscover archival data) at ~ 23 AU from the Sun (Hui et al., 2018; Jewitt et al., 2017; Meech et al., 2017), and was available for study over a range of R_h ~3.2 – 2.35 AU during our observations (May 2022-Aug 2022). In this study, the volatile composition for multiple molecular species (CO, C_2H_6, CH_4, H_2O) were sampled at the edge of the H_2O ice-line (~ 2.3 -3.0 AU) to characterize the interplay between the volatiles driving activity in this less-explored heliocentric distance transition region.

Our results indicate that, compared to other comets observed at similar R_h (~ 2.80 - 3 AU (Bockelée-Morvan et al., 2010; Bonev et al., 2017; McKay et al., 2019), the CO production rate in K2 at a comparable distance is less than an order of magnitude. We note that the production rate in comets depends on several factors such as orbital stage (whether it is in its pre- or post-perihelion path), whether the comet is dynamically new (coming to the inner solar system for the first time since scattered out to KB or OC region) or dynamically old, dust to gas ratio of the comet, size of the nucleus, and the fractional active surface of the nucleus (e.g., Bonev, 2005). The estimate of the upper limit of the nucleus radius size of comet K2 is ≤ 9 km (Jewitt et al., 2017). Even though the nucleus radius size of comet C/2016 R2 is unknown, based on its CO production rate, it is estimated to be less than ~ 15 km (Wierzchos and Womack, 2018). Thus, the nucleus size is possibly not a significant factor to account for an order of magnitude difference in CO production rate between comets K2 and C/2016 R2.

To address one of the main goals we set out in studying comet K2, the H_2O was measured using the NIRSPEC and iSHELL instrument at R_h = 2.54, 2.48 and 2.35 AU distances from the Sun. The H_2O production rate increased more steeply than other molecules near ~2.3 AU. To tell whether H_2O was fully active, molecular abundances of simultaneously (contemporaneously) measured species with H_2O such as HCN, C_2H_2, C_2H_6, CH_4, CH_3OH and CO were computed. Our measurements show that the mixing ratios of these volatile species relative to simultaneously measured H_2O are significantly higher than their range of mean values from OCCs measured to date in NIR within 2.0 AU (see e.g., Dello Russo et al., 2016a). This implies that either the abundances of these volatiles in K2 are enriched as was the case for comet C/2001 A1 (Gibb et al., 2007; Magee-Sauer et al., 2008) or, given the changing H_2O production rate over a range of our observations, that H_2O is not yet fully activated at these heliocentric distances from the Sun. Thus, to conclusively decide the H_2O activation distance of comet K2, more observations at heliocentric distances smaller than 2.35 AU are required.

3.2.3. Putting iSHELL Studies of K2 in Context. Combining facilities to conduct synergistic investigations of comets can yield information on potential time-variability, outgassing patterns, and correlations between chemical composition and spatial relationships (e.g., Khan et al., 2021; Roth et al., 2021). Observations of CO, HCN, CH_3OH, and H_2CO in comet K2 were acquired using Atacama Large Millimeter/Submillimeter Array (ALMA) around the same time as the iSHELL observations of K2 to characterize coma volatile composition of comet K2. However, symmetric molecules like CH_4 and C_2H_6, crucial to characterize the overall composition of K2, can not be observed at radio (mm/sub-mm) wavelengths, making the iSHELL measurements of these hypervolatiles at the infrared wavelength very important. From space-based observations, comet K2 has been observed using the James Webb Space Telescope (JWST). However, at the resolution of JWST, solid-ice spectral features cannot be disentangled from the gas phase organics (those detected by iSHELL). Thus, the iSHELL measurements of K2 provide an important comparison that will enhance the overall scientific goal of fully characterizing the volatile composition of K2, thereby making a vital addition to the sample of OCCs measured at the infrared wavelength region for the overall taxonomical classification of comets based on chemical composition.

APPENDIX A.

REDUCTION AND ANALYSES OF YSO SPECTRA

1. DATA REDUCTION

1.1. DARK SUBTRACTION

To account for any bias and dark current, a master dark frame, obtained by median-combining a set of (usually 5) dark frames, must be subtracted from each science frame before extraction. These dark frames need the same integration times as the science and telluric star frames.

1.1.1. Flatfielding. A set of quartz lamp images (usually 5) observed close in time to the science targets is needed for flat-fielding. The science frames must be divided by the normalized master flat-field image obtained by median-combining the flat-field frames using the xspextool task. The purpose of flat-fielding is to remove pixel-to-pixel quantum efficiency variations in the array. The Spextool does not subtract the dark from the flats.

1.2. REDUCING THAR ARC IMAGES

The thorium-argon arc lamp spectra (usually 2) taken close in time to the science data need to be reduced before generating the wavelength calibration solution. First, the arc lamps need to be flat-fielded using the xspextool task. The Spextool does not subtract darks from the arc lamps. Then, the program generates a wavelength calibration solution.

1.3. WAVELENGTH CALIBRATION

Spextool subtracts the master dark from the science frames, divides the dark-subtracted science frames by the master flat field, and wavelength calibrates the frames to the lines from the calibration arc lamp.

1.4. EXTRACTION

`Spextool` extracts each science spectrum using point source extraction configuration. Spextool automatically finds the spatial profile. The number of apertures that need to be found has to be specified. Then, it finds aperture positions and traces the order. The extraction width needs to be specified along with the background subtraction radius. Normally, the background sample has to lie outside of the extraction width of the spectrum. Finally, Spextool extracts the spectra. After that, Spextool can do all the steps from wavelength calibration to the extraction, at the same time, once the parameters are set for one frame, by entering the remaining science frames.

1.5. REDUCING THE TELLURIC SOURCE

An A0 standard star spectrum taken close in time to the science targets is needed for telluric correction. The telluric standard source has to be dark-subtracted, flat-fielded, and wavelength calibrated similarly to the science source, making sure that the master dark is of the same exposure as the telluric source and has to be extracted with the same extraction parameters set for the source.

1.6. COMBINING EXTRACTED SPECTRA

The signal-to-noise ratio of the final spectra is increased by combining the individual multi-order extracted spectra using the `xcombspec` task. Firstly, all orders must be scaled to a common order, usually one of the middle orders. This single scale factor is then applied to all spectrum orders. This is the stage at which one can mask out bad pixels using the “prune spectra” command before combining spectra. Then, all orders are combined to get a final single extracted and wavelength-calibrated spectrum.

1.7. TELLURIC CORRECTION

Telluric features (atmospheric absorption lines) are removed from the source spectra by dividing the source spectrum by the telluric standard spectrum using the `xtellcor` task (Vacca et al., 2003). Even after dividing the source spectrum by the telluric, we noticed unremoved telluric features in the final spectrum. This is due to a slight wavelength shift between the telluric spectrum and the object spectrum that is believed to be arising from the sub-pixel flexure of the instrument as the telescope moves between the object and the standard. Thus, we had to apply a corrective shift of about 0.25 to 0.5 pixels to the telluric spectrum to optimize the telluric correction.

1.8. CLEANING AND SMOOTHING THE SPECTRA

The last step of data reduction, which can be done, is removing or fixing a spectrum region using the `xcleanspec` task. It is also possible to smooth the spectra during the cleaning process, usually using the Savitzky-Golay smoothing function in xcleanspec. This function uses a nine-pixel width box for smoothing, and it preserves the average resolving power of the instrument.

2. ANALYSES OF INTERSTELLAR ABSORPTION LINES

2.1. CALCULATING THE DOPPLER SHIFTS OF THE SPECTRAL ABSORPTION LINES

Before proceeding with an analysis of the absorption lines, calculating the Doppler shift for each absorption line is necessary to check whether the line has been misidentified or is blended. This can be seen if Doppler shifts significantly differ from the average value. The Doppler shift of spectra is calculated as $\mathrm{v}_r = c\frac{\Delta\lambda}{\lambda_0}$, where $\Delta\lambda$ represents a shift in wavelength from the (known) rest (that is laboratory) wavelength λ_0, c (in $\mathrm{km\,s^{-1}}$) is the speed of light and v_r (in $\mathrm{km\,s^{-1}}$) is the velocity of the source along the line of sight from Earth.

2.2. COLUMN DENSITY CALCULATION

To determine the total number of atoms per unit area in all energy levels, how they are distributed (partitioned) among their energy levels must be known. In general, under conditions of equilibrium, the probability P_r of finding a given system in any particular state r of energy E_r is:

$$P_r = \frac{e^{-\frac{E_r}{kT}}}{\sum_r e^{-\frac{E_r}{kT}}} . \tag{1}$$

The quantity $\sum_r e^{-\frac{E_r}{kT}}$ is called the partition function; the sum extends over all possible states of the system irrespective of energy. Thus, if there are a total of N atoms, each of which has m possible energy levels, and if there are N_j atoms in energy level E_j, the total number of atoms is

$$N = \sum_{j=1}^{m} N_j, \tag{2}$$

where the integer j runs from 1 to m. Thus, the ratio between the number of atoms in level j and the total number of atoms per unit area in all levels is:

$$\frac{N_j}{N} = \frac{g_j e^{-\frac{E_j}{kT}}}{\sum_{j=1}^{m} g_j e^{-\frac{E_j}{kT}}}, \tag{3}$$

where g is the degeneracy of the energy levels in an atom. The denominator of the expression,

$$\sum_{j=1}^{m} g_j e^{-\frac{E_j}{kT}} = Q_{tot}, \tag{4}$$

is the total partition function. Thus, the column density of a line in a lower state (in cm^{-2}) for each transition can be determined from a measurement of the line strength (equivalent width) as follows:

$$N_{J''} = \frac{W_\lambda}{f\lambda^2}\left(\frac{m_e c^2}{\pi e^2}\right) = \frac{W_\lambda}{f\lambda^2(8.853 \times 10^{-13})}, \tag{5}$$

where 8.853×10^{-13} cm is the classical electron radius, $\frac{\pi e^2}{m_e c^2}$, f is the dimensionless oscillator strength of the transition, W_λ is the equivalent width of the line in units of *cm*, and J″ represents the lower state. To estimate the measurement uncertainty, we applied error propagation by rewriting Equation 5 as $N_{J''} = \frac{W_\lambda}{a\lambda^2}$, where a=f$(8.853 \times 10^{-13})$. This simplified equation is of the form x= $f(u, v)$ and the measurement uncertainty on the function x can be estimated as $\sigma_x = |x|\sqrt{(\frac{\sigma_u}{u})^2 + (\frac{\sigma_v}{v})^2}$, according to Bevington and Robinson (2003). The denominator of Eq. 5 is of the form $x = au^b$, and its uncertainty is given by $\sigma_x = bx\frac{\sigma_u}{u}$. Thus, the uncertainty on the column density is given as $\sigma_{N_{J''}} = N_{J''}\sqrt{(\frac{\sigma_{W_\lambda}}{W_\lambda})^2 + (\frac{2\sigma_\lambda}{\lambda})^2}$.

2.3. ROTATIONAL ENERGY OF A DIATOMIC MOLECULE

Consider the diatomic molecule shown in Figure 1. In general, the coordinates of

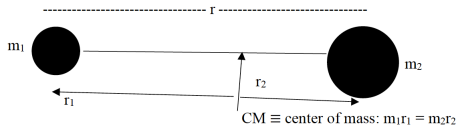

Figure 1. Diatomic Molecule, as a rigid rotator.

the center of mass (CM) are given by

$$\vec{r}_{cm} = \frac{\sum_i \vec{r}_i m_i}{\sum_i m} = \frac{\vec{r}_1 m_1 + \vec{r}_2 m_2}{m_1 + m_2} \tag{6}$$

Taking m_1 as located at the origin of the coordinate system:

$$\vec{r}_{cm} = \vec{r}_1 = \frac{\vec{r} m_2}{m_1 + m_2} \tag{7}$$

Similarly, taking m_2 as located at the origin of the coordinate system:

$$\vec{r}_{cm} = \vec{r}_2 = \frac{\vec{r} m_1}{m_1 + m_2} \tag{8}$$

Thus for a rotation about the *CM*, the moment of inertia, I:

$$I = m_1 r_1^2 + m_2 r_2^2 = m_1 \left(\frac{r m_2}{m_1 + m_2}\right)^2 + m_2 \left(\frac{r m_1}{m_1 + m_2}\right)^2 = r^2 \frac{m_1 m_2}{m_1 + m_2} = \mu r^2 \tag{9}$$

$$KE_{rot} = E_{rot} = \frac{1}{2} I\omega^2 = \frac{1}{2} \underbrace{(I\omega)}_{L} \omega = \frac{1}{2} L \left(\frac{L}{I}\right) = \frac{L^2}{2I}, \tag{10}$$

A diatomic molecule possesses angular momentum due to its rotation about the axis perpendicular to the line joining the atoms and electronic angular momentum. However, because the rotations of diatomic molecules are approximated as the rigid rotator, the total angular momentum of the diatomic molecule **J** is approximately the same as the angular momentum of L of the rigid rotator. Thus, the rotational energy of a diatomic molecule is $E_{rot} \approx \frac{\mathbf{J}^2}{2I}$. The total angular momentum **J** is quantized: $\mathbf{J}^2 = J(J+1)\hbar^2$, J = 0,1,2,... It is worth noting that in the case of rotating molecules, a capital J notation is also used as a quantum number directly, whereas, in the case of an electron, the total angular momentum quantum numbers are designated as $j = |\ell \pm s|$. For example, transitions are labeled as J = 1 $\rightarrow$ 0 to indicate that a molecule has moved from the first excited rotational state to its ground state.

The Eigenvalue equation (the time independent Schrödinger equation)is:

$$H\psi = E\psi = \frac{1}{2I} J^2 \psi = J(J+1)\frac{\hbar^2}{2I}\psi, \tag{11}$$

where $h = 2\pi\hbar$, is Planck's constant. Thus,

$$E = \frac{\hbar^2}{2I} J(J+1). \tag{12}$$

The set of solutions to $\frac{1}{2I}\hat{J}^2\psi = E\psi$ are spherical harmonics: $\psi_{JM_J} = Y_J^{M_J}(\theta,\phi) = P_J^{M_J}(\cos\theta)e^{iM_J\phi}$, where $J = 0, 1, 2, \ldots$, is the rotational quantum number, and it can have several discrete spatial orientations labeled by M_J, its projection onto the molecular axis (see Fig. 2).The possible values of M_J are: M_J = -J, -J+1,..., 0, ..., (J-1), J. Thus, each value of J has $2J + 1$ possible quantum states of the same energy.

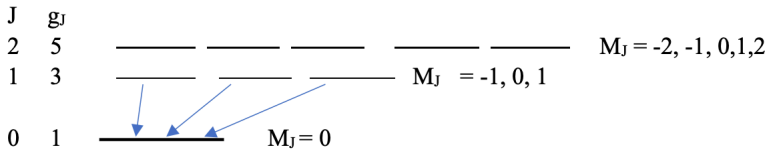

Figure 2. The degeneracy of energy levels.

The rotational spectrum of a diatomic molecule such as *CO* can be approximated as a rigid rotor and can be calculated as:

$$E_{rot} = \frac{\hbar^2}{2I}J(J+1), \tag{13}$$

where $h = 2\pi\hbar$ is Planck's constant; J = 0,1,2, ..., is the rotational quantum number; and I is the moment of inertia about the center of mass of the rotating diatomic molecule.

Energy in wavenumber units:

In general,

$$E = h\nu = h\left(\frac{c}{\lambda}\right) = hc\left(\frac{1}{\lambda}\right) = hc\tilde{\nu} \Rightarrow \tilde{\nu} = \frac{E}{hc}, \tag{14}$$

where the quantity $\tilde{\nu} = \frac{1}{\lambda}$ is the wave number (in cm^{-1}). Thus, the rotational energy, ε_r, in units of cm^{-1}:

$$\varepsilon_r \approx \frac{\hbar^2 J(J+1)}{2Ihc} \approx \frac{h}{8\pi^2 Ic}J(J+1) \approx BJ(J+1), \tag{15}$$

where B= $\frac{h}{8\pi^2 Ic}$ is the rotational constant in cm^{-1} units. It is worth noting that there is no rotational zero point energy, and the energy levels are separated by $\Delta\varepsilon_r = 2B(J''+1)$, where $J'' = J_{lower}$.

2.4. MOLECULAR PARTITION FUNCTION

Having derived the form of rotational energy of a diatomic molecule, the partition function of a diatomic molecule under certain temperature conditions is needed.
The total rotational partition function is given by

$$Q_{tot} = \sum_{J=0}^{\infty} (2J+1) e^{-\frac{hcB}{kT} J(J+1)}. \tag{16}$$

If we consider the ratio of rotational to thermal energy, $\frac{hcB}{kT} J(J+1)$, then for low temperature T or small moment of inertia, $\frac{hcB}{kT} \gg 1$ and $e^{-\frac{hcB}{kT} J(J+1)} \rightarrow 0$. If the temperature T is high and the moment of inertia is not very small, then $\frac{hcB}{kT} J(J+1) \ll 1$ and the rotational levels are closely spaced together. The summation in the above equation can be replaced by an integral:

$$Q_{tot} \approx \int_0^{\infty} du\, e^{-\frac{hcB}{kT} u}, \tag{17}$$

where u = $J(J+1)$. Thus, the total rotational partition function is given by

$$Q_{tot} \approx \frac{kT}{hcB}, \tag{18}$$

where k is the Boltzmann constant, T is the temperature, h is the Planck's constant, c is the speed of light, and B is the rotational constant. For temperatures greater than 20 K, the high-temperature limit formula for the total partition function for diatomic molecules such as *CO* gives roughly comparable values with those obtained from the formula for partition function using summation over the levels.

2.5. FRACTIONAL POPULATION

The fractional population is the contribution of each transition to the total population of the gas. The column density in the lower state can be related to the total column density for a molecule using the fractional population, $N_{J'',rel}$

$$N_{J'',rel} = \frac{N_{J''}}{N_{tot}} = \frac{g_{J''}}{Q_{tot}} e^{-\frac{E_{J''}}{kT_{rot}}} = \frac{2J''+1}{Q_{tot}} e^{\frac{-hcBJ''(J''+1)}{kT}} \tag{19}$$

$$\Rightarrow N_{tot} = N_{J''} \frac{Q_{tot}}{g_{J''} e^{-\frac{E_{J''}}{kT_{rot}}}}. \tag{20}$$

The fractional population is the contribution of each transition to the partition function divided by the total partition function at that rotational temperature. It is worth noting that the total column density N_{tot} is the average value of $\frac{N_{J''}}{N_{J'',rel}}$. To estimate the uncertainty on fractional population, we first write as:

$$N_{J'',frac} = \frac{(2J''+1)hcB}{kT} e^{\frac{-hcBJ''(J''+1)}{kT}} = \frac{ae^{\frac{-b}{T}}}{T} = \frac{A}{B}.$$

$\sigma_B = \sigma_{T^{-1}} = \frac{-\sigma_T}{T^2}$.

A = $ae^{\frac{-b}{T}} = ae^{-bu}$, which is a function of the form x= $ae^{\pm bu}$ with $\sigma_x = \pm bx\sigma_u$.

Thus, $\sigma_A = bA\frac{\sigma_T}{T^2}$.

Thus, the measurement uncertainty on the fractional population is given as follows:

$$\sigma_{N_{J''},frac} = N_{J'',frac} \sqrt{\left(\frac{b\sigma_T}{T^2}\right)^2 + \left(\frac{\sigma_T}{T}\right)^2}$$

The uncertainty on the total column density, $N_{tot} = \frac{N_{J''}}{N_{J'',frac}}$, can be estimated following a similar procedure. We finally compute the weighted mean for the total column density from the transitions using $\bar{x} = \frac{\sum(x_i/\sigma_i^2)}{\sum(1/\sigma_i^2)}$, with error in the weighted mean using the relation $\sigma_\mu = \frac{1}{\sqrt{\sum(1/\sigma_i^2)}}$

2.6. OPTICAL DEPTH CALCULATION

To check if the column densities of the absorption lines were derived from optically thin lines, and thus no correction for optical depth was needed, the maximum optical depth of the observed transitions needs to be estimated. According to the Maxwellian distribution of a molecular velocity component, $\mathrm{g(v}_x)\mathrm{dv}_x = n\left(\frac{m}{2\pi kT}\right)^{\frac{1}{2}} e^{-\frac{mv_x^2}{2kT}} dv_x$, each component of velocity is distributed with a Gaussian distribution symmetric about the mean value $\bar{v}_x = 0$ (Reif, 1965).

The Equipartition Theorem states that each independent quadratic term in the energy contributes a mean value of $\frac{1}{2}kT$. Thus,

$$\frac{m}{2}\bar{v_x^2} = \frac{1}{2}kT \Rightarrow \bar{v_x^2} = \frac{kT}{m} \tag{21}$$

Thus, the root-mean-square width of the Gaussian distribution,$\sqrt{\bar{v_x^2}} = \left(\frac{kT}{m}\right)^{\frac{1}{2}}$. The lower the temperature, the narrower the width of the distribution function $\mathrm{g(v}_x)$.

The optical depth τ is related to the column density and the oscillator strength as:

$$\tau = \frac{N_{tot} f N_{J'',rel}}{b\tilde{\nu}}\left(\frac{\pi e^2}{m_e c}\right) = \frac{f N_{tot}}{b\tilde{\nu}}\frac{N_{J''}}{N_{tot}}\left(\frac{\pi e^2}{m_e c}\right) = \frac{f N_{J''}}{b\tilde{\nu}}\left(\frac{\pi e^2}{m_e c}\right) = \frac{f N_{J''}}{b\tilde{\nu}(6.68\times 10^6)}, \tag{22}$$

where f is the oscillator strength, $\tilde{\nu}$ is the wavenumber in cm^{-1}, $\mathrm{N}_{J''}$ is the column density in cm^{-2}. The parameter $b = \left(\frac{2kT_{rot}}{m}\right)^{\frac{1}{2}}$, with m being the mass of the molecule, is called the intrinsic line width (or the doppler width). A value of τ on the order of 1 or less is sufficient to be considered optically thin, and in the case of our observations, the calculated values of τ were well below 1.

APPENDIX B.

COMET DATA REDUCTION AND ANALYSES OVERVIEW

1. DETERMINING GROWTH FACTOR

The Growth factor, the ratio of the terminal (total) production rate to the nucleus-centered production rate, is determined using Q-curve analysis.

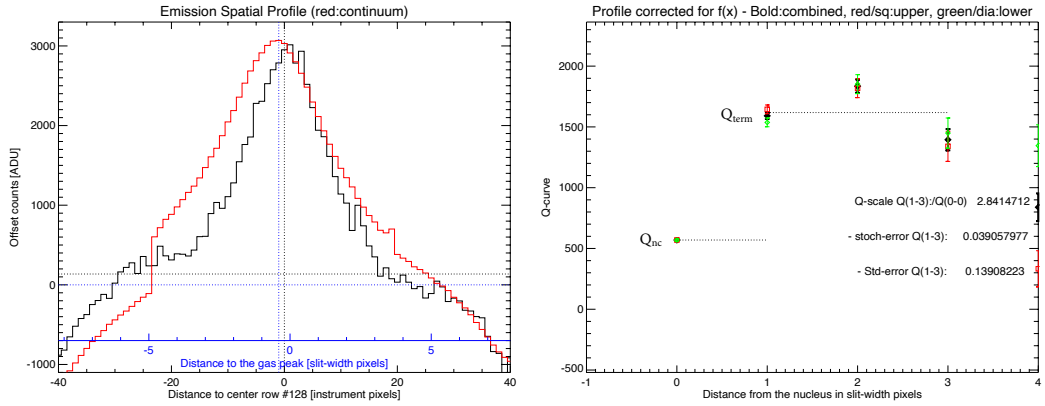

Figure 1. Determination of the Growth Factor using the Q-curve analysis method for C_2H_6 from S3 spectra during November 29, 2020, showing that the production rate increases from nucleus centered value to its final (terminal) value after which it remains constant.

2. DETERMINING ROTATIONAL TEMPERATURES

The excitation condition in the coma of a comet can be quantified by a rotational temperature (T_{rot}), which depends on the fractional strength of each ro-vibrational band contained by the observed emission lines (DiSanti et al., 2016). The rotational temperature is obtained using correlation and zero-slope excitation analyses. The rotational temperature is run over a range of temperatures covering the assumed temperature range of the inner coma of a comet (10-150 K). The observed comet residuals are compared to the model at each run step.

2.1. CORRELATION ANALYSIS

This method is based on the agreement between the convolved model (to the resolving power of the observed spectrum) and the observed comet residual. At each step in rotational temperature, a correlation coefficient, *R*, between the model and the data is computed. The most probable rotational temperature corresponds to the value of R with the maximum value, and the sharpness of this maximum indicates how well T_{rot} can be constrained. In Fig. 2, the second panel from the left shows the correlation analysis of K2, picking the highest correlation value corresponding to the best-fit rotational temperature.

2.2. ZERO SLOPE EXCITATION ANALYSIS

The fluorescence g-factors depend on rotational temperature. The g-factor of each emission line is multiplied by the fully resolved transmittance at the frequency of the Doppler shifted line center to express the g-factor in watts per molecule. This lets one compare it with the observed line flux, F_{line} (W m^{-2}). The ratio F_{line}/g (molecule m^{-2}) is proportional to the column density of molecules. At the correct T_{rot}, F_{line}/g is independent of rotational energy (DiSanti et al., 2006). In Fig. 2, the second panel from the end shows the zero slope excitation analysis method of determining best-fit rotational temperature.

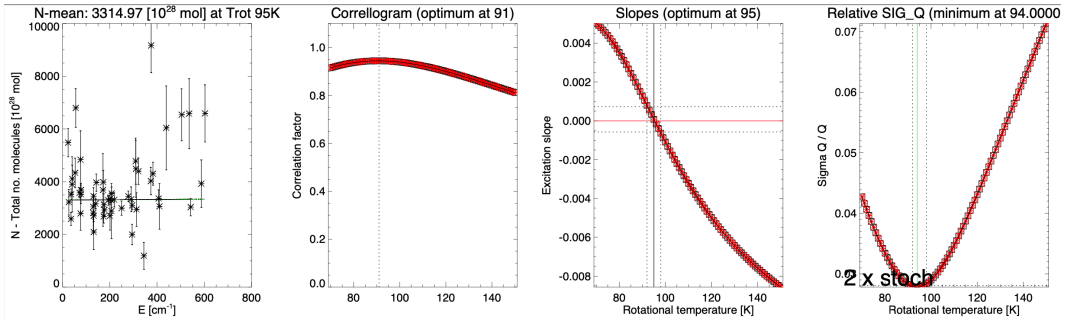

Figure 2. Rotational temperature determination from correlogram and zero-slope analyses methods for H_2O from S3 spectra during November 29, 2020 showing that consistent rotational temperatures are retrieved from each method.

3. CALCULATING PRODUCTION RATES AND MIXING RATIOS

3.1. UNCERTAINTIES ON PRODUCTION RATE

The uncertainties on the production rate of a given molecule take into account uncertainties due to the Growth Factor, the production rate of the molecule (Q_X), and flux calibration (Gamma).

$$\sigma_{Q_X} = Q_X \times \sqrt{\left(\frac{\sigma_{Q_X}}{Q_X}\right)^2 + \left(\frac{\sigma_{GF}}{GF}\right)^2 + (\sigma_\Gamma)^2} \tag{1}$$

We note that if a *GF* was assumed for a given molecule due to a low signal, then the uncertainty in the production rate of species needs to be calculated without taking into account uncertainty due to the *GF*

3.2. UNCERTAINTIES ON MIXING RATIOS

The uncertainties in *mixing ratio* of a given molecule take into account uncertainties on the production rate of the molecule (Q_X) and uncertainty on simultaneously or contemporaneously measured H_2O (Q_{H_2O}).

$$\sigma_{MixingRatio} = \left[\left(\frac{Q_X}{Q_{H_2O}}\right) \times 100\right] \times \sqrt{\left(\frac{\sigma_{Q_X}}{Q_X}\right)^2 + \left(\frac{\sigma_{Q_{H_2O}}}{Q_{H_2O}}\right)^2} \tag{2}$$

We note that if the molecule under consideration was observed with the same setting as H_2O (i.e., if it was observed simultaneously with H_2O), uncertainties on the mixing ratio need not account for uncertainty due to flux calibration, that is, the production rates of the molecule (Q_X) and Q_{H_2O} need to be calculated *without* accounting for the uncertainty due to flux calibration to calculate uncertainty on the mixing ratio.

APPENDIX C.

PERMISSIONS FOR FIGURES

1. PERMISSION FOR FIGURE 1.1 FROM THOMAS GREENE

FW: Form submission from: Request Permission to Copy for Educational Use

ME **Mia Evans <mevans@sigmaxi.org>** Today at 8:58 AM

To: Ejeta, Chemeda (S&T-Student)

WARNING: This message has originated from an External Source. This may be a phishing expedition that can result in unauthorized access to our IT System. Please use proper judgment and caution when opening attachments, clicking links, or responding to this email.

Thank you for contacting American Scientist. Permission is kindly granted. This permission is for one-time educational use only. If you need further assistance, please feel free to contact me.

Thank you for your request.

Mia Evans
Editorial Associate

From: noreply@americanscientist.org <noreply@americanscientist.org>
Sent: Monday, February 19, 2024 2:41 PM
To: Mia Evans <mevans@sigmaxi.org>
Subject: Form submission from: Request Permission to Copy for Educational Use

Submitted on Monday, February 19, 2024 - 2:40pm Submitted by user: Anonymous Submitted values are: Purpose: Educational Use Requested by: Chemeda Tadese Ejeta Institution: University of Missouri - St. Louis Telephone: 3146293730 Email: cteqnf@umsystem.edu Quarter/year: 2001 Expected enrollment (number of copies requested): 1 Volume: 89 Pages: 1 Article title: Protostars: "Stellar embryology" takes a step forward with the first detailed look at the youngest Sun-like stars Author(s): Thomas P. Greene

2. PERMISSION FOR FIGURE 3.2 FROM ALAN STERN

Re: Using Figure of your paper in my dissertation

AS ○ **Alan Stern <astern@boulder.swri.edu>** Thursday, October 5, 2023 at 1:39 PM

To: Ejeta, Chemeda (UMSL-Student); **Cc:** astern@swri.org

Approved if you cote the Nature paper for proper credit.

-Alan

Sent from my iPhone

On Oct 5, 2023, at 1:30 PM, Ejeta, Chemeda (UMSL-Student) <cteqnf@mst.edu> wrote:

[EXTERNAL EMAIL]

Dear S. Alan,

I am a Ph.D. student at the University of Missouri - St. Louis. I am in the final stage of submitting my dissertation on comets.

I am contacting you to request for your permission to use Figure 1 (Diagram illustrating KB and OC region) in the introduction section of my dissertation.

Thanks in advance for your time!

Sincerely,
Chemeda Tadese Ejeta

3. PERMISSION FOR FIGURE 3.1 FROM GERONIMO VILLANUEVA

From: Villanueva, Geronimo (he,his) (GSFC-6900) <geronimo.l.villanueva@nasa.gov>
Date: Tuesday, October 31, 2023 at 10:00 PM
To: Ejeta, Chemeda (UMSL-Student) <cteqnf@mst.edu>
Subject: Re: [EXTERNAL] Permission to use Figure 1 of this paper in my dissertation

WARNING: This message has originated from an External Source. This may be a phishing expedition that can result in unauthorized access to our IT System. Please use proper judgment and caution when opening attachments, clicking links, or responding to this email.

Sure Chemeda!

All the best with the dissertation, and thank you for consulting about using the figure,

Best,
Geronimo

Dr. Gerónimo Villanueva (he/him/él)
Associate Director, Strategic Science
Solar System Exploration Division
NASA Goddard Space Flight Center
http://astrobiology.gsfc.nasa.gov/Villanueva

Note: This conversation is restricted, so you might not be able to cut or copy from it. See the information above the To line for more details. Also, while the conversation is restricted, the conversation owner can send the message to other people.

From: "Ejeta, Chemeda (UMSL-Student)" <cteqnf@mst.edu>
Date: Tuesday, October 31, 2023 at 10:53 PM
To: "Villanueva, Geronimo Luis (GSFC-6930)" <geronimo.l.villanueva@nasa.gov>
Subject: [EXTERNAL] Permission to use Figure 1 of this paper in my dissertation

Hi Geronimo,

I am contacting you to request for your permission to use Figure 1 of this paper (which is originally yours) in the intro section of my dissertation on comets. Of course, needless to say that I will properly cite that the Figure is originally yours (as indicated in this paper).

Thank you,
Chemeda

REFERENCES

A'Hearn, M. F., Feaga, L. M., Keller, H. U., Kawakita, H., Hampton, D. L., Kissel, J., Klaasen, K. P., McFadden, L. A., Meech, K. J., Schultz, P. H., Sunshine, J. M., Thomas, P. C., Veverka, J., Yeomans, D. K., Besse, S., Bodewits, D., Farnham, T. L., Groussin, O., Kelley, M. S., Lisse, C. M., Merlin, F., Protopapa, S., and Wellnitz, D. D. (2012). Cometary Volatiles and the Origin of Comets. ApJ, 758(1):29.

A'Hearn, M. F., Millis, R. C., Schleicher, D. O., Osip, D. J., and Birch, P. V. (1995). The ensemble properties of comets: Results from narrowband photometry of 85 comets, 1976-1992. Icarus, 118(2):223–270.

Altwegg, K., Balsiger, H., and Fuselier, S. A. (2019). Cometary Chemistry and the Origin of Icy Solar System Bodies: The View After Rosetta. ARA&A, 57:113–155.

Altwegg, K., Balsiger, H., Hänni, N., Rubin, M., Schuhmann, M., Schroeder, I., Sémon, T., Wampfler, S., Berthelier, J.-J., Briois, C., Combi, M., Gombosi, T. I., Cottin, H., De Keyser, J., Dhooghe, F., Fiethe, B., and Fuselier, S. A. (2020). Evidence of ammonium salts in comet 67P as explanation for the nitrogen depletion in cometary comae. *Nature Astronomy*, 4:533–540.

André, P., Belloche, A., Motte, F., and Peretto, N. (2007). The initial conditions of star formation in the Ophiuchus main cloud: Kinematics of the protocluster condensations. A&A, 472(2):519–535.

Andre, P. and Montmerle, T. (1994). From T Tauri Stars to Protostars: Circumstellar Material and Young Stellar Objects in the rho Ophiuchi Cloud. ApJ, 420:837.

Andrews, S. M. and Williams, J. P. (2005). Circumstellar Dust Disks in Taurus-Auriga: The Submillimeter Perspective. ApJ, 631(2):1134–1160.

Andrews, S. M. and Williams, J. P. (2007). A Submillimeter View of Circumstellar Dust Disks in ρ Ophiuchi. ApJ, 671(2):1800–1812.

Arce-Tord, C., Vidal, M., Casassus, S., Cárcamo, M., Dickinson, C., Hensley, B. S., Génova-Santos, R., Bond, J. R., Jones, M. E., Readhead, A. C. S., Taylor, A. C., and Zensus, J. A. (2020). Resolved observations at 31 GHz of spinning dust emissivity variations in ρ Oph. MNRAS, 495(3):3482–3493.

Bergner, J. B. and Ciesla, F. (2021). Ice Inheritance in Dynamical Disk Models. ApJ, 919(1):45.

Bevington, P. R. and Robinson, D. K. (2003). *Data reduction and error analysis for the physical sciences*. McGraw-Hill Education.

Bigiel, F., Leroy, A., Walter, F., Brinks, E., de Blok, W. J. G., Madore, B., and Thornley, M. D. (2008). The Star Formation Law in Nearby Galaxies on Sub-Kpc Scales. AJ, 136(6):2846–2871.

Biver, N., Bockelée-Morvan, D., Colom, P., Crovisier, J., Henry, F., Lellouch, E., Winnberg, A., Johansson, L. E. B., Gunnarsson, M., Rickman, H., Rantakyrö, F., Davies, J. K., Dent, W. R. F., Paubert, G., Moreno, R., Wink, J., Despois, D., Benford, D. J., Gardner, M., Lis, D. C., Mehringer, D., Phillips, T. G., and Rauer, H. (2002). The 1995 2002 Long-Term Monitoring of Comet C/1995 O1 (HALE BOPP) at Radio Wavelength. *Earth Moon and Planets*, 90(1):5–14.

Biver, N., Bockelée-Morvan, D., Crovisier, J., Lis, D. C., Moreno, R., Colom, P., Henry, F., Herpin, F., Paubert, G., and Womack, M. (2006). Radio wavelength molecular observations of comets C/1999 T1 (McNaught-Hartley), C/2001 A2 (LINEAR), C/2000 WM_1 (LINEAR) and 153P/Ikeya-Zhang. A&A, 449(3):1255–1270.

Bockelée-Morvan, D. and Biver, N. (2017). The composition of cometary ices. *Philosophical Transactions of the Royal Society of London Series A*, 375(2097):20160252.

Bockelée-Morvan, D., Crovisier, J., Mumma, M. J., and Weaver, H. A. (2004). The composition of cometary volatiles. In Festou, M. C., Keller, H. U., and Weaver, H. A., editors, *Comets II*, page 391. University of Arizona Press.

Bockelée-Morvan, D., Hartogh, P., Crovisier, J., Vandenbussche, B., Swinyard, B. M., Biver, N., Lis, D. C., Jarchow, C., Moreno, R., Hutsemékers, D., Jehin, E., Küppers, M., Lara, L. M., Lellouch, E., Manfroid, J., de Val-Borro, M., Szutowicz, S., Banaszkiewicz, M., Bensch, F., Blecka, M. I., Emprechtinger, M., Encrenaz, T., Fulton, T., Kidger, M., Rengel, M., Waelkens, C., Bergin, E., Blake, G. A., Blommaert, J. A. D. L., Cernicharo, J., Decin, L., Encrenaz, P., de Graauw, T., Leeks, S., Medvedev, A. S., Naylor, D., Schieder, R., and Thomas, N. (2010). A study of the distant activity of comet C/2006 W3 (Christensen) with Herschel and ground-based radio telescopes. A&A, 518:L149.

Bonev, B. P. (2005). *Towards a Chemical Taxonomy of Comets: Infrared Spectroscopic Methods for Quantitative Measurements of Cometary Water*. PhD thesis, University of Toledo, Ohio.

Bonev, B. P., Dello Russo, N., DiSanti, M. A., Martin, E. C., Doppmann, G., Vervack, Ronald J., J., Villanueva, G. L., Kawakita, H., Gibb, E. L., Combi, M. R., Roth, N. X., Saki, M., McKay, A. J., Cordiner, M. A., Bodewits, D., Crovisier, J., Biver, N., Cochran, A. L., Shou, Y., Khan, Y., and Venkataramani, K. (2021). First Comet Observations with NIRSPEC-2 at Keck: Outgassing Sources of Parent Volatiles and Abundances Based on Alternative Taxonomic Compositional Baselines in 46P/Wirtanen. *Planetary Science Journal*, 2(2):45.

Bonev, B. P., Dello Russo, N., Kawakita, H., Vervack, Ronald J., J., DiSanti, M. A., Shinnaka, Y., Ootsubo, T., Gibb, E. L., Combi, M. R., Altwegg, K., Biver, N., Crovisier, J., Doppmann, G., Villanueva, G. L., Khan, Y., Ejeta, C. T., Saki, M., McKay, A. J., Cochran, A. L., Jehin, E., Roth, N. X., Cordiner, M. A., and Shou, Y. (2023). The Return of the Rosetta Target: Keck Near-infrared Observations of Comet 67P/Churyumov-Gerasimenko in 2021. AJ, 166(6):233.

Bonev, B. P. and Mumma, M. J. (2006). A Comprehensive Study of Infrared OH Prompt Emission in Two Comets. II. Implications for Unimolecular Dissociation of H_2O. ApJ, 653(1):788–791.

Bonev, B. P., Mumma, M. J., Villanueva, G. L., Disanti, M. A., Ellis, R. S., Magee-Sauer, K., and Dello Russo, N. (2007). A Search for Variation in the H_2O Ortho-Para Ratio and Rotational Temperature in the Inner Coma of Comet C/2004 Q2 (Machholz). ApJ, 661(1):L97–L100.

Bonev, B. P., Villanueva, G. L., DiSanti, M. A., Boehnhardt, H., Lippi, M., Gibb, E. L., Paganini, L., and Mumma, M. J. (2017). Beyond 3 au from the Sun: The Hypervolatiles CH_4, C_2H_6, and CO in the Distant Comet C/2006 W3 (Christensen). AJ, 153(5):241.

Bontemps, S., André, P., Kaas, A. A., Nordh, L., Olofsson, G., Huldtgren, M., Abergel, A., Blommaert, J., Boulanger, F., Burgdorf, M., Cesarsky, C. J., Cesarsky, D., Copet, E., Davies, J., Falgarone, E., Lagache, G., Montmerle, T., Pérault, M., Persi, P., Prusti, T., Puget, J. L., and Sibille, F. (2001). ISOCAM observations of the rho Ophiuchi cloud: Luminosity and mass functions of the pre-main sequence embedded cluster. A&A, 372:173–194.

Bregman, J. D., Witteborn, F. C., Allamandola, L. J., Campins, H., Wooden, D. H., Rank, D. M., Cohen, M., and Tielens, A. G. G. M. (1987). Airborne and groundbased spectrophotometry of comet P/Halley from 5-13 micrometers. A&A, 187(1-2):616–620.

Brooke, T. Y., Tokunaga, A. T., Weaver, H. A., Crovisier, J., Bockelée-Morvan, D., and Crisp, D. (1996). Detection of acetylene in the infrared spectrum of comet Hyakutake. Nature, 383(6601):606–608.

Brooke, T. Y., Weaver, H. A., Chin, G., Bockelée-Morvan, D., Kim, S. J., and Xu, L. H. (2003). Spectroscopy of Comet Hale-Bopp in the infrared. Icarus, 166(1):167–187.

Cambianica, P., Munaretto, G., Cremonese, G., Podio, L., Codella, C., and Boschin, W. (2023). CO_2 as the main parent source of atomic oxygen in comet C/2017 K2 (Pan-STARRS). A&A, 674:L14.

Casassus, S., Avenhaus, H., Pérez, S., Navarro, V., Cárcamo, M., Marino, S., Cieza, L., Quanz, S. P., Alarcón, F., Zurlo, A., Osses, A., Rannou, F. R., Román, P. E., and Barraza, M. (2018). An inner warp in the DoAr 44 T Tauri transition disc. MNRAS, 477(4):5104–5114.

Combi, M. R., Fougere, N., Mäkinen, J. T. T., Bertaux, J. L., Quémerais, E., and Ferron, S. (2014). Unusual Water Production Activity of Comet C/2012 S1 (ISON): Outbursts and Continuous Fragmentation. ApJ, 788(1):L7.

Combi, M. R., Harris, W. M., and Smyth, W. H. (2004). Gas dynamics and kinetics in the cometary coma: theory and observations. In Festou, M. C., Keller, H. U., and Weaver, H. A., editors, *Comets II*, page 523. University of Arizona Press.

Combi, M. R., Mäkinen, T., Bertaux, J. L., Quémerais, E., and Ferron, S. (2023). Water production rates from SOHO/SWAN observations of comets C/2020 S3 (Erasmus), C/2021 A1 (Leonard) and C/2021 O3 (PanSTARRS). Icarus, 398:115543.

Combi, M. R., Mäkinen, T., Bertaux, J. L., Quémerais, E., Ferron, S., and Coronel, R. (2020). Comet 41P/Tuttle-Giacobini-Kresak, 45P/Honda-Mrkos-Pajdusakova, and 46P/Wirtanen: Water Production Activity over 21 yr with SOHO/SWAN. *Planetary Science Journal*, 1(3):72.

Combi, M. R., Mäkinen, T. T., Bertaux, J. L., Quémerais, E., and Ferron, S. (2019). A survey of water production in 61 comets from SOHO/SWAN observations of hydrogen Lyman-alpha: Twenty-one years 1996-2016. Icarus, 317:610–620.

Cottin, H., Gazeau, M. C., Benilan, Y., and Raulin, F. (2001). Polyoxymethylene as Parent Molecule for the Formaldehyde Extended Source in Comet Halley. ApJ, 556(1):417–420.

Cox, E. G., Harris, R. J., Looney, L. W., Chiang, H.-F., Chandler, C., Kratter, K., Li, Z.-Y., Perez, L., and Tobin, J. J. (2017). Protoplanetary Disks in ρ Ophiuchus as Seen from ALMA. ApJ, 851(2):83.

Crovisier, J., Biver, N., Bockelée-Morvan, D., Boissier, J., Colom, P., and Lis, D. C. (2009). The Chemical Diversity of Comets: Synergies Between Space Exploration and Ground-based Radio Observations. *Earth Moon and Planets*, 105(2-4):267–272.

Crovisier, J., Bockelée-Morvan, D., Colom, P., Biver, N., Despois, D., Lis, D. C., and Target-of-opportunity Radio Observations of Comets Team (2004). The composition of ices in comet C/1995 O1 (Hale-Bopp) from radio spectroscopy. Further results and upper limits on undetected species. A&A, 418:1141–1157.

Crovisier, J., Encrenaz, T., Lyle, S., and Bonnet, F. b. R. M. (2000). *Comet Science*. Cambridge University Press.

Cushing, M. C., Vacca, W. D., and Rayner, J. T. (2004). Spextool: A Spectral Extraction Package for SpeX, a 0.8-5.5 Micron Cross-Dispersed Spectrograph. PASP, 116(818):362–376.

Dello Russo, N., DiSanti, M. A., Magee-Sauer, K., Gibb, E. L., Mumma, M. J., Barber, R. J., and Tennyson, J. (2004). Water production and release in Comet 153P/Ikeya-Zhang (C/2002 C1): accurate rotational temperature retrievals from hot-band lines near 2.9-μm. Icarus, 168(1):186–200.

Dello Russo, N., DiSanti, M. A., Mumma, M. J., Magee-Sauer, K., and Rettig, T. W. (1998). Carbonyl Sulfide in Comets C/1996 B2 (Hyakutake) and C/1995 O1 (Hale-Bopp): Evidence for an Extended Source in Hale-Bopp. Icarus, 135(2):377–388.

Dello Russo, N., Kawakita, H., Bonev, B. P., Vervack, R. J., Gibb, E. L., Shinnaka, Y., Roth, N. X., DiSanti, M. A., and McKay, A. J. (2020). Post-perihelion volatile production and release from Jupiter-family comet 45P/Honda-Mrkos-Pajdušáková. Icarus, 335:113411.

Dello Russo, N., Kawakita, H., Vervack, R. J., and Weaver, H. A. (2016a). Emerging trends and a comet taxonomy based on the volatile chemistry measured in thirty comets with high-resolution infrared spectroscopy between 1997 and 2013. Icarus, 278:301–332.

Dello Russo, N., Mumma, M. J., DiSanti, M. A., and Magee-Sauer, K. (2002). Production of ethane and water in comet C/1996 B2 Hyakutake. *Journal of Geophysical Research (Planets)*, 107(E11):5095.

Dello Russo, N., Mumma, M. J., DiSanti, M. A., Magee-Sauer, K., and Novak, R. (2001). Ethane Production and Release in Comet C/1995 O1 Hale-Bopp. Icarus, 153(1):162–179.

Dello Russo, N., Vervack, R. J., J., Weaver, H. A., Kawakita, H., Kobayashi, H., Biver, N., Bockelée-Morvan, D., and Crovisier, J. (2009a). The Parent Volatile Composition of 6p/d'Arrest and a Chemical Comparison of Jupiter-Family Comets Measured at Infrared Wavelengths. ApJ, 703(1):187–197.

Dello Russo, N., Vervack, R. J., Kawakita, H., Bonev, B. P., DiSanti, M. A., Gibb, E. L., McKay, A. J., Cochran, A. L., Weaver, H. A., Biver, N., Crovisier, J., Bockelée-Morvan, D., Kobayashi, H., Harris, W. M., Roth, N. X., Saki, M., and Khan, Y. (2022). Volatile Abundances, Extended Coma Sources, and Nucleus Ice Associations in Comet C/2014 Q2 (Lovejoy). *Planetary Science Journal*, 3(1):6.

Dello Russo, N., Vervack, R. J., Kawakita, H., Cochran, A., McKay, A. J., Harris, W. M., Weaver, H. A., Lisse, C. M., DiSanti, M. A., Kobayashi, H., Biver, N., Bockelée-Morvan, D., Crovisier, J., Opitom, C., and Jehin, E. (2016b). The compositional evolution of C/2012 S1 (ISON) from ground-based high-resolution infrared spectroscopy as part of a worldwide observing campaign. Icarus, 266:152–172.

Dello Russo, N., Vervack, R. J., Weaver, H. A., and Lisse, C. M. (2009b). Infrared measurements of the chemical composition of C/2006 P1 McNaught. Icarus, 200(1):271–279.

DiSanti, M. A., Bonev, B. P., Dello Russo, N., McKay, A. J., Roth, N. X., Saki, M., Gibb, E. L., Vervack, Ronald J., J., Khan, Y., and Kawakita, H. (2021). Volatile Composition and Outgassing in C/2018 Y1 (Iwamoto): Extending Limits for High-resolution Infrared Cometary Spectroscopy between 2.8 and 5.0 μm. *Planetary Science Journal*, 2(6):225.

DiSanti, M. A., Bonev, B. P., Gibb, E. L., Paganini, L., Villanueva, G. L., Mumma, M. J., Keane, J. V., Blake, G. A., Dello Russo, N., Meech, K. J., Vervack, R. J., J., and McKay, A. J. (2016). En Route to Destruction: The Evolution in Composition of Ices in Comet D/2012 S1 (ISON) between 1.2 and 0.34 AU from the Sun as Revealed at Infrared Wavelengths. ApJ, 820(1):34.

DiSanti, M. A., Bonev, B. P., Gibb, E. L., Roth, N. X., Dello Russo, N., and Vervack, Ronald J., J. (2018). Comet C/2013 V5 (Oukaimeden): Evidence for Depleted Organic Volatiles and Compositional Heterogeneity as Revealed through Infrared Spectroscopy. AJ, 156(6):258.

DiSanti, M. A., Bonev, B. P., Magee-Sauer, K., Dello Russo, N., Mumma, M. J., Reuter, D. C., and Villanueva, G. L. (2006). Detection of Formaldehyde Emission in Comet C/2002 T7 (LINEAR) at Infrared Wavelengths: Line-by-Line Validation of Modeled Fluorescent Intensities. ApJ, 650(1):470–483.

DiSanti, M. A., Bonev, B. P., Russo, N. D., Vervack, Ronald J., J., Gibb, E. L., Roth, N. X., McKay, A. J., Kawakita, H., Feaga, L. M., and Weaver, H. A. (2017). Hypervolatiles in a Jupiter-family Comet: Observations of 45P/Honda-Mrkos-Pajdušáková Using iSHELL at the NASA-IRTF. AJ, 154(6):246.

DiSanti, M. A., Bonev, B. P., Villanueva, G. L., and Mumma, M. J. (2013). Highly Depleted Ethane and Mildly Depleted Methanol in Comet 21P/Giacobini-Zinner: Application of a New Empirical ν_2-band Model for CH_3OH near 50 K. ApJ, 763(1):1.

Disanti, M. A., dello Russo, N., Magee-Sauer, K., Gibb, E. L., Reuter, D. C., and Mumma, M. J. (2002). CO, H_2CO, and CH_3OH in comet 2002 C1 Ikeya-Zhang. In Warmbein, B., editor, *Asteroids, Comets, and Meteors: ACM 2002*, volume 500 of *ESA Special Publication*, pages 571–574.

DiSanti, M. A., Mumma, M. J., Dello Russo, N., Magee-Sauer, K., and Griep, D. M. (2003). Evidence for a dominant native source of carbon monoxide in Comet C/1996 B2 (Hyakutake). *Journal of Geophysical Research (Planets)*, 108(E6):5061.

DiSanti, M. A., Mumma, M. J., Russo, N. D., and Magee-Sauer, K. (2001). Carbon Monoxide Production and Excitation in Comet C/1995 O1 (Hale-Bopp): Isolation of Native and Distributed CO Sources. Icarus, 153(2):361–390.

DiSanti, M. A., Villanueva, G. L., Paganini, L., Bonev, B. P., Keane, J. V., Meech, K. J., and Mumma, M. J. (2014). Pre- and post-perihelion observations of C/2009 P1 (Garradd): Evidence for an oxygen-rich heritage? Icarus, 228:167–180.

Dobbs, C. L., Krumholz, M. R., Ballesteros-Paredes, J., Bolatto, A. D., Fukui, Y., Heyer, M., Low, M. M. M., Ostriker, E. C., and Vázquez-Semadeni, E. (2014). Formation of Molecular Clouds and Global Conditions for Star Formation. In Beuther, H., Klessen, R. S., Dullemond, C. P., and Henning, T., editors, *Protostars and Planets VI*, pages 3–26.

Drozdovskaya, M. N., Walsh, C., van Dishoeck, E. F., Furuya, K., Marboeuf, U., Thiabaud, A., Harsono, D., and Visser, R. (2016). Cometary ices in forming protoplanetary disc midplanes. MNRAS, 462(1):977–993.

Dunham, M. M., Stutz, A. M., Allen, L. E., Evans, N. J., I., Fischer, W. J., Megeath, S. T., Myers, P. C., Offner, S. S. R., Poteet, C. A., Tobin, J. J., and Vorobyov, E. I. (2014). The Evolution of Protostars: Insights from Ten Years of Infrared Surveys with Spitzer and Herschel. In Beuther, H., Klessen, R. S., Dullemond, C. P., and Henning, T., editors, *Protostars and Planets VI*, pages 195–218.

Eistrup, C., Walsh, C., and van Dishoeck, E. F. (2019). Cometary compositions compared with protoplanetary disk midplane chemical evolution. An emerging chemical evolution taxonomy for comets. A&A, 629:A84.

Ejeta, C., Gibb, E., Roth, N., DiSanti, M. A., Dello Russo, N., Saki, M., McKay, A. J., Kawakita, H., Khan, Y., Bonev, B. P., Vervack, R. J., and Combi, M. R. (2024). Coma Abundances of Volatiles at Small Heliocentric Distances: Compositional Measurements of Long-period Comet C/2020 S3 (Erasmus). AJ, 167(1):32.

Faggi, S., Lippi, M., Mumma, M. J., and Villanueva, G. L. (2023). Strongly Depleted Methanol and Hypervolatiles in Comet C/2021 A1 (Leonard): Signatures of Interstellar Chemistry? *Planetary Science Journal*, 4(1):8.

Faggi, S., Villanueva, G. L., Mumma, M. J., and Paganini, L. (2018). The Volatile Composition of Comet C/2017 E4 (Lovejoy) before its Disruption, as Revealed by High-resolution Infrared Spectroscopy with iSHELL at the NASA/IRTF. AJ, 156(2):68.

Ferrière, K. M. (2001). The interstellar environment of our galaxy. *Reviews of Modern Physics*, 73(4):1031–1066.

Fougere, N., Combi, M. R., Tenishev, V., Rubin, M., Bonev, B. P., and Mumma, M. J. (2012). Understanding measured water rotational temperatures and column densities in the very innermost coma of Comet 73P/Schwassmann-Wachmann 3 B. Icarus, 221(1):174–185.

Fray, N., Bénilan, Y., Biver, N., Bockelée-Morvan, D., Cottin, H., Crovisier, J., and Gazeau, M.-C. (2006). Heliocentric evolution of the degradation of polyoxymethylene: Application to the origin of the formaldehyde (H $_2$CO) extended source in Comet C/1995 O1 (Hale-Bopp). Icarus, 184(1):239–254.

Gibb, E. L., Bonev, B. P., Villanueva, G., DiSanti, M. A., Mumma, M. J., Sudholt, E., and Radeva, Y. (2012). Chemical Composition of Comet C/2007 N3 (Lulin): Another "Atypical" Comet. ApJ, 750(2):102.

Gibb, E. L., DiSanti, M. A., Magee-Sauer, K., Dello Russo, N., Bonev, B. P., and Mumma, M. J. (2007). The organic composition of C/2001 A2 (LINEAR). II. Search for heterogeneity within a comet nucleus. Icarus, 188(1):224–232.

Gibb, E. L., Mumma, M. J., Dello Russo, N., DiSanti, M. A., and Magee-Sauer, K. (2003). Methane in Oort cloud comets. Icarus, 165(2):391–406.

Greene, T. (2001). Protostars. *American Scientist*, 89(4):316.

Guilbert-Lepoutre, A. (2012). Survival of Amorphous Water Ice on Centaurs. AJ, 144(4):97.

Habart, E., Boulanger, F., Verstraete, L., Pineau des Forêts, G., Falgarone, E., and Abergel, A. (2003). H_2 infrared line emission across the bright side of the rho Ophiuchi main cloud. A&A, 397:623–634.

Harker, D. E., Woodward, C. E., and Wooden, D. H. (2005). The Dust Grains from 9P/Tempel 1 Before and After the Encounter with Deep Impact. *Science*, 310(5746):278–280.

Huebner, W. and Mukherjee, J. (2015). Photoionization and photodissociation rates in solar and blackbody radiation fields. *Planetary and Space Science*, 106:11–45.

Hui, M.-T., Jewitt, D., and Clark, D. (2018). Pre-discovery Observations and Orbit of Comet C/2017 K2 (PANSTARRS). AJ, 155(1):25.

Jeans, J. H. (1928). *Astronomy and cosmogony*. Cambridge University Press.

Jehin, E., Moulane, Y., Manfroid, J., Pozuelos, F., Ferrais, M., and Hutsemekers, D. (2020a). TRAPPIST comet production rates: 88/Howell, C/2020 M3 (ATLAS), C/2020 S3 (Erasmus), 156P/Russell-LINEAR. *The Astronomer's Telegram*, 14174:1.

Jehin, E., Moulane, Y., Manfroid, J., Pozuelos, F., and Hutsemekers, D. (2020b). TRAPPIST comet production rates: 88/Howell, C/2020 M3 (ATLAS), C/2020 S3 (Erasmus), 156P/Russell-LINEAR. *The Astronomer's Telegram*, 14101:1.

Jewitt, D. (2009). The Active Centaurs. AJ, 137(5):4296–4312.

Jewitt, D., Hui, M.-T., Mutchler, M., Weaver, H., Li, J., and Agarwal, J. (2017). A Comet Active Beyond the Crystallization Zone. ApJ, 847(2):L19.

Kawakita, H. and Mumma, M. J. (2011). Fluorescence Excitation Models of Ammonia and Amidogen Radical (NH_2) in Comets: Application to Comet C/2004 Q2 (Machholz). ApJ, 727(2):91.

Khan, Y., Gibb, E. L., Bonev, B. P., Roth, N. X., Saki, M., DiSanti, M. A., Dello Russo, N., Vervack, Ronald J., J., McKay, A. J., Combi, M. R., Shou, Y., Cordiner, M. A., Kawakita, H., Fougere, N., and Protopapa, S. (2021). Testing Short-term Variability and Sampling of Primary Volatiles in Comet 46P/Wirtanen. *Planetary Science Journal*, 2(1):20.

Królikowska, M. and Dybczyński, P. A. (2017). Oort spike comets with large perihelion distances. MNRAS, 472(4):4634–4658.

Krumholz, M. R. (2015). Notes on Star Formation. *arXiv e-prints*, page arXiv:1511.03457.

Kulesa, C. A., Hungerford, A. L., Walker, C. K., Zhang, X., and Lane, A. P. (2005). Large-Scale CO and [C I] Emission in the ρ Ophiuchi Molecular Cloud. ApJ, 625(1):194–209.

Kwok, S. (2007). *Physics and Chemistry of the Interstellar Medium*. University Science Books.

Lada, C. J. (2005). Star Formation in the Galaxy: An Observational Overview. *Progress of Theoretical Physics Supplement*, 158:1–23.

Larson, R. B. (1969). Numerical calculations of the dynamics of collapsing proto-star. MNRAS, 145:271.

Leroy, A. K., Walter, F., Brinks, E., Bigiel, F., de Blok, W. J. G., Madore, B., and Thornley, M. D. (2008). The Star Formation Efficiency in Nearby Galaxies: Measuring Where Gas Forms Stars Effectively. AJ, 136(6):2782–2845.

Levison, H. F. (1996). Comet Taxonomy. In Rettig, T. and Hahn, J. M., editors, *Completing the Inventory of the Solar System*, volume 107 of *Astronomical Society of the Pacific Conference Series*, pages 173–191.

Levison, H. F., Morbidelli, A., Tsiganis, K., Nesvorný, D., and Gomes, R. (2011). Late Orbital Instabilities in the Outer Planets Induced by Interaction with a Self-gravitating Planetesimal Disk. AJ, 142(5):152.

Lippi, M., Vander Donckt, M., Faggi, S., Moulane, Y., Mumma, M. J., Villanueva, G. L., and Jehin, E. (2023). The volatile composition of C/2021 A1 (Leonard): Comparison between infrared and UV-optical measurements. A&A, 676:A105.

Loinard, L., Torres, R. M., Mioduszewski, A. J., and Rodríguez, L. F. (2008). VLBA determinations of the distances to nearby star-forming regions. In Jin, W. J., Platais, I., and Perryman, M. A. C., editors, *A Giant Step: from Milli- to Micro-arcsecond Astrometry*, volume 248, pages 186–189.

Lombardi, M., Lada, C. J., and Alves, J. (2008). Hipparcos distance estimates of the Ophiuchus and the Lupus cloud complexes. A&A, 480(3):785–792.

Magee-Sauer, K., Mumma, M. J., DiSanti, M. A., and Dello Russo, N. (2002). Hydrogen cyanide in comet C/1996 B2 Hyakutake. *Journal of Geophysical Research (Planets)*, 107(E11).

Magee-Sauer, K., Mumma, M. J., DiSanti, M. A., Dello Russo, N., Gibb, E. L., Bonev, B. P., and Villanueva, G. L. (2008). The organic composition of Comet C/2001 A2 (LINEAR). I. Evidence for an unusual organic chemistry. Icarus, 194(1):347–356.

Mamajek, E. E. (2008). On the distance to the Ophiuchus star-forming region. *Astronomische Nachrichten*, 329(1):10.

Manara, C. F., Testi, L., Natta, A., and Alcalá, J. M. (2015). X-Shooter study of accretion in ρ-Ophiucus: very low-mass stars and brown dwarfs. A&A, 579:A66.

Martin, E. C., Fitzgerald, M. P., McLean, I. S., Doppmann, G., Kassis, M., Aliado, T., Canfield, J., Johnson, C., Kress, E., Lanclos, K., Magnone, K., Sohn, J. M., Wang, E., and Weiss, J. (2018). An overview of the NIRSPEC upgrade for the Keck II telescope. In Evans, C. J., Simard, L., and Takami, H., editors, *Ground-based and Airborne Instrumentation for Astronomy VII*, volume 10702 of *Society of Photo-Optical Instrumentation Engineers (SPIE) Conference Series*, page 107020A.

Martin, E. C., Fitzgerald, M. P., McLean, I. S., Kress, E., and Wang, E. (2016). Optical design of the slit-viewing camera for the NIRSPEC upgrade. In Evans, C. J., Simard, L., and Takami, H., editors, *Ground-based and Airborne Instrumentation for Astronomy VI*, volume 9908 of *Society of Photo-Optical Instrumentation Engineers (SPIE) Conference Series*, page 99082R.

Mayama, S., Tamura, M., Hanawa, T., Matsumoto, T., Ishii, M., Pyo, T.-S., Suto, H., Naoi, T., Kudo, T., Hashimoto, J., Nishiyama, S., Kuzuhara, M., and Hayashi, M. (2010). Direct Imaging of Bridged Twin Protoplanetary Disks in a Young Multiple Star. *Science*, 327(5963):306.

McClure, M. K., Furlan, E., Manoj, P., Luhman, K. L., Watson, D. M., Forrest, W. J., Espaillat, C., Calvet, N., D'Alessio, P., Sargent, B., Tobin, J. J., and Chiang, H.-F. (2010). The Evolutionary State of the Pre-main Sequence Population in Ophiuchus: A Large Infrared Spectrograph Survey. ApJS, 188(1):75–122.

McKay, A. J., DiSanti, M. A., Cochran, A. L., Bonev, B. P., Dello Russo, N., Vervack, Ronald J., J., Gibb, E., Roth, N. X., Saki, M., Khan, Y., and Kawakita, H. (2021). Quantifying the Hypervolatile Abundances in Jupiter-family Comet 46P/Wirtanen. *Planetary Science Journal*, 2(1):21.

McKay, A. J., DiSanti, M. A., Kelley, M. S. P., Knight, M. M., Womack, M., Wierzchos, K., Harrington Pinto, O., Bonev, B., Villanueva, G. L., Dello Russo, N., Cochran, A. L., Biver, N., Bauer, J., Vervack, Ronald J., J., Gibb, E., Roth, N., and Kawakita, H. (2019). The Peculiar Volatile Composition of CO-dominated Comet C/2016 R2 (PanSTARRS). AJ, 158(3):128.

Meech, K. J., Kleyna, J. T., Hainaut, O., Micheli, M., Bauer, J., Denneau, L., Keane, J. V., Stephens, H., Jedicke, R., Wainscoat, R., Weryk, R., Flewelling, H., Schunová-Lilly, E., Magnier, E., and Chambers, K. C. (2017). Co-driven activity in comet c/2017 k2 (panstarrs). *The Astrophysical Journal Letters*, 849(1):L8.

Morbidelli, A., Levison, H. F., Tsiganis, K., and Gomes, R. (2005). Chaotic capture of Jupiter's Trojan asteroids in the early Solar System. Nature, 435(7041):462–465.

Motte, F., Andre, P., and Neri, R. (1998). The initial conditions of star formation in the rho Ophiuchi main cloud: wide-field millimeter continuum mapping. A&A, 336:150–172.

Mumma, M. J. and Charnley, S. B. (2011). The Chemical Composition of Comets—Emerging Taxonomies and Natal Heritage. ARA&A, 49(1):471–524.

Mumma, M. J., Weissman, P. R., and Stern, S. A. (1993). Comets and the Origin of the Solar System - Reading the Rosetta Stone. In Levy, E. H. and Lunine, J. I., editors, *Protostars and Planets III*, page 1177.

Natta, A., Testi, L., and Randich, S. (2006). Accretion in the ρ-Ophiuchi pre-main sequence stars. A&A, 452(1):245–252.

Nesvorný, D., Vokrouhlický, D., Dones, L., Levison, H. F., Kaib, N., and Morbidelli, A. (2017). Origin and Evolution of Short-period Comets. ApJ, 845(1):27.

Öberg, K. I., Boogert, A. C. A., Pontoppidan, K. M., van den Broek, S., van Dishoeck, E. F., Bottinelli, S., Blake, G. A., and Evans, Neal J., I. (2011). The Spitzer Ice Legacy: Ice Evolution from Cores to Protostars. ApJ, 740(2):109.

Oka, T., Hasegawa, T., Sato, F., Tsuboi, M., Miyazaki, A., and Sugimoto, M. (2001). Statistical Properties of Molecular Clouds in the Galactic Center. ApJ, 562(1):348–362.

Ootsubo, T., Kawakita, H., Hamada, S., Kobayashi, H., Yamaguchi, M., Usui, F., Nakagawa, T., Ueno, M., Ishiguro, M., Sekiguchi, T., Watanabe, J.-i., Sakon, I., Shimonishi, T., and Onaka, T. (2012). AKARI Near-infrared Spectroscopic Survey for CO_2 in 18 Comets. ApJ, 752(1):15.

Ortiz-León, G. N., Loinard, L., Kounkel, M. A., Dzib, S. A., Mioduszewski, A. J., Rodríguez, L. F., Torres, R. M., González-Lópezlira, R. A., Pech, G., Rivera, J. L., Hartmann, L., Boden, A. F., Evans, Neal J., I., Briceño, C., Tobin, J. J., Galli, P. A. B., and Gudehus, D. (2017). The Gould's Belt Distances Survey (GOBELINS). I. Trigonometric Parallax Distances and Depth of the Ophiuchus Complex. ApJ, 834(2):141.

Ossenkopf, V., Krips, M., and Stutzki, J. (2008). Structure analysis of interstellar clouds. II. Applying the Δ-variance method to interstellar turbulence. A&A, 485(3):719–727.

Paganini, L., DiSanti, M. A., Mumma, M. J., Villanueva, G. L., Bonev, B. P., Keane, J. V., Gibb, E. L., Boehnhardt, H., and Meech, K. J. (2014). The Unexpectedly Bright Comet C/2012 F6 (Lemmon) Unveiled at Near-infrared Wavelengths. AJ, 147(1):15.

Paganini, L., Mumma, M. J., Boehnhardt, H., DiSanti, M. A., Villanueva, G. L., Bonev, B. P., Lippi, M., Käufl, H. U., and Blake, G. A. (2013). Ground-Based Infrared Detections of CO in the Centaur-comet 29P/Schwassmann-Wachmann 1 at 6.26 AU from the Sun. ApJ, 766(2):100.

Pineda, J. L., Goldsmith, P. F., Chapman, N., Snell, R. L., Li, D., Cambrésy, L., and Brunt, C. (2010). The Relation Between Gas and Dust in the Taurus Molecular Cloud. ApJ, 721(1):686–708.

Pinilla, P., Pérez, L. M., Andrews, S., van der Marel, N., van Dishoeck, E. F., Ataiee, S., Benisty, M., Birnstiel, T., Juhász, A., Natta, A., Ricci, L., and Testi, L. (2017). A Multi-wavelength Analysis of Dust and Gas in the SR 24S Transition Disk. ApJ, 839(2):99.

Poch, O., Istiqomah, I., Quirico, E., Beck, P., Schmitt, B., Theulé, P., Faure, A., Hily-Blant, P., Bonal, L., Raponi, A., Ciarniello, M., Rousseau, B., Potin, S., Brissaud, O., Flandinet, L., Filacchione, G., Pommerol, A., Thomas, N., Kappel, D., Mennella, V., Moroz, L., Vinogradoff, V., Arnold, G., Erard, S., Bockelée-Morvan, D., Leyrat, C., Capaccioni, F., De Sanctis, M. C., Longobardo, A., Mancarella, F., Palomba, E., and Tosi, F. (2020). Ammonium salts are a reservoir of nitrogen on a cometary nucleus and possibly on some asteroids. *Science*, 367(6483):aaw7462.

Prialnik, D. (1992). Crystallization, Sublimation, and Gas Release in the Interior of a Porous Comet Nucleus. ApJ, 388:196.

Prialnik, D. and Bar-Nun, A. (1992). Crystallization of amorphous ice as the cause of Comet P/Halley's outburst at 14 AU. A&A, 258(2):L9–L12.

Radeva, Y. L., Mumma, M. J., Bonev, B. P., DiSanti, M. A., Villanueva, G. L., Magee-Sauer, K., Gibb, E. L., and Weaver, H. A. (2010). The organic composition of Comet C/2000 WM $_1$ (LINEAR) revealed through infrared spectroscopy. Icarus, 206(2):764–777.

Radeva, Y. L., Mumma, M. J., Villanueva, G. L., Bonev, B. P., DiSanti, M. A., A'Hearn, M. F., and Dello Russo, N. (2013). High-resolution infrared spectroscopic measurements of Comet 2P/Encke: Unusual organic composition and low rotational temperatures. Icarus, 223(1):298–307.

Rayner, J., Tokunaga, A., Jaffe, D., Bond, T., Bonnet, M., Ching, G., Connelley, M., Cushing, M., Kokubun, D., Lockhart, C., Vacca, W., and Warmbier, E. (2022). iSHELL: a 1-5 micron R = 80,000 Immersion Grating Spectrograph for the NASA Infrared Telescope Facility. PASP, 134(1031):015002.

Reif, F. (1965). *Fundamentals of Statistical and Thermal Physics*. Waveland Press Inc.

Ressler, M. E. and Barsony, M. (2001). A Luminous Infrared Companion in the Young Triple System WL 20. AJ, 121(2):1098–1110.

Ridge, N. A., Di Francesco, J., Kirk, H., Li, D., Goodman, A. A., Alves, J. F., Arce, H. G., Borkin, M. A., Caselli, P., Foster, J. B., Heyer, M. H., Johnstone, D., Kosslyn, D. A., Lombardi, M., Pineda, J. E., Schnee, S. L., and Tafalla, M. (2006). The COMPLETE Survey of Star-Forming Regions: Phase I Data. AJ, 131(6):2921–2933.

Rigliaco, E., Wilking, B., Meyer, M. R., Jeffries, R. D., Cottaar, M., Frasca, A., Wright, N. J., Bayo, A., Bonito, R., Damiani, F., Jackson, R. J., Jiménez-Esteban, F., Kalari, V. M., Klutsch, A., Lanzafame, A. C., Sacco, G., Gilmore, G., Randich, S., Alfaro, E. J., Bragaglia, A., Costado, M. T., Franciosini, E., Lardo, C., Monaco, L., Morbidelli, L., Prisinzano, L., Sousa, S. G., and Zaggia, S. (2016). The Gaia-ESO Survey: Dynamical analysis of the L1688 region in Ophiuchus. A&A, 588:A123.

Roth, N. X. (2019). *Decoding the History of the Early Solar System Using Comet Volatile Compositions*. PhD thesis, Missouri University of Science and Technology, Rolla.

Roth, N. X., Bonev, B. P., DiSanti, M. A., Dello Russo, N., McKay, A. J., Gibb, E. L., Saki, M., Khan, Y., Vervack, Ronald J., J., Kawakita, H., Cochran, A. L., Biver, N., Cordiner, M. A., Crovisier, J., Jehin, E., and Weaver, H. (2021). The Volatile Composition of the Inner Coma of Comet 46P/Wirtanen: Coordinated Observations Using iSHELL at the NASA-IRTF and Keck/NIRSPEC-2. *Planetary Science Journal*, 2(2):54.

Roth, N. X., Gibb, E. L., Bonev, B. P., DiSanti, M. A., Dello Russo, N., Vervack, Ronald J., J., McKay, A. J., and Kawakita, H. (2018). A Tale of "Two" Comets: The Primary Volatile Composition of Comet 2P/Encke Across Apparitions and Implications for Cometary Science. AJ, 156(6):251.

Roth, N. X., Gibb, E. L., Bonev, B. P., DiSanti, M. A., Mumma, M. J., Villanueva, G. L., and Paganini, L. (2017). The Composition of Comet C/2012 K1 (PanSTARRS) and the Distribution of Primary Volatile Abundances among Comets. AJ, 153(4):168.

Saki, M., Gibb, E. L., Bonev, B. P., Roth, N. X., DiSanti, M. A., Dello Russo, N., Vervack, Ronald J., J., McKay, A. J., and Kawakita, H. (2020). Carbonyl Sulfide (OCS): Detections in Comets C/2002 T7 (LINEAR), C/2015 ER61 (PanSTARRS), and 21P/Giacobini-Zinner and Stringent Upper Limits in 46P/Wirtanen. AJ, 160(4):184.

Saki, M., Gibb, E. L., Bonev, B. P., Roth, N. X., DiSanti, M. A., Khan, Y., Dello Russo, N., Vervack, Ronald J., J., McKay, A. J., and Kawakita, H. (2021). Chemical Composition of Outbursting Comet C/2015 ER61 (PanSTARRS). AJ, 162(4):145.

Stahler, S. W. (1983). The birthline for low-mass stars. ApJ, 274:822–829.

Stern, S. A. (2003). The evolution of comets in the Oort cloud and Kuiper belt. Nature, 424(6949):639–642.

Sullivan, T., Wilking, B. A., Greene, T. P., Lisalda, L., Gibb, E. L., and Ejeta, C. (2019). A Radial Velocity Survey of Embedded Sources in the Rho Ophiuchi Cluster. AJ, 158(1):41.

Tennyson, J. (2011). *Astronomical Spectroscopy: AN Introduction to the Atomic and Molecular Physics of Astronomical Spectra (2ND Edition)*. World Scientific Publishing Company.

Vacca, W. D., Cushing, M. C., and Rayner, J. T. (2003). A Method of Correcting Near-Infrared Spectra for Telluric Absorption. PASP, 115(805):389–409.

Villanueva, G. L., DiSanti, M. A., Mumma, M. J., and Xu, L. H. (2012a). A Quantum Band Model of the ν_3 Fundamental of Methanol (CH_3OH) and Its Application to Fluorescence Spectra of Comets. ApJ, 747(1):37.

Villanueva, G. L., Magee-Sauer, K., and Mumma, M. J. (2013). Modeling of nitrogen compounds in cometary atmospheres: Fluorescence models of ammonia (NH_3), hydrogen cyanide (HCN), hydrogen isocyanide (HNC) and cyanoacetylene (HC_3N). J. Quant. Spec. Radiat. Transf., 129:158–168.

Villanueva, G. L., Mumma, M. J., Bonev, B. P., Novak, R. E., Barber, R. J., and Disanti, M. A. (2012b). Water in planetary and cometary atmospheres: H_2O/HDO transmittance and fluorescence models. J. Quant. Spec. Radiat. Transf., 113(3):202–220.

Villanueva, G. L., Mumma, M. J., DiSanti, M. A., Bonev, B. P., Gibb, E. L., Magee-Sauer, K., Blake, G. A., and Salyk, C. (2011a). The molecular composition of Comet C/2007 W1 (Boattini): Evidence of a peculiar outgassing and a rich chemistry. Icarus, 216(1):227–240.

Villanueva, G. L., Mumma, M. J., and Magee-Sauer, K. (2011b). Ethane in planetary and cometary atmospheres: Transmittance and fluorescence models of the ν_7 band at 3.3 μm. *Journal of Geophysical Research (Planets)*, 116(E8):E08012.

Villanueva, G. L., Smith, M. D., Protopapa, S., Faggi, S., and Mandell, A. M. (2018). Planetary Spectrum Generator: An accurate online radiative transfer suite for atmospheres, comets, small bodies and exoplanets. J. Quant. Spec. Radiat. Transf., 217:86–104.

Vokrouhlický, D., Nesvorný, D., and Dones, L. (2019). Origin and Evolution of Long-period Comets. AJ, 157(5):181.

Vuong, M. H., Montmerle, T., Grosso, N., Feigelson, E. D., Verstraete, L., and Ozawa, H. (2003). Determination of the gas-to-dust ratio in nearby dense clouds using X-ray absorption measurements. A&A, 408:581–599.

Wainscoat, R. J., Wells, L., Micheli, M., and Sato, H. (2017). Comet C/2017 K2 (Panstarrs). *Central Bureau Electronic Telegrams*, 4393:1.

Wierzchos, K. and Womack, M. (2018). C/2016 R2 (PANSTARRS): A Comet Rich in CO and Depleted in HCN. AJ, 156(1):34.

Wilking, B. A., Gagné, M., and Allen, L. E. (2008). Star Formation in the ρ Ophiuchi Molecular Cloud. In Reipurth, B., editor, *Handbook of Star Forming Regions, Volume II*, volume 5, page 351. Astronomical Society of the Pacific.

Willacy, K., Turner, N., Bonev, B., Gibb, E., Dello Russo, N., DiSanti, M., Vervack, Ronald J., J., and Roth, N. X. (2022). Comets in Context: Comparing Comet Compositions with Protosolar Nebula Models. ApJ, 931(2):164.

Wooden, D. H., Woodward, C. E., and Harker, D. E. (2004). Discovery of Crystalline Silicates in Comet C/2001 Q4 (NEAT). ApJ, 612(1):L77–L80.

Yang, B., Jewitt, D., Zhao, Y., Jiang, X., Ye, Q., and Chen, Y.-T. (2021). Discovery of Carbon Monoxide in Distant Comet C/2017 K2 (PANSTARRS). ApJ, 914(1):L17.

Zolensky, M. E., Zega, T. J., Yano, H., Wirick, S., Westphal, A. J., Weisberg, M. K., Weber, I., Warren, J. L., Velbel, M. A., Tsuchiyama, A., Tsou, P., Toppani, A., Tomioka, N., Tomeoka, K., Teslich, N., Taheri, M., Susini, J., Stroud, R., Stephan, T., Stadermann, F. J., Snead, C. J., Simon, S. B., Simionovici, A., See, T. H., Robert, F., Rietmeijer, F. J. M., Rao, W., Perronnet, M. C., Papanastassiou, D. A., Okudaira, K., Ohsumi, K., Ohnishi, I., Nakamura-Messenger, K., Nakamura, T., Mostefaoui, S., Mikouchi, T., Meibom, A., Matrajt, G., Marcus, M. A., Leroux, H., Lemelle, L., Le, L., Lanzirotti, A., Langenhorst, F., Krot, A. N., Keller, L. P., Kearsley, A. T., Joswiak, D., Jacob, D., Ishii, H., Harvey, R., Hagiya, K., Grossman, L., Grossman, J. N., Graham, G. A., Gounelle, M., Gillet, P., Genge, M. J., Flynn, G., Ferroir, T., Fallon, S., Ebel, D. S., Dai, Z. R., Cordier, P., Clark, B., Chi, M., Butterworth, A. L., Brownlee, D. E., Bridges, J. C., Brennan, S., Brearley, A., Bradley, J. P., Bleuet, P., Bland, P. A., and Bastien, R. (2006). Mineralogy and Petrology of Comet 81P/Wild 2 Nucleus Samples. *Science*, 314(5806):1735.

VITA

Chemeda Tadese Ejeta was born in South Western part of Ethiopia, Oromia region. He came to St. Louis at the end of 2012 and finally joined the UMSL graduate program. He obtained his Master's degree from UMSL in 2017 on the path to his Ph.D. program. He received his Doctor of Philosophy in Physics from the Missouri University of Science and Technology and the University of Missouri-St. Louis in May 2024.